© Copyright 2022

Alejandra Jazmin Cabrera

The dissemination of oncogenic *Ras^{V12}*-transformed cells in the adult *Drosophila* intestine

Alejandra Jazmin Cabrera

A dissertation

submitted in partial fulfillment of the

requirements for the degree of

Doctor of Philosophy

University of Washington

Year 2022

Reading Committee:

Young Kwon, Chair

Richard Palmiter

Hannele Ruohola-Baker

Program Authorized to Offer Degree:

Biochemistry

University of Washington

Abstract

The dissemination of oncogenic *Ras*^{V12}-transformed cells in the adult *Drosophila* intestine

Alejandra Jazmin Cabrera

Chair of the Supervisory Committee:

Young Kwon, PhD

Biochemistry

Dissemination of transformed cells is a key process in metastasis. Despite its importance, how transformed cells disseminate from an intact tissue and enter the circulation is poorly understood. Here, we use a fully developed tissue, *Drosophila* midgut, and describe the morphologically distinct steps and the cellular events occurring over the course of *Ras*^{V12}-transformed cell dissemination. Notably, *Ras*^{V12}-transformed cells formed the Actin- and Cortactin-rich invasive protrusions that were important for breaching the extracellular matrix (ECM) and visceral muscle. Next, employing this *Drosophila* model of cell dissemination, we uncovered the essential roles of the mechanosensory channel Piezo in orchestrating dissemination of *Ras*^{V12}-transformed

cells. Moreover, we demonstrate that the cell adhesion protein E-cadherin (E-cad) is necessary for the invasiveness of *Ras^{V12}*-transformed cells *in vivo*, challenging the prior perceived principle of the inverse relationship between E-cad levels and cell invasion. We demonstrate that *Drosophila* E-cad/β-catenin disassembles at adherens junctions and assembles at invasive protrusions during cell dissemination. Loss of E-cad attenuates dissemination of *Ras^{V12}*-transformed cells by impairing their ability to compromise the ECM. Furthermore, we show that the remodeling of E-cad/β-catenin subcellular distribution is controlled by two discrete intracellular calcium signaling pathways: Ca^{2+} release from endoplasmic reticulum via the inositol triphosphate receptor (IP3R) disassembles E-cad at adherens junctions while Ca^{2+} entry via Piezo assembles E-cad at invasive protrusions. Thus, our study provides molecular insights into the unconventional role of E-cad in cell invasion during cell dissemination *in vivo* and describes the discrete roles of intracellular calcium signaling in the remodeling of E-cad/β-catenin subcellular localization. Collectively, our study establishes an *in vivo* model for studying how transformed cells migrate out from a complex tissue and provides unique insights into the roles of E-cad, IP3R, and Piezo in invasive cell behavior.

Acknowledgements

I thank my mentor Young Kwon first and foremost for his guidance, patience, and support. I would like to thank my lab members, especially Jiae Lee for training me in all fly-related techniques and incentivizing lab outings. I also thank my IDTG mentor Barry Gumbiner for his advice. I am grateful to my past and present thesis committee members Drs. Young Kwon, Richard Palmiter, Hannele Ruohola-Baker, Susan Parkhurst, Trisha Davis, Barry Gumbiner, and David Kimmelman. I am thankful to my friend Amy Ferreccio for her support in and out of the academic setting. Thank you for being my rock when I needed it the most. Finally, I thank my family, especially my mom who has lived a difficult life as a low-income single parent. Thank you, mom, for always prioritizing my education and helping in the ways you could.

Dedication

I dedicate this dissertation to my siblings and mother Isabel. Luis, Dalia, Jose, Coral, and Adbiel, I love you all.

Table of Contents

List of Figures

Chapter 1. Introduction to *Drosophila* as a tool to study metastatic behavior

A hallmark of malignancy, metastasis is the major contributor of mortality in cancer patients [1, 2]. To metastasize, cancer cells undergo a series of processes, including dissemination from the original tumor site, circulation in blood or lymph, extravasation, and then colonization at a secondary site [2, 3]. Given that metastasis is initiated by dissemination from the original tumor site into the circulation, targeting this initial step could be an ideal strategy for intervening metastasis. Most of our knowledge of the molecular mechanisms of cell dissemination has been acquired from studies utilizing cancer cells in culture. Nevertheless, recapitulating the intricacy of the native microenvironment using *in vitro* culture systems remains difficult at best. Therefore, a simple *in vivo* system allowing us to observe the dissemination process in a native context will be useful to achieve a better understanding on the mechanisms that transformed cells utilize for dissemination.

Simple model organisms have provided tools to investigate the mechanisms underlying cell migration and invasion in native contexts [4]. For instance, migration of the border cells during *Drosophila* oocyte development has illustrated how cells can migrate collectively [4, 5]. Additionally, invasion of *Caenorhabditis elegans* (*C. elegans*) anchor cells into the vulval epithelia has provided a powerful tool to study invasive cell behavior in an *in vivo* microenvironment [6, 7]. In *Drosophila*, genetic manipulation of epithelial tissues can induce hyperplasia or tissue overgrowth—a so called 'tumor' in *Drosophila* [8-11]. Notably,

these *Drosophila* tumors also provide a tool to study metastatic behavior [12, 13]. In particular, a recent study demonstrated that adult hindgut epithelial cells expressing mutant *Ras* (Ras^{V12}) could disseminate from the hindgut and metastasize to distant tissues [14, 15]. Interestingly, the same study elucidated that sustained intestinal infection with pathogenic bacteria could enhance dissemination of Ras^{V12}-expressing hindgut cells via activation of Imd innate immune signaling [14]. Although these tumor models have allowed the identification of several genetic and environmental factors underlying metastatic phenotypes [12-14, 16, 17], it still remains obscure how these transformed cells disseminate from the primary tumor site into the hemocoel to initiate metastasis.

Here, we show that expression of Ras^{V12} in intestinal stem cells (ISCs) and enteroblasts (EBs) in the adult *Drosophila* midgut causes them to disseminate from the posterior midgut and transmigrate into the circulation. Our cellular and molecular characterization reveals how some of the molecular mechanisms underlying the migratory and invasive phenotypes of cancer cells are assembled *in vivo* to form a mode of cell dissemination. Observing the cell dissemination process in a native context allows us to describe Actin- and Cortactin-rich invasive protrusions that are associated with degradation of the ECM and the visceral muscle (VM) layer in *Drosophila* and discover the mechanosensitive channel Piezo as a key player of cell dissemination *in vivo*.

Chapter 2. Modeling cell dissemination in the adult *Drosophila* intestine

2.1 *Ras^{V12}* cells basally disseminate from the posterior midgut

Ras genes encode small GTPases that are frequently mutated in multiple types of cancers [18]. Oncogenic Ras isoforms affect multiple aspects of cancers, including the metastatic transformation of breast cancers [19-21]. In *Drosophila*, ectopic expression of *Ras^{V12}* in developing discs increases cell division; however, it is not sufficient to induce malignant transformation. Disruption of polarity in addition to *Ras^{V12}* is required to induce malignant disc tumors with metastatic properties [12]. Similarly, ectopic expression of *Ras^{V12}* in midgut ISCs and EBs using a clonal strategy was not sufficient to induce tumors. Instead, *Ras^{V12}*-expressing cells gradually disappeared from midguts [22, 23]. When we expressed *Ras^{V12}* in adult midgut ISCs and EBs using the conditional GAL4 driver *esg^{ts}* (*escargot-GAL4*, *tubulin-GAL80^{ts}*, *UAS-GFP*/+; see methods), *Ras^{V12}* cells propagated initially and then, progressively disappeared from the midgut. At day 6 of *Ras^{V12}* expression, most of the *Ras^{V12}* cells had been eliminated from the midgut (Fig. 1a). In contrast, cells expressing a gain-of-function *Raf* allele (*Raf^{gof}*) were retained in the midgut (Fig. 1a), indicating that general alteration in cell proliferation or cell crowding is not the cause of the phenotype.

Previously, it has been reported that the hindgut epithelial cells expressing *Ras^{V12}* could disseminate and metastasize to distant tissues [14]. Similarly, we noticed that a significant number of GFP-labeled *Ras^{V12}* cells were detected outside of the VM at day 2

of *Ras^{V12}* expression (Fig. 1b, c). Moreover, we detected GFP-labeled cells in hemolymph prepared from flies expressing *Ras^{V12}* with *esg^{ts}*, but not from control flies (Fig. 1d, e). To be detected outside the VM or in hemolymph, these cells must have passed through the basement membrane (BM), which resides outside of the midgut epithelium.

Previous studies have shown that metastatic transformation in *Drosophila* can upregulate Matrix-metalloprotease 1 (Mmp1) [14, 16, 24], which plays a crucial role in the degradation of the extracellular matrix (ECM). Similarly, we found that Mmp1 levels were increased by expression of *Ras^{V12}* but not *Raf^{gof}* (Fig. 1f, g). Additionally, expression of *Ras^{V12}* with *esg^{ts}* also caused a cell non-autonomous increase in Mmp1 signals in surrounding cells. Although expression of MMPs was thought to be critical for invasive cell behavior, anchor cells in *C. elegans* could physically breach the basement membrane even in the absence of MMPs by employing an extensive F-actin-rich protrusion [25]. We found that expression of Tissue inhibitor of metalloproteases (Timp) with *esg^{ts}* completely suppressed dissemination of *Ras^{V12}* cells (Fig. 1h and Supplementary Fig. 1a), suggesting the importance of MMPs in dissemination of *Ras^{V12}* cells.

Adult midgut is surrounded by thick ECM, which can be visualized by staining Laminin: one continuous Laminin layer is detected at the basal side of the epithelium (Fig. 1i and Supplementary Fig. 1c, white arrowhead) and another prominent Laminin layer is located at the outside of the VM (Supplementary Fig. 1c, yellow arrowhead). This complexity in the midgut ECM structure might account for the requirement of MMPs for dissemination of *Ras^{V12}* cells. In accordance with Mmp1 elevation, we detected deterioration of Laminin structure. At day 1 of *Ras^{V12}* expression, we frequently observed

a partial degradation of the ECM, which is manifested by loss of the Laminin layer adjacent to the intestinal epithelium (Supplementary Fig. 1c, white arrow). At day 2 of Ras^{V12} expression, more extensive degradation affecting the entire ECM structure was observed. The inner Laminin layer juxtaposed with the intestinal epithelium was almost completely absent (Fig. 1j, white arrow). Moreover, the Laminin layer outside visceral muscle was also significantly compromised, leading to patchy pattern of Laminin signals outside of the visceral muscle at day 2 of Ras^{V12} expression (Fig. 1j, yellow arrow and Supplementary Fig. 1d). Of importance, Laminin signals were almost invisible at the basal side of disseminated Ras^{V12} cells (Supplementary Fig. 1c, white arrow). This global degradation of the Laminin layer could be explained by the fact that Ras^{V12} cells covered the entire basal side of the midgut epithelium at day 1 of Ras^{V12} expression (Supplementary Fig. 2b). Therefore, a tissue-wide upregulation of Mmp1 signals was detected at day 1 of Ras^{V12} expression (Fig. 1f). Additionally, we speculate that cell non-autonomous MMP expression may contribute to the profound ECM degradation phenotype although the molecular mechanism underlying this cell non-autonomous Mmp1 expression requires further investigations.

We noticed that Ras^{V12} cells also frequently delaminated toward the midgut lumen after 2 days of Ras^{V12} expression (Supplementary Fig. 2b'). Altogether, our observations suggest that Ras^{V12} cells migrate out from the posterior midgut via at least two different processes: dissemination into the hemocoel and delamination into lumen. Of note, expression of baculovirus p35, an anti-apoptotic protein, did not impair the dissemination

of *Ras^{V12}* cells (Supplementary Fig. 2c), suggesting that cell death was not responsible for the phenotype.

2.2 Disseminating *Ras^{V12}* cells undergo morphological remodeling

Since the mechanism by which cells disseminate from a complex tissue is poorly described, we further investigated the phenomenon by scrutinizing the morphology of *Ras^{V12}* cells. We found that *Ras^{V12}* cells basally moved out from midgut epithelia at day 1 of *Ras^{V12}* expression (Fig. 2a). They resided in-between the epithelium and the VM layer and were significantly spread out (Fig. 2a). Interestingly, a significant portion of *Ras^{V12}* cells appeared to be bigger than normal ISCs or EBs (Supplementary Fig. 3a, b), an indication of possible misdifferentiation [26]. Nevertheless, a large portion of *Ras^{V12}* cells residing outside the epithelium could still divide (Fig. 2b) and express the Notch receptor ligand, Delta (Dl) (Fig. 2c and Supplementary Fig. 3c), which are the characteristics of active ISCs. At day 2 and 3 of *Ras^{V12}* expression, *Ras^{V12}* cells produced large protrusions across the VM while these large protrusions were not detected in control or *Raf^{gof}* cells (Fig. 2d). Furthermore, we were able to observe cells adopting various morphologies that appeared to be traversing the muscle layer (Fig. 2e).

2.3 Disseminating *Ras^{V12}* cells assemble invasive protrusions

Actin-based cellular structures play crucial roles in invasive cell behaviors. In particular, invadopodia, which are Actin- and Cortactin-rich protrusions associated with degradation of the ECM [27, 28], are known to be essential for cancer-cell invasive phenotypes [28, 29]. To address whether *Ras^{V12}* cells are forming similar invasive structures,

we decided to elucidate Actin cytoskeleton organization. Staining Actin with Phalloidin did not yield a discernable signal in ISCs and EBs because the adjacent VM expressed a large quantity of Actin. Thus, we assessed Actin cytoskeleton organization by expressing Actin-mRFP (*UAS-Actin-mRFP*) with esg^{ts}. Intriguingly, Actin-mRFP was detected as puncta at the basal side of Ras^{V12} cells that protruded toward the VM while similar puncta were undetectable in control cells (Fig. 3a, b). Of importance, these Actin-rich protrusions frequently reached the outer surface by passing through the BM and VM layers (Fig. 3b). Furthermore, these protrusions were also detected as large blebs at day 2 of Ras^{V12} expression (Fig. 3c).

In cancer cells, invadopodia are detected as protrusions enriched for both Actin and Cortactin—a regulator of actin polymerization [28]. Since the shape of these protrusions observed in Ras^{V12} cells resembles that of invadopodia [28], we examined Cortactin localization by expressing HA-tagged Cortactin (*UAS-Cortactin-HA*) with esg^{ts}. We found that Cortactin-HA was also detected as protrusions and large blebs at the basal side of Ras^{V12} cells (Supplementary Fig. 4b, c). In control cells, Cortactin-HA was broadly detected at the cortical region and did not form prominent puncta or protrusions at the basal side (Supplementary Fig. 4a). To further confirm that Cortactin-rich protrusions observed in Ras^{V12} cells were not formed due to an overexpression artifact, we expressed Cortactin-HA in Raf^{gof} cells. Nevertheless, we found that Cortactin-HA overexpression alone was not sufficient to induce similar protrusions and large blebs at the basal side of Raf^{gof} cells (Supplementary Fig. 4e, f). Notably, these Cortactin-rich protrusions found in

Ras^{V12} cells were also stained with Phalloidin (Fig. 3d, arrowhead), indicating that these protrusions were enriched for both Cortactin and Actin.

Remarkably, these protrusions could even perpendicularly penetrate the VM (Fig. 3d), resulting in damage to the tissue. In particular, we observed that the circular-muscles around *Ras*^{V12} cells became torn and thinned (Fig. 3a–c; Phalloidin staining). Interestingly, we detected large ruptures in the VM layer where multiple projections are concentrated (Fig. 3e and Supplementary Fig. 4d). When the midguts were viewed from the outside, a severe damage in VM was detected at day 2 of *Ras*^{V12} expression, which was manifested by breakage of the longitudinal muscles that normally span the whole posterior part of the midgut (Fig. 3f, g). We also noticed that a significant number of large blebs were visible outside of the posterior *esg*^{ts}*>Ras*^{V12} midguts (Fig. 3f, arrowhead). Altogether, these observations indicate that Actin- and Cortactin-rich protrusions are associated with the breach of the VM layer.

In cancer cells, Cortactin plays a crucial role in formation of invadopodia as well as secretion of MMPs [30]. Knockdown of *Cortactin* in cancer cells decreased MMP secretion and impaired ability to degrade the ECM by invadopodia [31]. Given the strong enrichment of Cortactin in the protrusions detected in *Ras*^{V12} cells, we decided to inactivate *Cortactin* to gain more insight into the role of these protrusions. *Cortactin* knockdown in *Ras*^{V12} cells suppressed ECM degradation (Supplementary Fig. 5a, b) and rescued the muscle-damage phenotype caused by *Ras*^{V12} cells (Supplementary Fig. 5c). Notably, Cortactin depletion caused a slight, but significant reduction in Mmp1 levels (Supplementary Fig. 5d, e). As a consequence, cell dissemination was almost completely suppressed by

Cortactin depletion in *Ras^{V12}* cells (Supplementary Fig. 5f). Altogether, these results demonstrate that these Actin- and Cortactin-rich protrusions observed in *Ras^{V12}* cells are linked to the breach of the ECM as well as the VM layer.

Note that we detected Lifeact-mRFP also forming puncta at the basal side of *Ras^{V12}* cells (Supplementary Fig. 6). In general, these puncta marked with Lifeact-mRFP remained underneath the VM layer and did not grow into large protrusions, which might be explained by defect in actin caused by the overexpression of Lifeact [32].

Our study describes the Actin- and Cortactin-rich protrusions that are associated with degradation of the ECM and the VM layer in *Drosophila*. The characteristics and the invasive nature of these protrusions resemble those of invadopodia observed in cancer cells [28]. Altogether, our observations demonstrate that dissemination of *Ras^{V12}* cells is an active process requiring cell-autonomous remodeling of cell morphology and formation of invasive protrusions at the basal side.

2.4 *Ras^{V12}* cells produce large blebs and extracellular vesicles

To gain further insights into how midgut epithelial cells disseminate by passing through the VM layers, we performed *ex vivo* live-imaging of midguts. We noticed that *Ras^{V12}* cells produced large blebs, which were also formed across the VM and eventually released as extracellular vesicles (Fig. 4a, b and Supplementary Videos 1–3). In contrast, *Raf^{gof}* cells did not produce a significant number of blebs or extracellular vesicles even though expression of *Raf^{gof}* induced comparable cell proliferation (Fig. 4b and Supplementary Video 4). The average size of these vesicles was approximately 3.1±1.5

μm (mean±SD) (Fig. 4c). Thus, they are bigger than exosomes (<100nm) and microvesicles (100–1000nm). Since these vesicles have not been previously described in *Drosophila*, we refer them as extremely large extracellular vesicles (ELEVs). Additionally, GFP-positive particles bigger than 1 μm were detected in hemolymph prepared from flies expressing Ras^{V12} but not from controls or flies expressing Raf^{gof}, indicating that ELEVs were also produced *in vivo* (Fig. 4d, e). Interestingly, these ELEVs are reminiscent of large extracellular vesicles, including large oncosomes and cytoplasts, which are also implicated in the invasive phenotypes of cancer cells [33-35].

Amoeboid movement, which is characterized by extensive blebbing, is used by cancer cells to migrate through holes in the matrix and move without support of adhesion [36-38]. Production of ELEVs implies that Ras^{V12} cells may utilize amoeboid movement. Indeed, we observed that Ras^{V12} cells in the posterior midgut often extensively remodeled their cell shape. Tracing the outline of representative Ras^{V12} cells in *ex vivo* time-lapse live imaging videos further visualized these dynamic remodeling events (Fig. 4f, g, and h). Notably, we observed that Ras^{V12} cells could migrate out from the midgut involving extensive blebbing (Fig. 4i and Supplementary Video 5). Additionally, Ras^{V12} cells could also slip out of the tissue without significant blebbing through a region where a large quantity of ELEVs had been generated (Supplementary Fig. 7 and Supplementary Video 6). These observations suggest that Ras^{V12} cells mainly use blebbing to migrate out from the midgut.

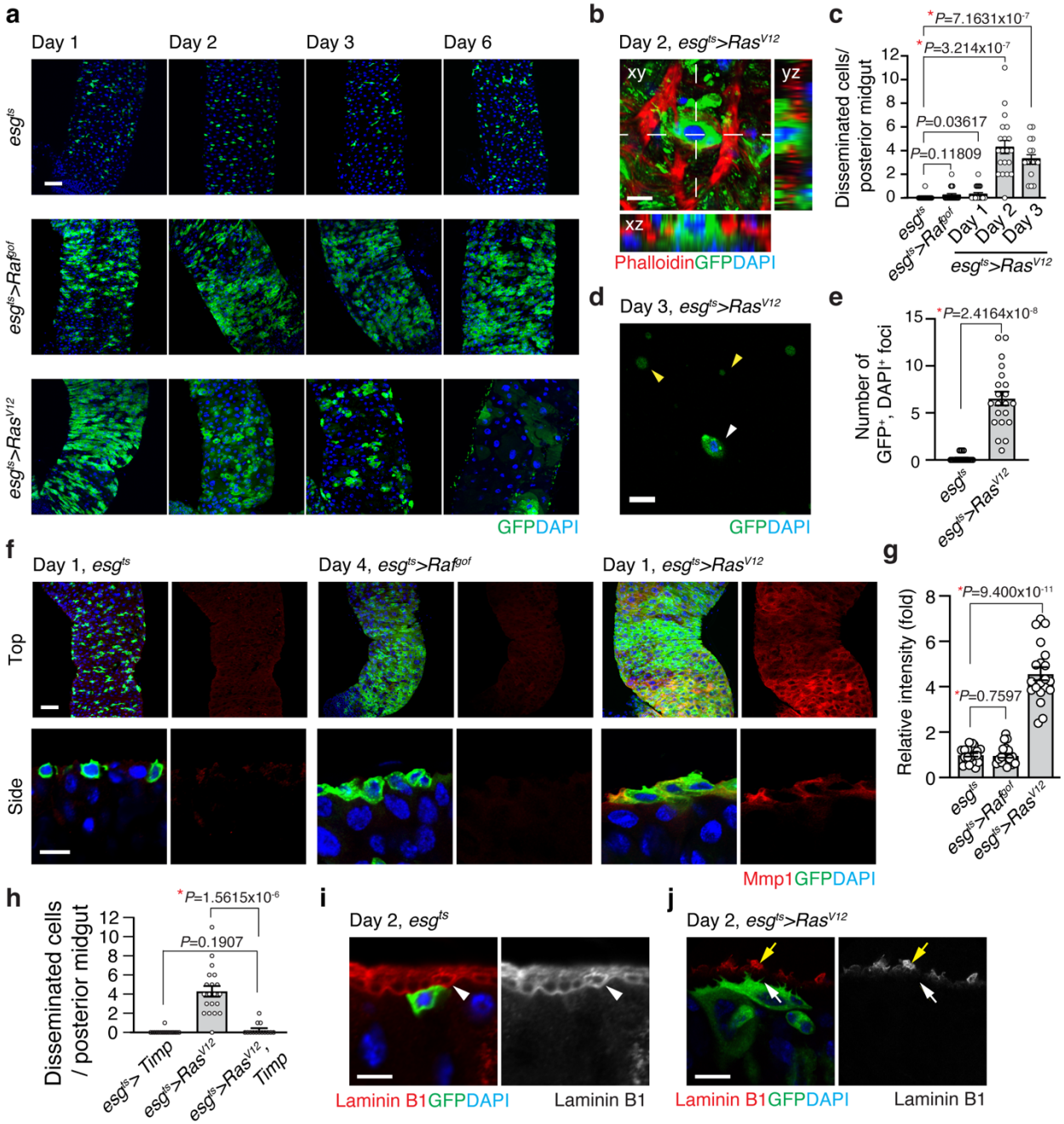
a
Day 1
Day 2
Day 3
Day 6
esgts
esgts>Rafgof
esgts>RasV12
GFPDAPI
b
Day 2, esgts>RasV12
xy
yz
xz
PhalloidinGFPDAPI
c
*P=7.1631x10-7
*P=3.214x10-7
P=0.03617
P=0.11809
Disseminated cells/ posterior midgut
esgts
esgts>Rafgof
Day 1
Day 2
Day 3
esgts>RasV12
d
Day 3, esgts>RasV12
GFPDAPI
e
*P=2.4164x10-8
Number of GFP+, DAPI+ foci
esgts
esgts>RasV12
f
Day 1, esgts
Day 4, esgts>Rafgof
Day 1, esgts>RasV12
Top
Side
Mmp1GFPDAPI
g
*P=9.400x10-11
*P=0.7597
Relative intensity (fold)
esgts
esgts>Rafgof
esgts>RasV12
h
*P=1.5615x10-6
P=0.1907
Disseminated cells / posterior midgut
esgts> Timp
esgts>RasV12
esgts>RasV12 , Timp
i
Day 2, esgts
Laminin B1GFPDAPI
Laminin B1
j
Day 2, esgts>RasV12
Laminin B1GFPDAPI
Laminin B1

Figure 1. *Ras^{V12}* cells basally disseminate from the posterior midgut.

a, Images of the posterior midgut. Transgenes were induced with *esg^{ts}* by incubating at 29°C for indicated durations. The cells manipulated by *esg^{ts}* are marked and stained with GFP (green), and nuclei are stained with DAPI (blue). Scale bar, 50 μm. **b**, Representative image of disseminated cell. Top view (xy) and orthogonal views (yz and xz) are shown. Phalloidin (red) visualizes VM. Scale bar, 10 μm. **c**, Quantification of disseminated cells detected on the surface of posterior midgut. N=25 (*esg^{ts}*), N=20 (*esg^{ts}>Raf^{gof}*), N=21 (Day1, *esg^{ts}>Ras^{V12}*), N=20 (Day 2, *esg^{ts}>Ras^{V12}*), N=16 (Day 3, *esg^{ts}>Ras^{V12}*) biological replicates. **d**, Representative image of GFP^{+} and DAPI^{+} cell (white arrowhead) detected in hemolymph. *Ras^{V12}* was expressed with *esg^{ts}* for 3 days before hemolymph collection. GFP^{+} and DAPI^{-} particles (yellow arrowheads) were also detected. Scale bar, 10 μm. **e,** Quantification of circulating GFP^{+} and DAPI^{+} cells. N=3 independent experiments for each genotype. **f**, Mmp1 immunostaining (red) in posterior midguts. Lower panels show side view of the cells. Scale bars, 50 μm (top) and 10 μm (bottom). **g**, Quantification of Mmp1 levels. N=20 data points collected from 7 biological replicates for each genotype. **h**, Quantification of disseminated cells detected on the surface of posterior midgut. N=16 (*esg^{ts}>Timp*), N=20 (*esg^{ts}>Ras^{V12}*), N=14 (*esg^{ts}>Ras^{V12}, Timp*) biological replicates. **I–j**, Laminin B1 staining of midguts. *esg^{ts}* and *esg^{ts}>Ras^{V12}* midguts were stained with anti-Laminin B1 antibody. White arrowhead in the *esg^{ts}* image points to the inner Laminin layer adjacent to the epithelium, white arrow in the *esg^{ts}>Ras^{V12}* images points the boundary of the epithelium where Laminin is degraded, and yellow arrow in the *esg^{ts}>Ras^{V12}* images points to a patchy Laminin signal outside VM. Scale bar, 10 μm. In the side views, the

basal side of epithelia is positioned upward. In **c**, **e**, **g**, and **h**, mean±SEMs are shown with individual data points. Data were analyzed by two-tailed unpaired Student's *t*-test. Asterisks indicate statistical significance (*$P<0.01$) and *P*-values are indicated in the graph.

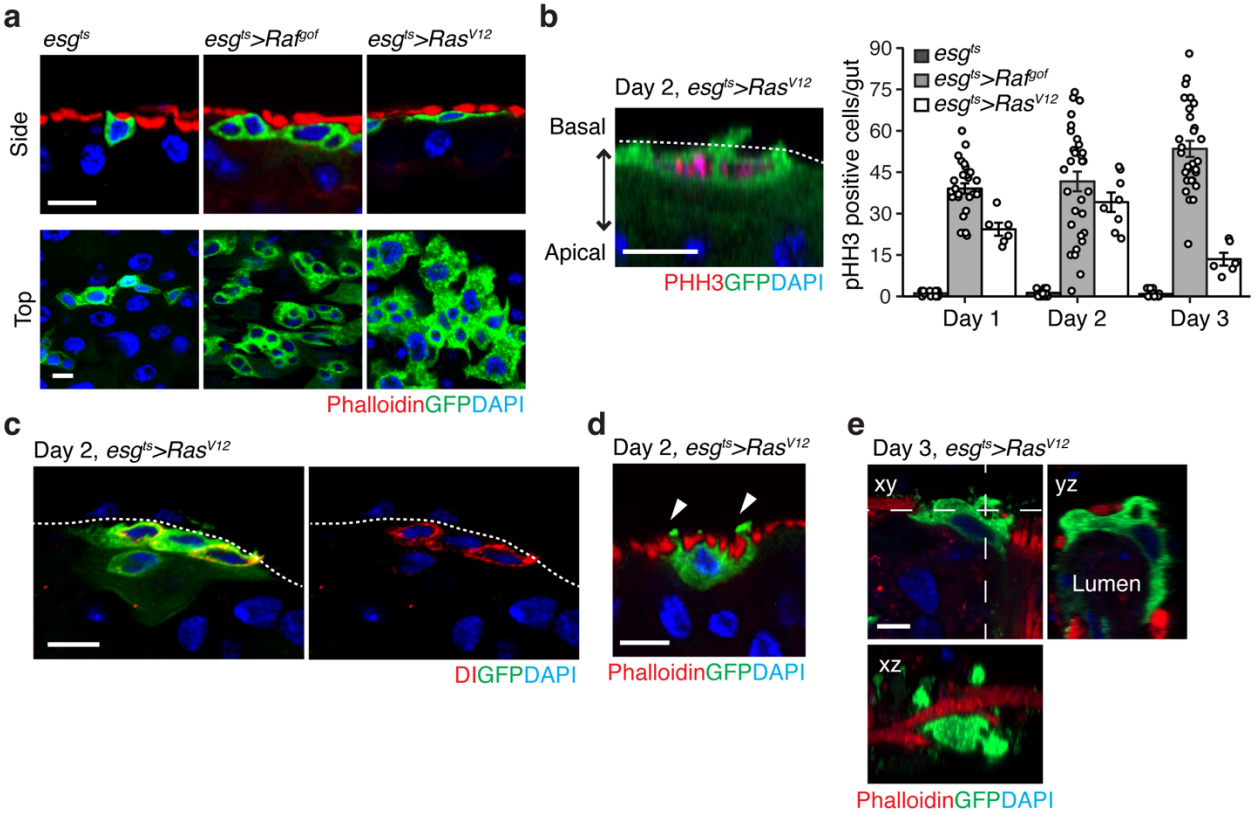
a
esg^ts
esg^ts>Raf^gof
esg^ts>Ras^V12
Side
Top
PhalloidinGFPDAPI
b
Day 2, esg^ts>Ras^V12
Basal
Apical
PHH3GFPDAPI
pHH3 positive cells/gut
90
75
60
45
30
15
0
esg^ts
esg^ts>Raf^gof
esg^ts>Ras^V12
Day 1
Day 2
Day 3
c
Day 2, esg^ts>Ras^V12
DIGFPDAPI
d
Day 2, esg^ts>Ras^V12
PhalloidinGFPDAPI
e
Day 3, esg^ts>Ras^V12
xy
yz
Lumen
xz
PhalloidinGFPDAPI

Figure 2. Disseminating *Ras^{V12}*-transformed cells undergo extensive remodeling of cell morphology.

a, Representative cell morphologies from side and top view. Transgenes were induced for 1 day. Phalloidin signal visualizes VM (red). Scale bars, 10μm. **b,** Representative image of pHH3 (red) staining of *Ras^{V12}* cells and quantification of phospho-histone H3 (pHH3) cells per midgut after 3 days of expression. Prior to staining, *Ras^{V12}* was expressed for 2 days. Dotted line indicates the epithelial boundary. Scale bars, 10μm. For Quantification, Day 1: N=16 (*esg^{ts}*), N=27 (*esg^{ts}>Raf^{gof}*), N=6 (*esg^{ts}>Ras^{V12}*); Day 2: N=14 (*esg^{ts}*), N=31 (*esg^{ts}>Raf^{gof}*), N=8 (*esg^{ts}>Ras^{V12}*); Day 3: N=16 (*esg^{ts}*), N=29 (*esg^{ts}>Raf^{gof}*), N=6 (*esg^{ts}>Ras^{V12}*) biological replicates. Data are mean±SEMs. **c**, Delta (Dl) antibody staining. The Notch receptor ligand Dl—a marker of intestinal stem cells—was detected in *Ras^{V12}* cells. Dotted line indicates the epithelial boundary. *Ras^{V12}* cells are marked with GFP (green), and nuclei are stained with DAPI (blue). Scale bar, 10μm. **d**, Side view of *Ras^{V12}* cell. *Ras^{V12}* was induced for 2 days with *esg^{ts}*. Arrowheads point to protrusions formed across VM. Scale bar, 10μm. **e**, Side (xy) and orthogonal (yz and xz) views of *Ras^{V12}* cell. *Ras^{V12}* was expressed for 3 days. Scale bar, 10μm.

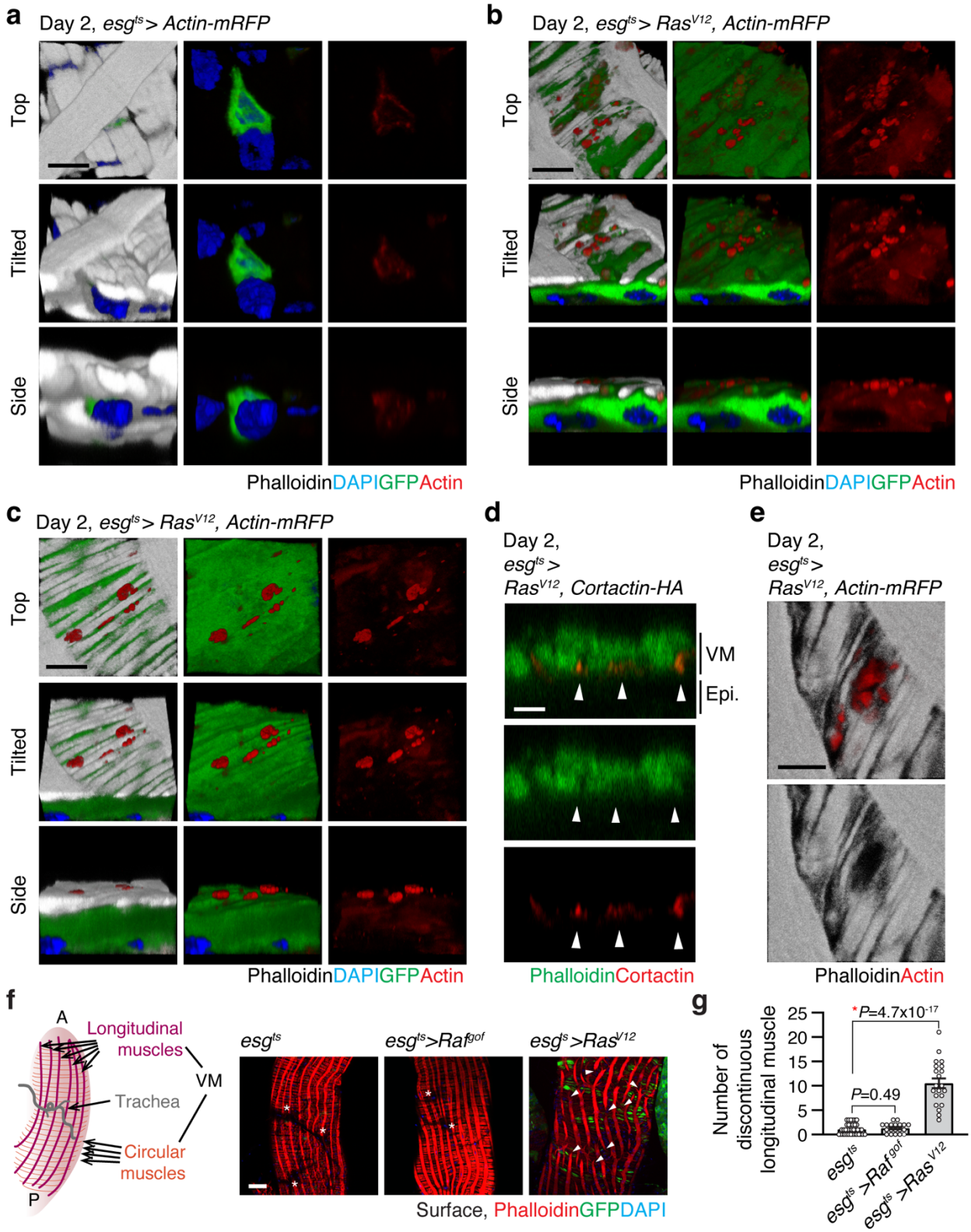
a
Day 2, esg^ts> Actin-mRFP
Top
Tilted
Side
PhalloidinDAPIGFPActin
b
Day 2, esg^ts> Ras^V12, Actin-mRFP
Top
Tilted
Side
PhalloidinDAPIGFPActin
c
Day 2, esg^ts> Ras^V12, Actin-mRFP
Top
Tilted
Side
PhalloidinDAPIGFPActin
d
Day 2,
esg^ts>
Ras^V12, Cortactin-HA
VM
Epi.
PhalloidinCortactin
e
Day 2,
esg^ts>
Ras^V12, Actin-mRFP
PhalloidinActin
f
A
Longitudinal muscles
VM
Trachea
Circular muscles
P
esg^ts
esg^ts>Raf^gof
esg^ts>Ras^V12
Surface, PhalloidinGFPDAPI
g
Number of discontinuous longitudinal muscle
25
20
15
10
5
0
*P=4.7x10^-17
P=0.49
esg^ts
esg^ts >Raf^gof
esg^ts >Ras^V12

Figure 3. Basal Actin-rich protrusions disrupt visceral muscle integrity.

a–**c**, 3D reconstructions of confocal images angled at 0, 45, and 90 degrees for top, tilted, and side views, respectively. Representative images of control cells (**a**), and *Ras^{V12}* cells (**b** and **c**) are shown. Dissected guts are imaged for Actin-mRFP (red), Phalloidin (gray) and DAPI (blue). Scale bars, 5 μm. **d**, Orthogonal view of Cortactin-rich protrusions and VM layer. Arrowheads indicate Cortactin-rich protrusions (red) co-stained with Phalloidin (gray). Scale bar, 5 μm. **e**, Surface view of a rupture in the VM layer induced by a cluster of Actin-rich protrusions (red). Scale bar, 5 μm. N=12 (*esg^{ts}>Actin-mRFP*) for **a** and N=28 (*esg^{ts}>Ras^{V12}, Actin-mRFP*) biological replicates for **b, c, d** and **e**. **f**, Surface views of the posterior midgut. Schematic illustration describes the architecture of the *Drosophila* VM. VM (red) is visualized with Phalloidin. Arrowheads show discontinued longitudinal muscles. The region void of Phalloidin signals (asterisks) is where the trachea is present. Longitudinal and circular-muscles behind trachea are not captured because they are at different focal planes. **g**, Quantification of longitudinal muscle breaks. Discontinuation of longitudinal muscles in one layer of VM in the area captured with 40x objective (388 μm x 388 μm) was counted. N=37 (*esg^{ts}*), N=19 (*esg^{ts}>Raf^{gof}*), N=21 (Day1, *esg^{ts}>Ras^{V12}*) biological replicates. Mean±SEMs are shown with individual data points. Data were analyzed by two-tailed unpaired Student's *t*-test. Asterisks indicate statistical significance (*P<0.01), and P-values are indicated in graph, Transgenes were induced with *esg^{ts}* for 2 days at 29°C. In the side views of **a**-**d**, the basal side of epithelia is positioned upward.

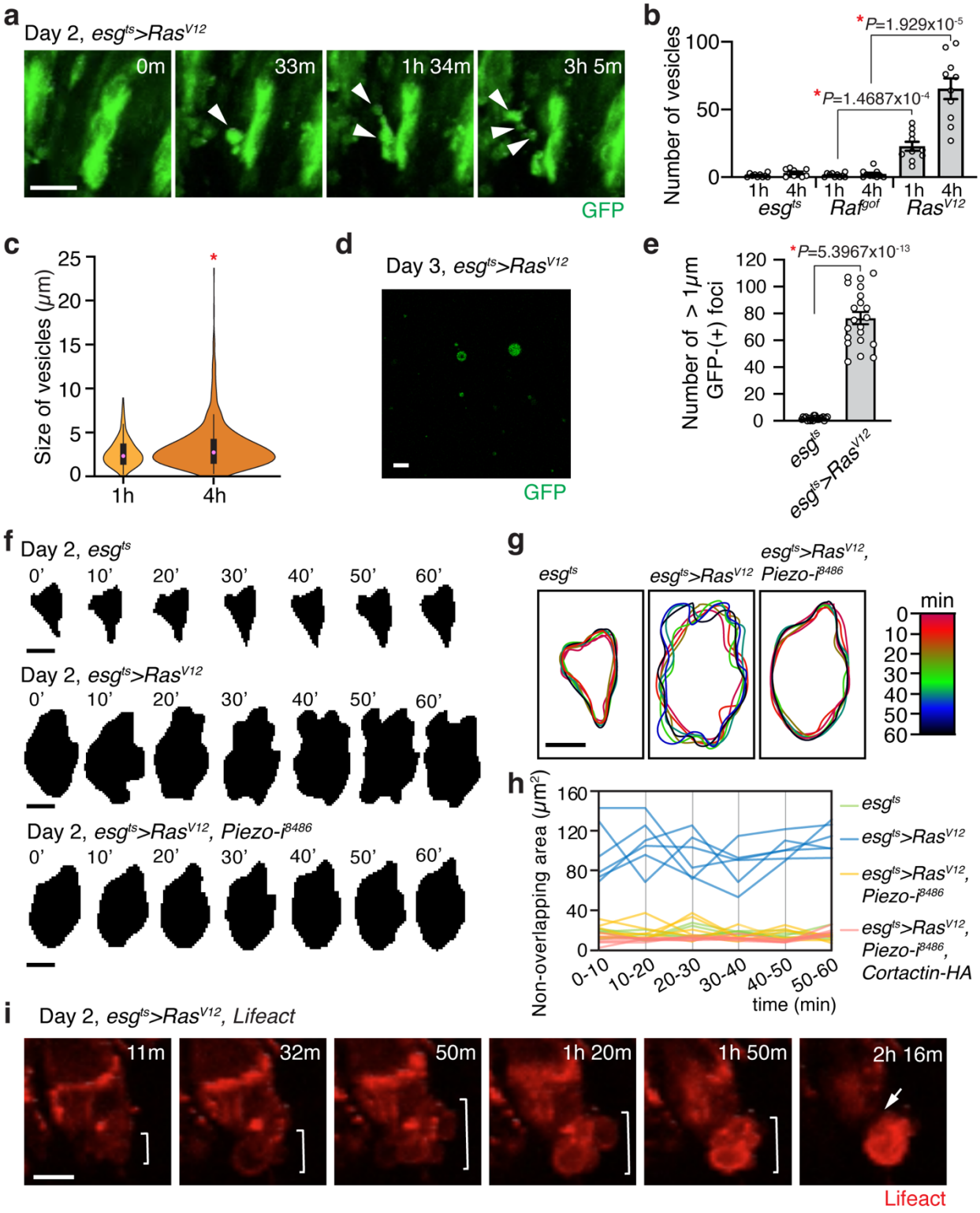
a
Day 2, esg^ts>Ras^V12
0m
33m
1h 34m
3h 5m
GFP
b
Number of vesicles
100
50
0
*P=1.929x10^-5
*P=1.4687x10^-4
1h 4h 1h 4h 1h 4h
esg^ts
Raf^gof
Ras^V12
c
Size of vesicles (μm)
25
20
15
10
5
0
*
1h
4h
d
Day 3, esg^ts>Ras^V12
GFP
e
Number of > 1μm GFP-(+) foci
120
100
80
60
40
20
0
*P=5.3967x10^-13
esg^ts
esg^ts>Ras^V12
f
Day 2, esg^ts
0' 10' 20' 30' 40' 50' 60'
Day 2, esg^ts>Ras^V12
0' 10' 20' 30' 40' 50' 60'
Day 2, esg^ts>Ras^V12, Piezo-i^8486
0' 10' 20' 30' 40' 50' 60'
g
esg^ts
esg^ts>Ras^V12
esg^ts>Ras^V12, Piezo-i^8486
min
0
10
20
30
40
50
60
h
Non-overlapping area (μm^2)
160
120
80
40
0
0-10 10-20 20-30 30-40 40-50 50-60
time (min)
esg^ts
esg^ts>Ras^V12
esg^ts>Ras^V12, Piezo-i^8486
esg^ts>Ras^V12, Piezo-i^8486, Cortactin-HA
i
Day 2, esg^ts>Ras^V12, Lifeact
11m
32m
50m
1h 20m
1h 50m
2h 16m
Lifeact

Figure 4. *Ras^{V12}* cells generate blebs and ELEVs and disseminate by extensive blebbing.

a, Still shots from *ex vivo* live imaging of *esg^{ts}>Ras^{V12}* midgut. Arrowheads indicate blebs and ELEVs. Scale bar, 10 μm. **b**, **c**, Quantification of ELEVs generated from dissected midgut. Transgenes were induced for 2 days with *esg^{ts}*. Number and size of ELEVs produced from dissected midgut were measured at 1h and 4h post incubation in *ex vivo* live imaging media. N=10 biological replicates for each genotype. **b**, Number of ELEVs. **c**, Size of ELEVs. Circles show the medians (1h, 3.0928 μm; 4h, 3.6199 μm); box limits indicate the 25th and 75th percentiles; whiskers extend 1.5 times the interquartile range from the 25th and 75th percentiles. **d**, Representative image of circulating ELEVs. Scale bar, 10 μm. **e**, Quantification of GFP$^+$ particles in hemolymph. Green particles bigger than 1 μm were counted. N=21 from 3 independent experiments for each genotype. **f**–**h**, Outline tracing of representative cells in *esg^{ts}*, *esg^{ts}>Ras^{V12}*, and *esg^{ts}>Ras^{V12}*, *Piezo-i^{8486}* midguts. **f**, Time series of cell boundary masks. The representative cells were traced for an hour from *ex vivo* live-imaging videos. Masks of the cells were generated every 10 minutes. Scale bars, 10 μm. **g**, Overlay of cell outlines. Time series of the cell silhouettes were color-coded and overlaid. Scale bar, 10 μm. **h,** Deviation of cell boundary. Non-overlapping area of two cell silhouettes acquired at consecutive time points (n' and n+10', n = 0', 10', 20', 30', 40', 50') is measured. N=6 for each genotype. **i,** Still shots from *ex vivo* live imaging of *esg^{ts}>Ras^{V12}* midgut. Lifeact is expressed to visualize filamentous actin (red). Brackets indicate blebbing. Arrow points out the detachment of the blebbing cell from the midgut epithelium. Scale bar, 10 μm. In **b** and **e**, mean±SEMs are shown

with individual data points. Data were analyzed by two-tailed unpaired Student's *t*-test. Asterisks indicate statistical significance (*$P<0.01$), and *P*-values are indicated in graph.

Chapter 3. Dissemination of *Ras^{V12}*-transformed cells requires the mechanosensitive channel Piezo

3.1 Disruption of Piezo impairs dissemination of *Ras^{V12}* cells

Given the breach of the BM and VM layers, *Ras^{V12}* cells need to sense the cues associated with it and elicit appropriate cellular responses to successfully transmigrate into the hemocoel. Since degradation of the ECM and ruptures in the VM layers could substantially alter the biomechanical microenvironment, we looked into the role of the mechanosensitive cation channel Piezo in the cell dissemination process.

Disruption of Piezo in *Ras^{V12}* cells using RNA inference (RNAi) lines (NIG#8486R-3 and VDRC#v2796) [39, 40] led to a significant suppression in cell dissemination (Fig. 5a, b). It has been shown that a blocker of mechanically activated cationic currents, gadolinium also efficiently inhibits mouse Piezo1-induced current [41]. We found that feeding gadolinium was also sufficient to suppress dissemination of *Ras^{V12}* cells (Fig. 5c). This suppression could not be simply explained by a reduction in cell number since *Piezo* knockdown did not decrease the number of ISCs nor the division of *Ras^{V12}* cells (Supplementary Fig. 8a–c). Similarly, the division of *Ras^{V12}* cells was not decreased by gadolinium feeding (Supplementary Fig. 8d).

A recent study has demonstrated that Piezo regulates differentiation of enteroendocrine (EE) cells in *Drosophila* midgut [42]. However, we found that the overall EE cell number remained unchanged in *esg^{ts}>Ras^{V12}* midgut, indicating that expression of *Ras^{V12}* did not facilitate production of EEs (Supplementary Fig. 8e–g). Additionally, the

effect of *Piezo* knockdown in Ras^{V12} cells on EE cell population was negligible (Supplementary Fig. 8e–g). Thus, a possible change in EE cell population due to Piezo inhibition cannot account for the suppression of Ras^{V12} cell dissemination.

To determine which process requires Piezo, we scrutinized the cellular phenotypes caused by *Piezo* knockdown. Interestingly, formation of invasive protrusions was not inhibited by *Piezo* knockdown as Lifeact puncta were still detected at the basal side of Ras^{V12}, *Piezo* RNAi cells (Supplementary Fig. 9). In contrast, the muscle-damage phenotype was rescued by *Piezo* knockdown in Ras^{V12} cells, and the large blebs/protrusions detected outside the posterior midguts were almost invisible in the esg^{ts}>Ras^{V12}, *Piezo* RNAi posterior midgut (Fig. 5a, d). Furthermore, we found that *Piezo* knockdown significantly suppressed ELEV production (Fig. 5e and Supplementary Videos 7, 8). Similarly, blebbing cells were no longer detected in the posterior esg^{ts}>Ras^{V12}, *Piezo* RNAi midguts; the boundary of Ras^{V12}, *Piezo* RNAi cells was not altered dramatically over an hour of tracing (Fig. 4f). Altogether, our characterization of the *Piezo* knockdown phenotypes suggests that during dissemination of Ras^{V12} cells, Piezo impinges on two different processes: the breach of the VM layer and the induction of blebbing.

3.2 Piezo plays two discrete roles in Ras^{V12} cell dissemination

Our observations indicate that Actin- and Cortactin-rich invasive protrusions were associated with the breach of the ECM and the VM layer. Given the rescue of muscle-damage by *Piezo* inactivation in Ras^{V12} cells, Piezo might regulate the function of these

invasive protrusions. Since we found that *Cortactin* knockdown in Ras^{V12} cells suppressed the degradation of the ECM (Supplementary Fig. 5a, b), we tested whether *Piezo* knockdown also rescued ECM degradation. Stainings of Laminin B1 showed that Piezo was required for degradation of the ECM by Ras^{V12} cells (Fig. 6a). Furthermore, we found that *Piezo* knockdown rescued the circular-muscle thinning and segregation phenotype caused by Ras^{V12} expression (Fig. 6b). Of importance, *Piezo* knockdown in Ras^{V12} cells greatly reduced Mmp1 levels (Fig. 6c), indicating that Mmp1 expression in Ras^{V12} cells was dependent upon Piezo. Multiple studies have shown that the calcium-dependent proteases Calpains are critical mediators of calcium signaling induced by Piezo channels [43, 44]. To elucidate the role of Calpain in Mmp1 induction, we inactivated *Drosophila Calpain-A* (*CalpA*) and *Calpain-B* (*CalpB*) in Ras^{V12} cells respectively by RNAi approach. We found that knockdown of either *CalpA* or *CalpB* in Ras^{V12} cells significantly reduced Mmp1 levels (Supplementary Fig. 10a, b). Additionally, *Calpain* knockdown in Ras^{V12} cells rescued the muscle-damage phenotype (Supplementary Fig. 10a). Of importance, dissemination of Ras^{V12} cells was almost completely inhibited by inactivation of either *CalpA* or *CalpB* (Supplementary Fig. 10c). Altogether, these results suggest that Piezo is a critical determinant of Mmp1 levels, and Calpains might be a mediator of Piezo-induced calcium signaling in Ras^{V12} cells.

Piezo disruption induces additional distinct phenotypes: reduction in ELEVs and impairment in blebbing. If the molecular function of Piezo during cell dissemination can be attributed solely to the control of Mmp1 expression, the cell dissemination defect caused by *Piezo* knockdown could be rescued by promoting Mmp1 expression. Cortactin

is a key regulator of invadopodia assembly and function in cancer cells, and amplification of *Cortactin* is linked to an increase in metastasis of carcinoma 31, 45. Furthermore, it has been shown that Cortactin overexpression promotes invadopodia function and MMP activity in many types of cancer cells [31]. Given the conservation of the molecular function of Cortactin in the control of Actin assembly, we hypothesized that Cortactin overexpression might rescue the cell dissemination defect caused by *Piezo* knockdown by enhancing the invasive protrusion function. We found that Cortactin overexpression in Ras^{V12}, *Piezo* RNAi cells restored Mmp1 levels (Fig. 6d), the formation of large blebs/protrusions across VM (Fig. 6e), and the VM damage (Fig. 6f) to the extent caused by Ras^{V12} cells. These results suggest that augmentation of Cortactin levels in Ras^{V12} cells was sufficient to promote Mmp1 expression and compromise the integrity of the tissue. Nevertheless, it could not rescue the defect in dissemination of Ras^{V12}, *Piezo* RNAi cells (Fig. 6g), indicating that creating ruptures in the BM and VM layers was not sufficient to induce dissemination of Ras^{V12}, *Piezo* RNAi cells. Of significance, Cortactin overexpression failed to restore ELEV production to the levels of Ras^{V12} cells even though it could slightly increase ELEV formation from Ras^{V12}, *Piezo* RNAi cells (Fig. 6h). Furthermore, Ras^{V12}, *Piezo* RNAi cells failed to produce blebs despite of ectopic Cortactin expression (Fig. 6i and Supplementary Video 9). Time-lapse, outline-tracing of representative cells in the tissue demonstrated that Ras^{V12}, *Piezo* RNAi cells with ectopic Cortactin expression still remained steady and did not exert extensive blebbing (Fig. 4h and Fig. 6i). Altogether, these results suggest that Piezo plays a discrete role in eliciting blebbing, which is a way to transmigrate into the hemocoel.

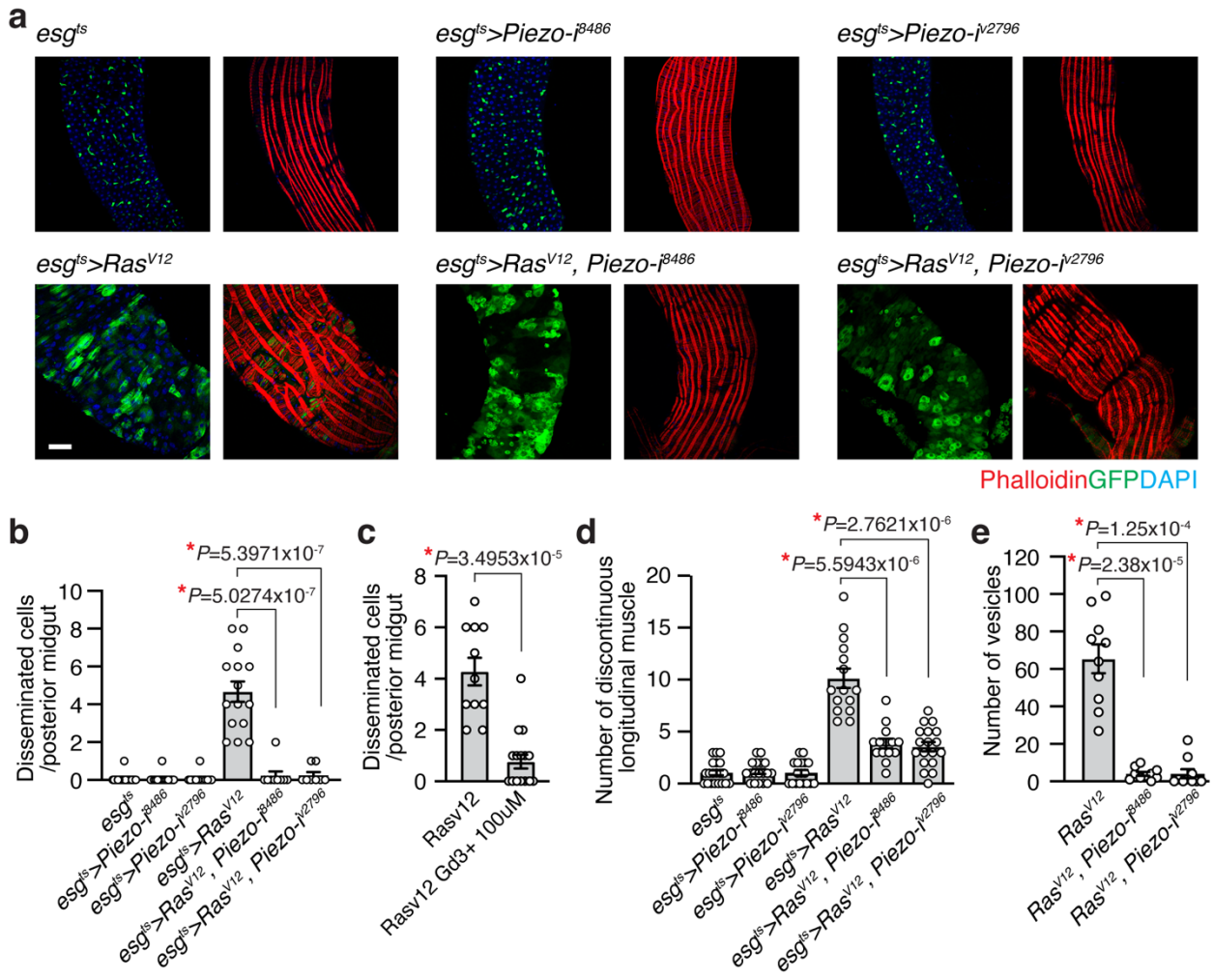
a
esgts
esgts>Piezo-i8486
esgts>Piezo-iv2796
esgts>RasV12
esgts>RasV12, Piezo-i8486
esgts>RasV12, Piezo-iv2796
PhalloidinGFPDAPI
b
Disseminated cells /posterior midgut
*P=5.3971x10-7
*P=5.0274x10-7
esgts
esgts>Piezo-i8486
esgts>Piezo-iv2796
esgts>RasV12
esgts>RasV12, Piezo-i8486
esgts>RasV12, Piezo-iv2796
c
Disseminated cells /posterior midgut
*P=3.4953x10-5
Rasv12
Rasv12 Gd3+ 100uM
d
Number of discontinuous longitudinal muscle
*P=2.7621x10-6
*P=5.5943x10-6
esgts
esgts>Piezo-i8486
esgts>Piezo-iv2796
esgts>RasV12
esgts>RasV12, Piezo-i8486
esgts>RasV12, Piezo-iv2796
e
Number of vesicles
*P=1.25x10-4
*P=2.38x10-5
RasV12
RasV12, Piezo-i8486
RasV12, Piezo-iv2796

Figure 5. The mechanosensory channel Piezo is required for dissemination of *Ras^{V12}* cells.

a, Representative images of posterior midguts. Transgenes were induced for 2 days with *esg^{ts}*. Scale bar, 50 μm. **b**, Quantification of disseminated cells residing on the surface of VM. N=20 (*esg^{ts}*), N=15 (*esg^{ts}>Piezo-i^{8488}*), N=14 (*esg^{ts}>Piezo-i^{v2796}*), N=15 (*esg^{ts}>Ras^{V12}*), N=9 (*esg^{ts}>Ras^{V12}, Piezo-i^{8488}*), N=8 (*esg^{ts}>Ras^{V12}, Piezo-i^{v2796}*) biological replicates. **c**, Quantification of disseminated cells detected on the surface of VM. 100 μM $GdCl_3$-supplemented food was fed for 2 days while expressing *Ras^{V12}* with *esg^{ts}*. N=11 (*esg^{ts}>Ras^{V12}*), N=17 (*esg^{ts}>Ras^{V12}*) biological replicates. **d**, Quantification of discontinuous longitudinal muscles. N=21 (*esg^{ts}*), N=18 (*esg^{ts}>Piezo-i^{8488}*), N=18 (*esg^{ts}>Piezo-i^{v2796}*), N=15 (*esg^{ts}>Ras^{V12}*), N=14 (*esg^{ts}>Ras^{V12}, Piezo-i^{8488}*), N=18 (*esg^{ts}>Ras^{V12}, Piezo-i^{v2796}*) biological replicates. **e**, Quantification of vesicles. N=10 biological replicates for each genotype. *In **b**–**e**,* Mean±SEMs are shown with individual data points. Data were analyzed by two-tailed unpaired Student's *t*-test, asterisks indicate statistical significance (*P<0.01), and P-values are indicated in graph.

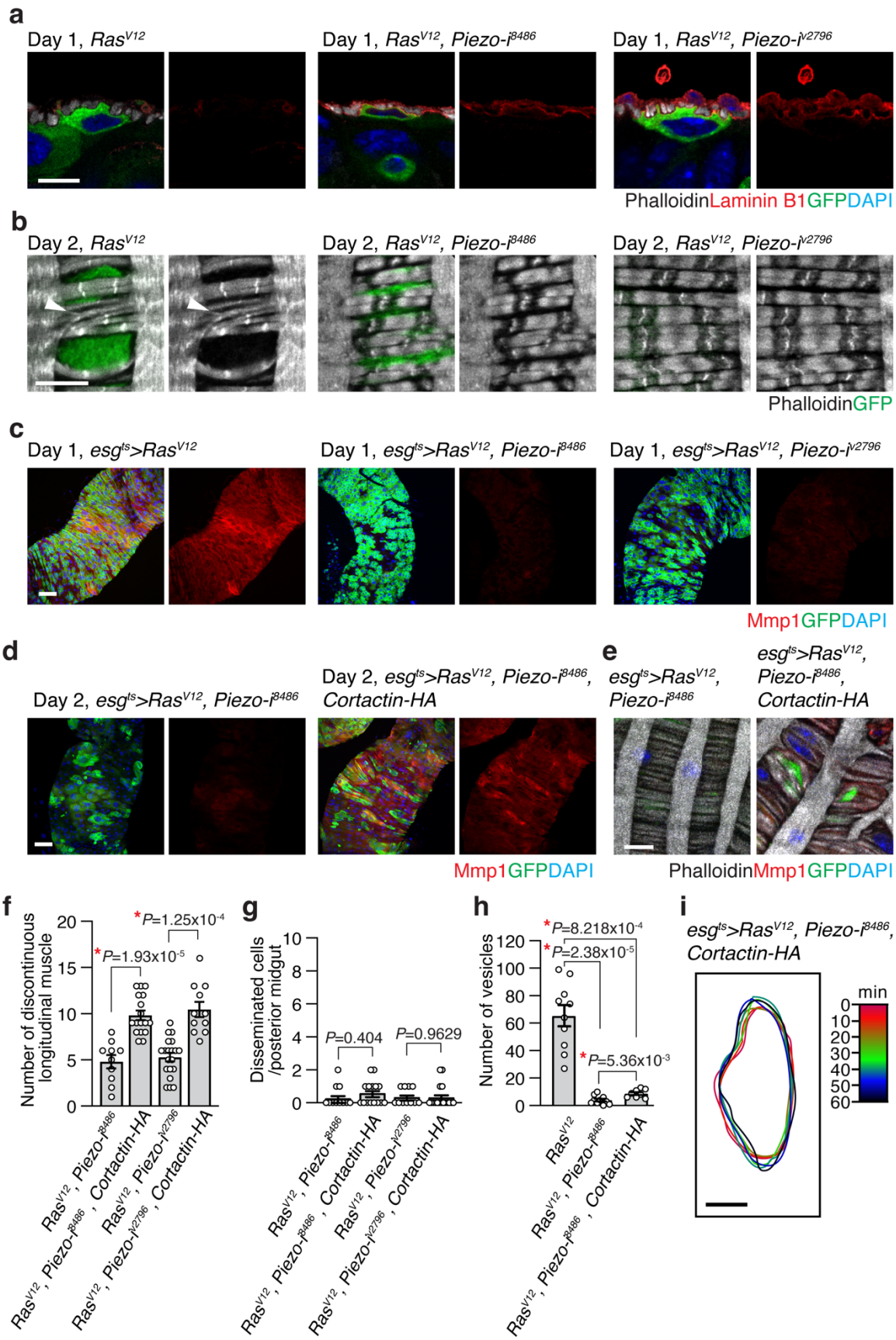
a
Day 1, RasV12
Day 1, RasV12, Piezo-i3486
Day 1, RasV12, Piezo-iv2796
PhalloidinLaminin B1GFPDAPI
b
Day 2, RasV12
Day 2, RasV12, Piezo-i3486
Day 2, RasV12, Piezo-iv2796
PhalloidinGFP
c
Day 1, esgts>RasV12
Day 1, esgts>RasV12, Piezo-i3486
Day 1, esgts>RasV12, Piezo-iv2796
Mmp1GFPDAPI
d
Day 2, esgts>RasV12, Piezo-i3486
Day 2, esgts>RasV12, Piezo-i3486, Cortactin-HA
Mmp1GFPDAPI
e
esgts>RasV12, Piezo-i3486
esgts>RasV12, Piezo-i3486, Cortactin-HA
PhalloidinMmp1GFPDAPI
f
Number of discontinuous longitudinal muscle
*P=1.93x10-5
*P=1.25x10-4
RasV12, Piezo-i3486
RasV12, Piezo-i3486, Cortactin-HA
RasV12, Piezo-iv2796
RasV12, Piezo-iv2796, Cortactin-HA
g
Disseminated cells /posterior midgut
P=0.404
P=0.9629
h
Number of vesicles
*P=8.218x10-4
*P=2.38x10-5
*P=5.36x10-3
RasV12
i
esgts>RasV12, Piezo-i3486, Cortactin-HA
min

Figure 6. Piezo is required for induction of Mmp1 expression and blebbing.

a, Laminin B1 immunostaining (red). The basal side of epithelia is positioned upward. GFP and transgenes were induced for 1 day. Scale bar, 10 μm. **b**, Magnified views of VM (grey). Arrowhead indicates torn circular-muscles. Transgenes were expressed for 2 days. VM is visualized with Phalloidin staining (grey). Scale bar, 10 μm. **c, d**, Mmp1 staining (red) of posterior midguts. Scale bar, 50 μm. **e,** Magnified views of VM (grey). Scale bar, 10 μm. **f,** Quantification of longitudinal muscle break. N=20 (*esg^{ts}> Ras^{V12}, Piezo-i^{8488}*), N=11 (*esg^{ts}> Ras^{V12}, Piezo-i^{8488}, Cortactin-HA*), N=10 (*esg^{ts}> Ras^{V12}, Piezo-i ^{v2796}*), N=17 (*esg^{ts}> Ras^{V12}, Piezo-i ^{v2796}, Cortactin-HA*) biological replicates. **g**, Disseminated cells detected outside VM. N=11 (*esg^{ts}> Ras^{V12}, Piezo-i^{8488}*), N=17 (*esg^{ts}> Ras^{V12}, Piezo-i^{8488}, Cortactin-HA*), N=11 (*esg^{ts}> Ras^{V12}, Piezo-i ^{v2796}*), N=15 (*esg^{ts}> Ras^{V12}, Piezo-i ^{v2796}, Cortactin-HA*) biological replicates. **h**, Quantification of vesicles at 4 h post incubation. The *Ras^{V12}* and *Ras^{V12}, Piezo-i^{8486}* quantifications were adapted from Fig. 5e for comparison. N=10 (*esg^{ts}> Ras^{V12}*), N=10 (*esg^{ts}> Ras^{V12}, Piezo-i^{8488}*), N=8 (*esg^{ts}> Ras^{V12}, Piezo-i^{8488}, Cortactin-HA*) biological replicates. **i**, Overlay of cell outlines. A *Ras^{V12}*, *Piezo* RNAi*, Cortactin-HA* cell in *ex vivo* live-imaging video was traced for an hour. The cell's silhouettes obtained every 10 minutes were overlaid. GFP and other transgenes were induced with *esg^{ts}* for 2 days. Scale bar, 10 μm. In **f**–**h**, Mean±SEMs are shown with individual data points. Data were analyzed by two-tailed unpaired Student's *t*-test. Asterisks indicate statistical significance (*P<0.01), and P-values are indicated in graph.

Chapter 4. Discussion on the in vivo mechanisms of *Ras^{V12}* cell dissemination and the role of Piezo

Although previous studies have demonstrated that *Drosophila* transformed cells can metastasize to distant tissues [8, 12, 14, 16, 17], it has been largely unknown how these transformed cells migrate from their primary site into the hemocoel. Here, we define a series of cellular processes and molecular mechanisms required for cell dissemination in *Drosophila* (Fig. 7). Initially, expression of *Ras^{V12}* in ISCs and EBs allows them propagate. These *Ras^{V12}* cells produce Actin- and Cortactin-rich invasive protrusions at the basal side, which grow into large blebs/protrusions penetrating the BM and VM layers (Fig. 7, stage 2). *Ras^{V12}* cells release ELEVs across the VM layer presumably from where these large blebs/protrusions are formed. Finally, *Ras^{V12}* cells transverse the VM layer by mechanisms involving extensive blebbing or simply slipping through where tissue integrity is compromised (Fig. 7, stage 3) and complete the transmigration process (Fig. 7, stage 4). Note that we did not detect metastasis of *Ras^{V12}* cells although they were found in hemolymph. To metastasize, these cells might require additional genetic alterations to evade anoikis in hemolymph and reactivate cell division in distant tissues, avenues for further investigation. Altogether, our observations demonstrate how multiple invasive and migratory mechanisms are incorporated *in vivo* to form a mode of cell dissemination.

In this study, we describe the Actin- and Cortactin-rich invasive protrusions in *Drosophila*. Our observations show the striking resemblance between these invasive

protrusions and invadopodia observed in cancer cells. In particular, our findings indicate that these invasive protrusions in *Ras^{V12}* cells are associated with the breach of the ECM. In cancer cells, disruption of Cortactin, which is a major component in invadopodia, impaired invadopodia-mediated ECM degradation [31] [30]. Similarly, Cortactin was enriched at the invasive protrusions, and Cortactin depletion in *Ras^{V12}* cells significantly suppressed the ECM degradation (Supplementary Fig. 5a–b) and dissemination of *Ras^{V12}* cells (Supplementary Fig. 5f). These results suggest that the invasive protrusions in *Drosophila* are functionally orthologous to invadopodia observed in cancer cells. Therefore, testing localization of additional invadopodium markers, such as Tyrosine Kinase Substrate with Five SH3 Domains (Tks5), and measuring the release of MMPs at the invasive protrusions will help us to further highlight the resemblance between two invasive protrusions. Interestingly, a robust ECM degradation is a phenotype commonly observed in metastatic tumors in *Drosophila* [12-14, 16, 24]. However, it is unknown whether other transformed *Drosophila* cells also utilize similar invasive protrusions for cell dissemination. Therefore, it would be interesting to address other metastatic cells in *Drosophila*, such as *Ras^{V12}/scrib$^{-/-}$* eye disc tumor cells [12] and *Ras^{V12}*-expressing hindgut epithelial cells [14], utilize a similar invasive structure for cell dissemination.

Our observations suggest that the breach of the ECM and the VM layer associated with the action of the invasive protrusions could be exploited for cell dissemination. *Ras^{V12}* cells transmigrate into the hemocoel through the ruptures in the VM layer by employing extensive blebbing. Additionally, *Ras^{V12}* cells can even slide out from the midgut through the regions that produce ELEVs. Notably, our observations show that some of these

disseminated cells are not originally located near the dissemination site (Supplementary Video 8). Altogether, these observations suggest that the breach of the ECM and VM layers provides an opportunity that nearby cells can utilize for dissemination. Nevertheless, our observations also demonstrate that this opportunity cannot be utilized when Piezo is disrupted (Fig. 6d-i). Given the extensive degradation of the ECM, mesenchymal mode of migration is not a proper migratory strategy that *Ras*^{V12} cells can adopt for dissemination since it requires formation of strong adhesions at the leading edge [37, 46]. Multiple mechanisms that cells use to migrate without support of focal adhesions have been proposed [38]. In particular, bleb-driven amoeboid movement allows cells to pass through holes in the three-dimensional substrate. Interestingly, we found that *Ras*^{V12} cells generate a large amount of ELEVs and blebs, suggesting that *Ras*^{V12} cells adopt bleb-driven amoeboid movement. Notably, Piezo depletion in *Ras*^{V12} cells impaired production of ELEVs and blebs. The breach of the BM and VM layers would cause a significant remodeling of the biomechanical microenvironment. Therefore, we propose that Piezo plays a key role in transducing the opportunistic cues associated with the compromise in the tissue integrity to allow *Ras*^{V12} cells to adapt appropriate migratory modes for dissemination. A recent study demonstrated that confinement and low adhesion could induce amoeboid movement in various mammalian cells [47], which highlighted how the mechanical cues in the substrates influences a cell's migratory strategy. Interestingly, Srivastava et al. (2020) showed that pressure sensing via Piezo makes *Dictyostelium* to generate blebs instead of pseudopods for migration [48]. Thus, it would be interesting to address what environmental cues drive Piezo activation in the

midguts for coordination of the cell's dissemination process.

We elucidated a mode of cell dissemination and uncovered Piezo as a key player of cell dissemination *in vivo*. Piezo disruption interferes with specific cellular phenotypes observed over the course of cell dissemination, indicating that some of the morphologically distinct stages and cellular processes observed during cell dissemination are also genetically discriminable. Given the description of the molecular and cellular mechanisms during an actual cell dissemination process, our study underscores the usefulness of *Drosophila* in deciphering the genetic basis of these invasive mechanisms in a native context.

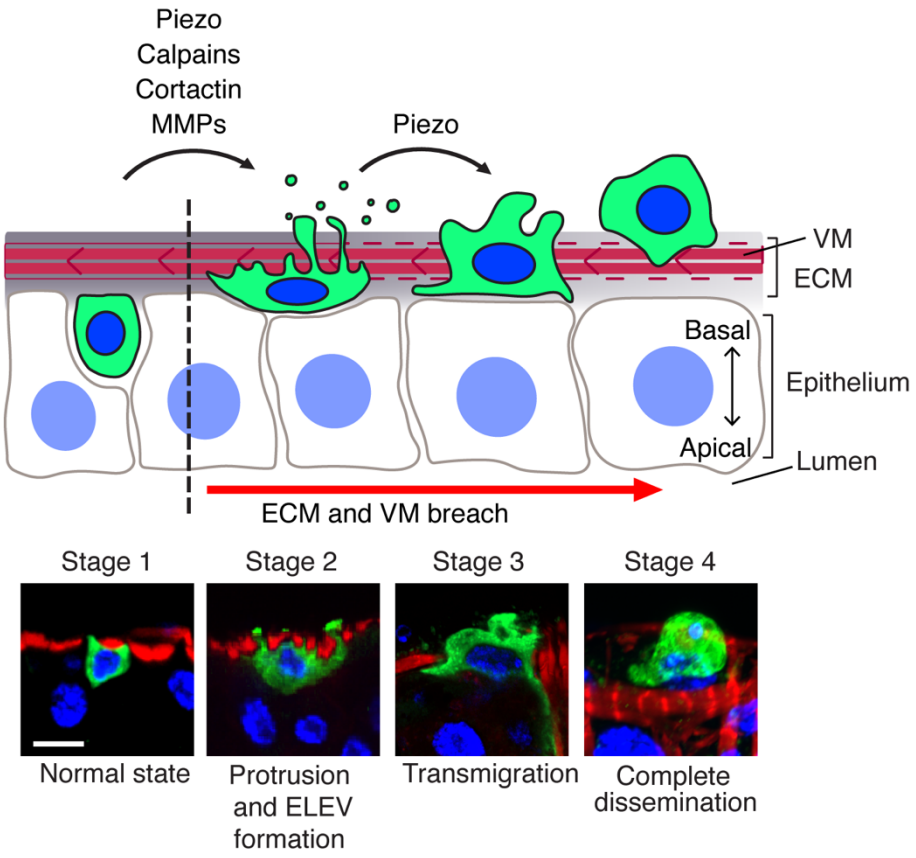
Piezo
Calpains
Cortactin
MMPs
Piezo
VM
ECM
Basal
Epithelium
Apical
Lumen
ECM and VM breach
Stage 1
Stage 2
Stage 3
Stage 4
Normal state
Protrusion and ELEV formation
Transmigration
Complete dissemination

Figure 7. Schematic stages of cell dissemination.

Stages of cell dissemination were reconstituted based on confocal images of fixed Ras^{V12} cells and *ex vivo* live imaging of esg^{ts}>Ras^{V12} posterior midguts. Lower panels show representative confocal images of control (esg^{ts}; stage 1) and Ras^{V12} cells (stage 2-4). An esg^{ts} cell is illustrated in stage 1. In the absence of Ras^{V12} expression, ISCs and EBs reside within the midgut epithelia. Upon Ras^{V12} expression, invasive protrusions are formed at the basal side of the cells, and Mmp1 levels increase. Stage 2 illustrates a Ras^{V12} cell producing large protrusions/blebs and ELEVs across the VM. These cells could be observed at day 2 and 3 of Ras^{V12} expression. Stage 3 and 4 illustrate Ras^{V12} cells under and after transmigration, respectively. Disseminated cells were frequently detected at day 2 and 3 of Ras^{V12} expression. Scale bar, 10 μm.

Chapter 5. Introduction to E-cadherin's complex role in metastasis

E-cadherin (E-cad), the main component of adherens junctions, helps to hold epithelial cells together [49-53]. To invade and migrate, cells disintegrate adherens junctions to free themselves from neighboring cells [51, 54, 55]. When epithelial cells invade and migrate during development, they undergo epithelial mesenchymal transition (EMT), a process that allows them to acquire the properties of mesenchymal cells [56, 57]. Consistent with the role of E-cad, loss of E-cad is considered to be a hallmark of EMT [58, 59]. Frixen et al. showed that loss of E-cad is also important for the ability of carcinoma cells to invade and migrate in culture [60]. These observations coincide with clinical reports, indicating that E-cad is frequently reduced in epithelial cell cancers [61, 62]. Therefore, reduction of E-cad is thought to promote cancer cell invasion and metastasis [60, 63-70]. However, a number of clinical studies have reported that E-cad is expressed in multiple metastatic tumors [71-74]. Notably, Padmanaban et al. have recently demonstrated that E-cad is required for metastasis in multiple invasive ductal carcinoma models by helping cancer cells to survive after dissemination [63], suggesting that E-cad might play a more complicated, not fully defined, role in metastasis of cancer cells.

We attempted to address the role of E-cad in the invasiveness of transformed cells in a native microenvironment by employing our *Drosophila* model of Ras^{V12}-transformed cell dissemination [75]. Expression of Ras^{V12} in adult intestinal stem cells (ISCs) and enteroblasts (EBs) using the conditional GAL4 driver *esg-GAL4*, *UAS-GFP*, $tub\text{-}GAL80^{ts}$

(*esg*^{ts}; see methods) makes *Ras*^{V12}-expressing intestinal epithelial cells (*Ras*^{V12} cells) disseminate basally from the midgut and enter the hemocoel—the primary cavity containing circulatory fluid [75, 76] (Fig. 7). Note that *Ras*^{V12} cells also delaminate apically toward lumen and then are presumably excreted [75]. During dissemination, *Ras*^{V12} cells generate Actin- and Cortactin-rich invasive protrusions functionally and structurally reminiscent of invadopodia observed in cancer cells to breach the ECM and the visceral muscle (VM) layer [27-29, 31, 75]. After compromising the integrity of the ECM and the VM, *Ras*^{V12} cells can then migrate into the circulation by bleb-driven movement. Inactivation of *Cortactin* or the mechanosensitive channel *Piezo* specifically in *Ras*^{V12} cells attenuates dissemination of *Ras*^{V12} cells by impairing their ability to invade and migrate across the ECM and the VM. Thus, this model allows us not only to observe the cell dissemination process in a native context at the cellular and molecular levels, but also to test the function of a gene in the cell dissemination process using the advanced genetic tools available in *Drosophila*.

Our findings demonstrate that E-cad is necessary for the invasiveness of *Ras*^{V12} cells during cell dissemination *in vivo*. Our observations suggest that subcellular E-cad is redistributed in disseminating *Ras*^{V12} cells: E-cad disassembles at adherens junctions—a process that recapitulates the functional consequence of E-cad loss during EMT—and assembles at invasive protrusions, which is not a conventional location for E-cad. We show that two distinct intracellular calcium signaling pathways mediated by the inositol triphosphate receptor (IP3R) and Piezo control disassembly of E-cad at adherens junctions and assembly at invasive protrusions, respectively. Therefore, our study

provides new insights into the role of E-cad in invasiveness and elucidates the mechanisms by which two intracellular calcium signaling pathways differentially control the disassembly and assembly of E-cad to aid cell dissemination.

Chapter 6. Introduction to E-cadherin's complex role in metastasis

6.1 E-cadherin is required for dissemination of *Ras^{V12}* cells

Since our knowledge of the role of E-cad in cell dissemination is limited, we initiated our study by testing whether E-cad is necessary using the *Drosophila Ras^{V12}*-induced cell dissemination model [75]. At day 2 of *Ras^{V12}* expression, disseminated *Ras^{V12}* cells residing at the outer surface of the posterior midguts can be quantified to assess cell dissemination [75]. Inactivation of *Drosophila E-cadherin (DE-cad*; also known as *shotgun* [*shg*]) in *Ras^{V12}* cells by expressing *DE-cad* RNA interference (RNAi) (*JF02769* and *HMS00693*) with *esg^{ts}* did not dramatically alter the overall distribution of *Ras^{V12}* cells in the posterior midguts (Supplementary Fig. 11a). However, *E-cad* inactivation in *Ras^{V12}* cells almost completely eliminated disseminated *Ras^{V12}* cells detected at the outer surface of the posterior midguts (Fig. 8a and b). Given the inverse relationship between E-cad levels and cell migration in cultured cancer cells [60], we also increased DE-cad levels in *Ras^{V12}* cells by expressing *UAS-DE-cad* with *esg^{ts}*. E-cad overexpression only partially reduced dissemination of *Ras^{V12}* cells (Fig. 8b). At day 2 of *Ras^{V12}* expression, *Ras^{V12}* cells also apically delaminate (Fig. 7). Interestingly, *DE-cad* inactivation did not impair apical delamination of *Ras^{V12}* cells (Supplementary Fig. 11b), suggesting that inability to move out from the epithelium was not likely to account for the cell dissemination defect caused by *DE-cad* inactivation in *Ras^{V12}* cells. Altogether, we concluded that E-cad was necessary for cell dissemination.

6.2 The subcellular distribution of DE-cad/Arm is remodeled during *in vivo* cell dissemination

To gain insight into how adherens junctions were affected during cell dissemination, we scrutinized the subcellular distribution of DE-cad in Ras^{V12} cells. At day 1 of Ras^{V12} expression, most of the Ras^{V12} cells stay in the midgut epithelium, resulting in hyperplasia [75]. At day 2, Ras^{V12} cells basally disseminate from the midgut while a significant number of Ras^{V12} cells also delaminate apically toward the lumen [75] (Supplementary Fig. 11b and Fig. 7). When we stained control and Ras^{V12} cells at day 1 with anti-DE-cad antibody, strong signals were detected at the lateral side (Supplementary Fig. 12a), which was recapitulated by staining for the *Drosophila* β-catenin ortholog Armadillo (Arm) (Supplementary Fig. 12b). Since Arm staining yielded much less background signals at the VM (Supplementary Fig. 12a and b, nonspecific signals in the VM layer is indicated with asterisks), we decided to use Arm staining as the primary method to assess E-cad subcellular distribution. At day 2 of Ras^{V12} expression, Arm signals were no longer clearly visible at the lateral side of Ras^{V12} cells while cytoplasmic Arm signals were increased (Fig. 9e, middle section), suggesting that disassembly of adherens junctions rather than reduction in E-cad levels was a mechanism to aid dissemination of Ras^{V12} cells. Notably, we detected Arm signals as discrete puncta at the basal side of Ras^{V12} cells (Fig. 8e, basal section, red arrowheads). These basal Arm signals were not visible in control cells (Fig. 8d) or Ras^{V12} cells at day 1 (Supplementary Fig. 12b). E-cad was also detected as puncta at the basal side of Ras^{V12} cells when we stained with anti-E-cad antibody or used the DE-cad protein-trap line

(*shg*^{mTomato}) producing DE-cad-mTomato under the control of its own promotor (Supplementary Fig. 12c and d). Additionally, Arm colocalized with DE-cad-mRFP at the basal side of *Ras*^{V12} cells (Supplementary Fig. 12d), and *DE-cad* inactivation impaired formation of Arm puncta at the basal side of *Ras*^{V12} cells (Fig. 8f and g, middle sections), indicating that the formation of these puncta was dependent on E-cad. Overexpression of DE-cad did not stabilize adherens junctions nor impair formation of Arm puncta at the basal side of *Ras*^{V12} cells (Fig. 8h, basal and middle sections). Taken together, these observations demonstrate that DE-cad/Arm undergoes extensive remodeling during dissemination of *Ras*^{V12} cells. DE-cad disassembles at adherens junctions and assembles as puncta at the basal side of *Ras*^{V12} cells, which doesn't appear to be simply controlled by DE-cad levels.

6.3 DE-cad/Arm assembles at invasive protrusions and is required for the invasiveness of *Ras*^{V12} cells

The unconventional DE-cad/Arm puncta at the basal side of *Ras*^{V12} cells are reminiscent of *Drosophila* invasive protrusions, which are Actin- and Cortactin-rich protrusions associated with degradation of the ECM and the VM [75]. Thus, we tested whether DE-cad/Arm was localized at invasive protrusions. Considering the possible limitations associated with various Actin markers [32, 77], we decided to use three different Actin reporters, Lifeact-mRFP [77, 78], mCherry-Moe.ABD [79], and Actin-mRFP [80] to visualize invasive protrusions (Fig. 9a, arrowheads). Importantly, Arm signals co-localized to the puncta marked by the Actin markers (Fig. 9a, arrowheads). Thus, these results indicate that DE-cad/Arm is a new component of invasive protrusions.

We then tested whether DE-cad was required for formation of invasive protrusions. Expression of *DE-cad* RNAi with *esg*^{ts} did not alter the formation of Lifeact-RFP puncta at the basal side of *Ras*^{V12} cells (Fig. 9b), indicating that DE-cad is not crucial for the formation of invasive protrusions. Notably, *DE-cad* inactivation impaired *Ras*^{V12} cells' ability to degrade the ECM (Fig. 9c and d). At day 2 of *Ras*^{V12} expression, the Laminin layer was almost completely degraded (Fig. 9c and d). In contrast, the Laminin layer remained intact when *DE-cad* was inactivated in *Ras*^{V12} cells (Fig. 9c and d). *Drosophila* invasive protrusions have been shown to damage the VM layer—manifested by occasional breakages of the longitudinal muscles that normally span the whole posterior part of the midgut [75] (Fig. 9e and f). *DE-cad* inactivation in *Ras*^{V12} cells significantly reduced the longitudinal muscle breakages (Fig. 9e and f). Note that DE-cad overexpression in *Ras*^{V12} cells could not suppress the Laminin degradation or the longitudinal muscle breakage phenotypes (Fig. 9c-f), indicating that an increase in DE-cad levels was not sufficient to impair the function of invasive protrusions. These results show that DE-cad plays an essential role in the invasiveness of *Ras*^{V12} cells by controlling the function of invasive protrusions. Without DE-cad, *Ras*^{V12} cells lose their ability to compromise the ECM and the VM for dissemination.

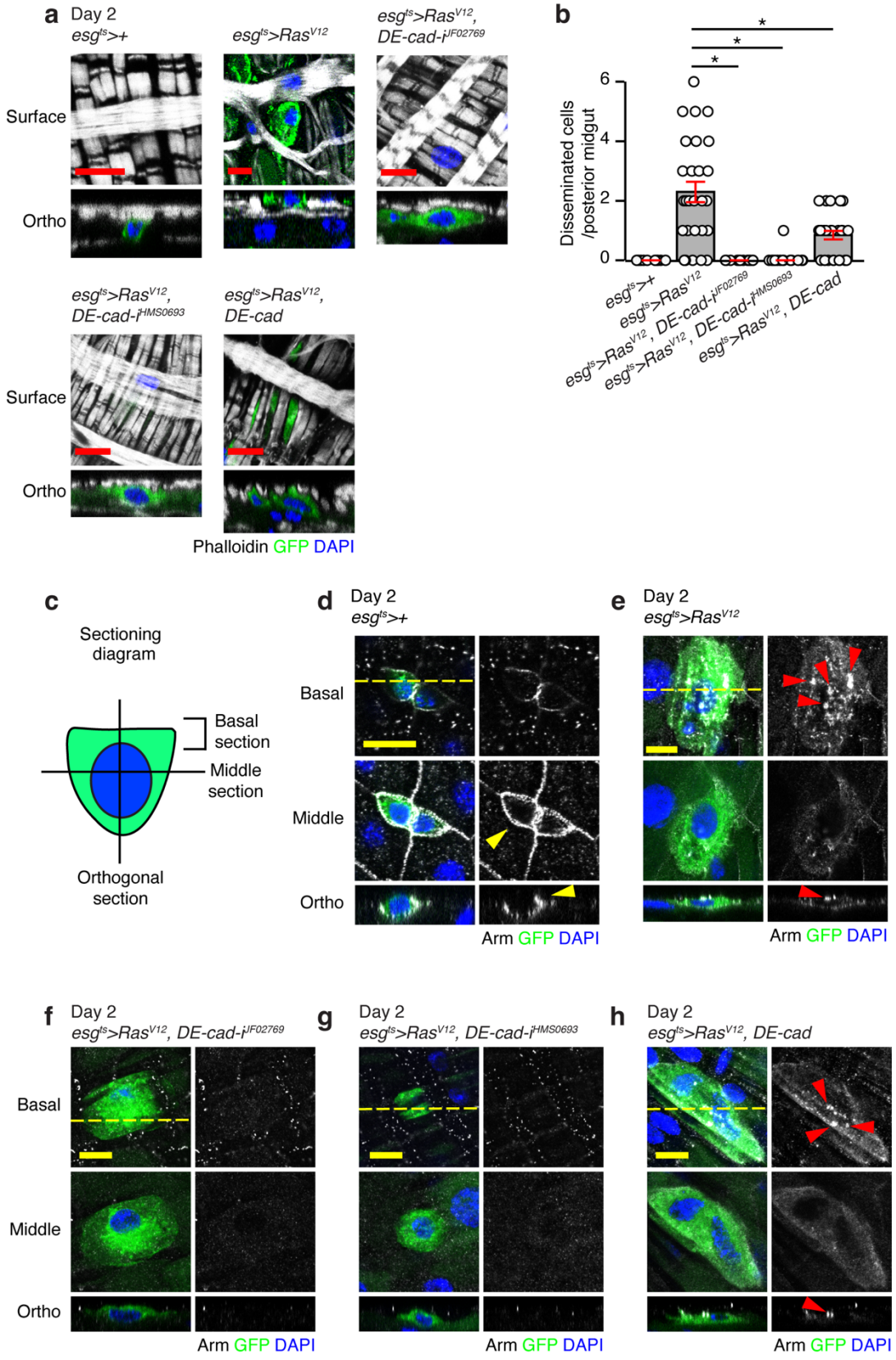
a
Day 2
esg^ts>+
esg^ts>Ras^V12
esg^ts>Ras^V12, DE-cad-i^JF02769
Surface
Ortho
esg^ts>Ras^V12, DE-cad-i^HMS0693
esg^ts>Ras^V12, DE-cad
Surface
Ortho
Phalloidin GFP DAPI
b
Disseminated cells /posterior midgut
0
2
4
6
*
*
*
esg^ts>+
esg^ts>Ras^V12
esg^ts>Ras^V12, DE-cad-i^JF02769
esg^ts>Ras^V12, DE-cad-i^HMS0693
esg^ts>Ras^V12, DE-cad
c
Sectioning diagram
Basal section
Middle section
Orthogonal section
d
Day 2
esg^ts>+
Basal
Middle
Ortho
Arm GFP DAPI
e
Day 2
esg^ts>Ras^V12
Arm GFP DAPI
f
Day 2
esg^ts>Ras^V12, DE-cad-i^JF02769
Basal
Middle
Ortho
Arm GFP DAPI
g
Day 2
esg^ts>Ras^V12, DE-cad-i^HMS0693
Arm GFP DAPI
h
Day 2
esg^ts>Ras^V12, DE-cad
Arm GFP DAPI

Figure 8. DE-cadherin is necessary for cell dissemination.

a, Surface views and orthogonal images of representative cells; *esg^{ts}>+*, control cell residing in the intestinal epithelium; *esg^{ts}>Ras^{V12}*, representative disseminated *Ras^{V12}* cell residing at the outer surface of the visceral muscle; *esg^{ts}>Ras^{V12}, DE-cad-i^{JF02769} and esg^{ts}>Ras^{V12}, DE-cad-i^{JF02769}* cell, representative *DE-cad* inactivated *Ras^{V12}* cells residing in the intestinal epithelium; *esg^{ts}>Ras^{V12}, DE-cad*, representative *Ras^{V12}* cells overexpressing *DE-cad* in the intestinal epithelium. The visceral muscle is visualized with Phalloidin (gray), *ras^{V12}* cells are marked with GFP (green), and nuclei are stained with DAPI (blue). Scale bar, 10 μm. **b,** Quantification of disseminated cells residing on the outer VM surface at the posterior midguts. From left to right, P=4.3971 x 10^{-9} (*Ras^{V12} - Ras^{V12}, DE-cad-i^{JF02769}*), P=1.0966 x 10^{-9} (*Ras^{V12} - Ras^{V12}, DE-cad-i^{HMS0693}*), P= 5.9459 x 10^{-6} (*Ras^{V12} - Ras^{V12}, DE-cad*). n=12 (*esg^{ts}*), n=27 (*esg^{ts}>Ras^{V12}*), n=13 (*esg^{ts}>Ras^{V12}, DE-cad-i^{JF02769}*), n=16 (*esg^{ts}>Ras^{V12}, DE-cad-i^{HMS0693}*), n=26 (*esg^{ts}>Ras^{V12}, DE-cad*) biological replicates. Mean±SEM are shown with individual data points. Statistical analysis was performed using one-way ANOVA with post-hoc Tukey HSD. Asterisks indicate statistical significance (*P<0.05). **c-h,** Representative images of cells stained with anti-Arm antibody (gray). Genotypes are shown. Top images representing the basal section of the cells are projections of 2-4 very basal z-stacks. Middle images show the representative cross sections capturing adherens junctions of the cells. In the orthogonal views, the basal side of cells is positioned upward. Red arrowheads indicate Arm signals detected at cell-cell junctions, and yellow arrowheads indicate Arm signals detected as distinct puncta at the basal side of *Ras^{V12}* cells. Scale bar, 10 μm.

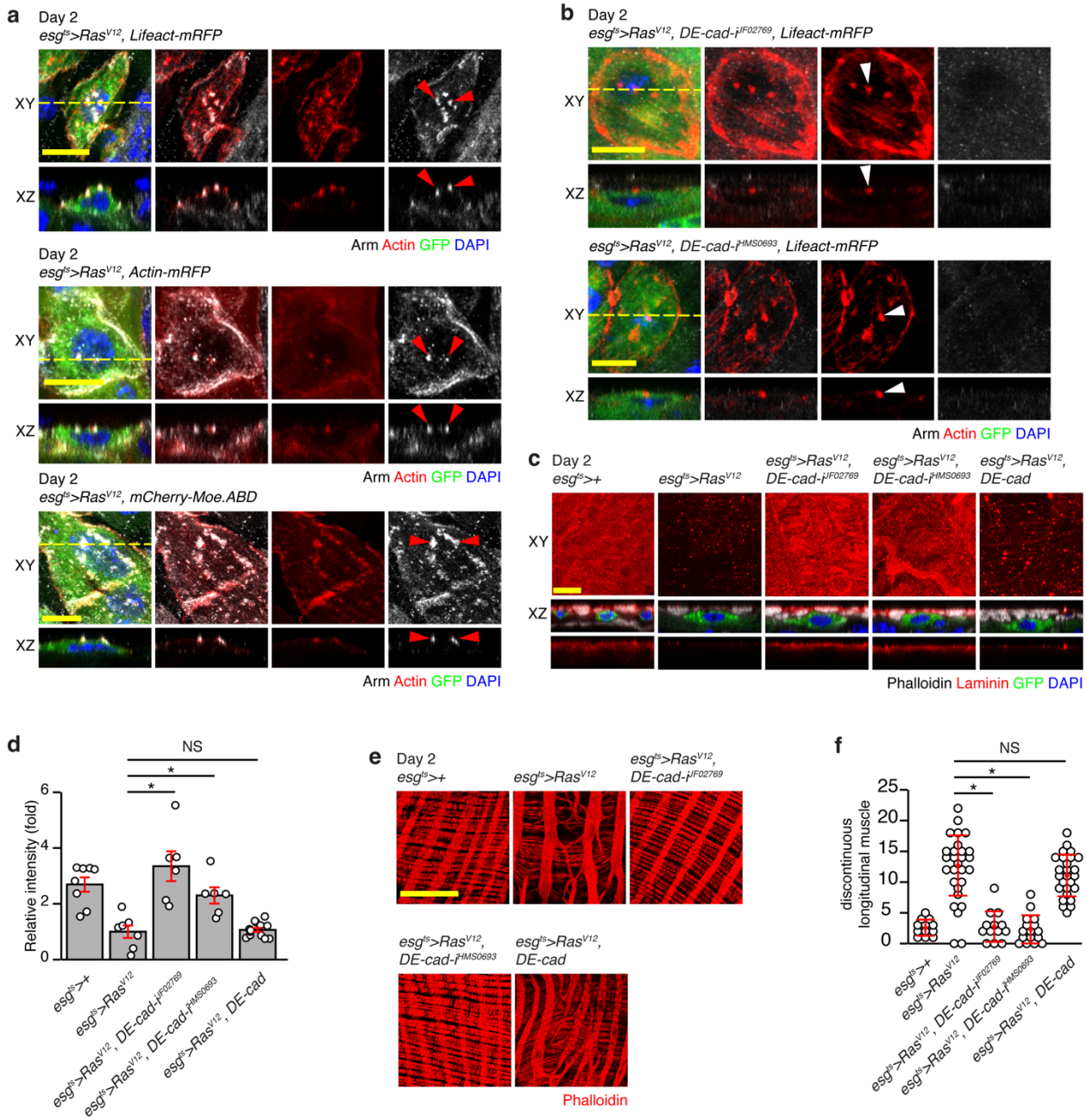
a
Day 2
esg^ts>Ras^V12, Lifeact-mRFP
XY
XZ
Arm Actin GFP DAPI
Day 2
esg^ts>Ras^V12, Actin-mRFP
XY
XZ
Arm Actin GFP DAPI
Day 2
esg^ts>Ras^V12, mCherry-Moe.ABD
XY
XZ
Arm Actin GFP DAPI
b
Day 2
esg^ts>Ras^V12, DE-cad-i^JF02769, Lifeact-mRFP
XY
XZ
esg^ts>Ras^V12, DE-cad-i^HMS0693, Lifeact-mRFP
XY
XZ
Arm Actin GFP DAPI
c
Day 2
esg^ts>+
esg^ts>Ras^V12
esg^ts>Ras^V12, DE-cad-i^JF02769
esg^ts>Ras^V12, DE-cad-i^HMS0693
esg^ts>Ras^V12, DE-cad
XY
XZ
Phalloidin Laminin GFP DAPI
d
NS
*
*
Relative intensity (fold)
6
4
2
0
esg^ts>+
esg^ts>Ras^V12
esg^ts>Ras^V12, DE-cad-i^JF02769
esg^ts>Ras^V12, DE-cad-i^HMS0693
esg^ts>Ras^V12, DE-cad
e
Day 2
esg^ts>+
esg^ts>Ras^V12
esg^ts>Ras^V12, DE-cad-i^JF02769
esg^ts>Ras^V12, DE-cad-i^HMS0693
esg^ts>Ras^V12, DE-cad
Phalloidin
f
NS
*
*
discontinuous longitudinal muscle
25
20
15
10
5
0
esg^ts>+
esg^ts>Ras^V12
esg^ts>Ras^V12, DE-cad-i^JF02769
esg^ts>Ras^V12, DE-cad-i^HMS0693
esg^ts>Ras^V12, DE-cad

Figure 9. DE-cad/Arm assembles at invasive protrusions and controls their function.

a, Basal sections (xy) and orthogonal views (xz) of *Ras^{V12}* cells. Transgenes are induced for 2 days. Actin (red) is visualized *UAS-Lifeact-mRFP, UAS-Actin-mRFP,* and *UAS-mCherry-Moe.ABD*. Arm (gray) was detected by staining with anti-Arm antibody. In the orthogonal views, the basal side of cells is positioned upward. Co-localization of an Actin marker and Arm is indicated with arrowheads. Nuclei are stained with DAPI (blue). Scale bars, 10 μm. **b,** Lifeact-mRFP signals (red) in *Ras^{V12}*, *DE-cad* RNAi cells. Lifeact-mRFP puncta located at the basal side of *Ras^{V12}* cells represent invasive protrusions (arrowheads). Two DE-cad RNAi lines (*JF02769* and *HMS0693*) are used to knockdown *DE-cad* in *Ras^{V12}* cells. Top images (xy), basal sections; bottom images (xz), orthogonal sections. **c,** Laminin B1 staining. Top images, top views (xy); bottom images, orthogonal sections (xz). *Ras^{V12}* cells are marked with GFP (green). All genotypes were stained with anti-Laminin B1 antibody (red), Phalloidin (gray) and DAPI (blue). Scale bars, 10 μm. **d,** Quantification of Laminin B1 signals. From left to right, P=8.9517 x 10^{-06} (*Ras^{V12} - Ras^{V12}, DE-cad-i^{JF02769}*), P=0.0186 (*Ras^{V12} - Ras^{V12}, DE-cad-i^{HMS0693}*), P=0.9996 (*Ras^{V12} - Ras^{V12}, DE-cad*). n=8 (*esg^{ts}*), n=7(*esg^{ts}>Ras^{V12}*), n=6 (*esg^{ts}>Ras^{V12}, DE-cad-i^{JF02769}*), n=6 (*esg^{ts}>Ras^{V12}, DE-cad-i^{HMS0693}*), n=13 (*esg^{ts}>Ras^{V12}, DE-cad*) biological replicates. **e,** Visceral muscle (VM) at the posterior midguts. VM (red) is visualized with phalloidin. Scale bars, 50 μm. **f,** Quantification of longitudinal muscle breaks. From left to right, P=5.4445 x 10^{-13} (*Ras^{V12} - Ras^{V12}, DE-cad-i^{JF02769}*), P=9.2371 x 10^{-14} (*Ras^{V12} - Ras^{V12}, DE-cad-i^{HMS0693}*), P=0.48779 (*Ras^{V12} - Ras^{V12}, DE-cad*). n=12 (*esg^{ts}*), n=27(*esg^{ts}>Ras^{V12}*),

n=13 (*esg*^{ts}>*Ras*^{V12}, *DE-cad-i*^{JF02769}), *n*=16 (*esg*^{ts}>*Ras*^{V12}, *DE-cad-i*^{HMS0693}), *n*=26 (*esg*^{ts}>*Ras*^{V12}, *DE-cad*) biological replicates. In **d** and **f**, mean±SEMs are shown with individual data points. Data were analyzed by using one-way ANOVA with post-hoc Tukey HSD. Asterisks indicate statistical significance (P<0.05). Transgenes were expressed with *esg*^{ts} for 2 days by shifting to 29ºC.

Chapter 7. E-cadherin remodeling during cell dissemination by Piezo and inositol triphosphate receptor (IP3R)

7.1 Intracellular calcium signaling via the PLC-IP3R-CAMK pathway is required for disassembly of DE-cad/Arm at adherens junctions in *Ras^{V12}* cells

Since our findings suggest that the subcellular distribution of DE-cad/Arm is actively remodeled in disseminating cells, we sought to elucidate the signaling mechanisms underlying the remodeling process. Our previous report demonstrated that calcium signaling mediated by the mechanosensitive cation channel Piezo was essential for dissemination of *Ras^{V12}* cells [75], which led us to investigate the importance of intracellular calcium signaling in cell dissemination. IP3R increases cytosolic calcium levels by releasing calcium from the endoplasmic reticulum (ER) in response to its ligand inositol triphosphate (IP_3), which is generated by Phospholipase C (PLC)-mediated cleavage of phosphatidylinositol 4,5-bisphosphate (PIP_2) [81, 82]. At day 2 of *Ras^{V12}* expression, a significant portion of *Ras^{V12}* cells basally disseminate and apically delaminate [75]. Therefore, *Ras^{V12}* cells form tumors at low frequency at day 2 (Fig. 10a and Supplementary Fig. 13a). Interestingly, *IP3R* inactivation made *Ras^{V12}* cells stay in the midguts, resulting in an increase in tumor formation at day 2 (Fig. 10a and Supplementary Fig. 13a). Moreover, *IP3R* inactivation attenuated dissemination (Fig. 10b) and delamination of *Ras^{V12}* cells (Supplementary Fig. 13b). These observations led us to speculate that intracellular calcium signaling mediated by IP3R might be important for disassembly of DE-cad/Arm at adherens junctions. Thus, we attempted to identify the pathway components using tumor growth as a readout. To identify the PLC functioning

upstream of IP3R, we tested all three PLCs in the genome, and found that inactivation of the PLCγ *small wing* (*sl*) in Ras^{V12} cells led to tumor formation (Fig. 10a and Supplementary Fig. 13c). Additionally, inactivation of both *Ca^{2+}/calmodulin-dependent protein kinase* (*CaMK*) *I* and *II* in Ras^{V12} cells induced tumors (Fig. 10a and Supplementary Figure 13a). Knockdown of individual CaMKs in Ras^{V12} cells induced tumors at a low frequency (Supplementary Fig. 13a), suggesting a redundancy in their functions. Notably, inactivation of either *sl* or *CaMKI* and *II* also significantly suppressed dissemination of Ras^{V12} cells (Fig. 10b). These phenotypic similarities suggest that Sl, IP3R, and CaMKs might form a pathway to operate calcium release from the ER in Ras^{V12} cells, which is crucial for dissemination of Ras^{V12} cells.

To address whether the PLC-IP3R-CAMK pathway controls disassembly of DE-cad/Arm at adherens junctions, we assessed the subcellular distribution of Arm in Ras^{V12} cells after depleting each component. In Ras^{V12} cells, Arm signals disappeared from the lateral side (Fig. 10c). In contrast, strong Arm signals were present at the lateral side of Ras^{V12} cells when the PLC-IP3R-CAMK pathway was disrupted (Fig. 10d-h, yellow arrowheads). Arm puncta were almost undetectable at the basal side of Ras^{V12} cells when either *sl* or *IP3R* was inactivated (Fig. 10d-g). When both *CaMKs* were inactivated, basal Arm puncta were only occasionally detected in some Ras^{V12} cells (Fig. 10h and Supplementary Fig. 14). Loss of DE-cad/Arm at invasive protrusions could result in an impairment of invasive protrusion's function. Indeed, inactivation of *sl*, *IP3R*, or *CaMKs* significantly impaired the Ras^{V12} cells' ability to disrupt the VM (Fig. 10i and j). Thus, these observations suggest that the PLC-IP3R-CAMK pathway controls the remodeling of DE-

cad/Arm subcellular distribution in *Ras^{V12}* cells by inducing disassembly of DE-cad/Arm at adherens junctions. Additionally, the loss-of-function phenotypes indicate that the PLC-IP3R-CAMK pathway is also required for localization of DE-cad/Arm to invasive protrusions.

7.2 The Piezo-calpain pathway controls the assembly of DE-cad/Arm at invasive protrusions

Piezo channels can initiate intracellular calcium signaling by transporting Ca^{2+} across the plasma membrane upon sensing mechanical cues in the microenvironment [39, 41, 83, 84]. Previous studies have elucidated the roles of Piezo channels in the invasiveness of transformed cells [43, 48, 75]. In particular, Piezo channels has been shown to control matrix degradation, which is associated with invadopodia function [43, 75]. Nevertheless, the molecular mechanism by which Piezo controls the invasiveness of transformed cells has not been elucidated. Since Piezo activation could increase cytosolic Ca^{2+}, we asked whether inactivation of *Piezo* in *Ras^{V12}* cells affects the redistribution of DE-cad/Arm. Interestingly, when *Piezo* was inactivated in *Ras^{V12}* cells, discrete Arm signals were not detected at the cell boundary, and most of Arm signals were detected in the cytosol (Fig. 11a). The absence of basal Arm puncta in *Ras^{V12}*, *Piezo* RNAi cells indicates that Piezo is required for assembly of DE-cad/Arm at invasive protrusions. Our previous study showed that the calcium-dependent non-lysosomal, cysteine proteases, calpains, worked with Piezo to control the function of invasive protrusion and increase matrix metalloproteinase 1 (Mmp1) expression in *Ras^{V12}* cells [75, 83]. Inactivation of *Calpain-A* (*CalpA*) was also sufficient to recapitulate the Arm subcellular distribution observed in

Ras^{V12}, *Piezo* RNAi cells (Fig. 11a), suggesting that calpains might transduce the calcium signaling induced by Piezo activation. The absence of Arm signals at adherens junctions could be caused by an impairment in either assembly of DE-cad/Arm or maintenance of existing DE-cad/Arm. To gain further insight, we assessed the effect of *Piezo* inactivation on adherens junctions at day 1 of *Ras*^{V12} expression when adherens junctions were not disassembled (Fig. 11b and Supplementary Figure 12b). Interestingly, Arm signals were not clearly visible at the lateral side of *Ras*^{V12} cells even at day 1 when *Piezo* was inactivated (Fig. 11b). These observations support that an impairment in assembly of DE-cad/Arm at adherens junctions is likely to be responsible for the absence of Arm signals at the lateral side of *Ras*^{V12}, *Piezo* RNAi cells. Altogether, our results demonstrate that the Piezo-calpain pathway is required for assembly of DE-cad/Arm at invasive protrusions, implying that calcium signaling mediated by the Piezo-calpain pathway plays a distinct role in the DE-cad/Arm remodeling process. Considering the essential role of DE-cad in the function of invasive protrusions (Fig. 9), we propose that controlling the assembly of DE-cad/Arm at invasive protrusions is the molecular mechanism by which Piezo controls the invasiveness of *Ras*^{V12} cells.

7.3 An increase in cytosolic Ca^{2+} induces disassembly of DE-cad/Arm at adherens junctions

Our observations suggest that the two calcium signaling pathways—the PLC-IP3R-CAMK pathway and the Piezo-calpain pathway—elicit distinct effects on DE-cad/Arm redistribution in disseminating cells. To gain further insights into the roles of the calcium signaling pathways, we decided to assess the acute responses to manipulation

of calcium signaling *ex vivo*. At day 1 of Ras^{V12} expression, DE-cad/Arm is not disassembled from adherens junctions or assembled at invasive protrusions (Supplementary Fig. 12b). Thus, we attempted to assess how pharmacological manipulation of calcium signaling affects the Arm localization in Ras^{V12} cells at day 1 of Ras^{V12} expression. Sarco/endoplasmic reticulum Ca^{2+}-ATPase (SERCA) transports Ca^{2+} from the cytosol to the ER, which keeps cytosolic Ca^{2+} concentration low [85]. Thus, inhibition of SERCA leads to an increase in cytosolic Ca^{2+} and a depletion of Ca^{2+} in the ER. Thus, we used the inhibitor of SERCA, thapsigargin (TG), to induce a global increase in cytosolic Ca^{2+} [86]. To inhibit Piezo-mediated calcium entry, we used gadolinium chloride ($GdCl_3$), which inhibits the mechanically activated cationic currents [41]. When we incubated day 1 Ras^{V12} midguts in control media, Arm signals at adherens junctions were well-preserved (Fig. 12a-c, H_2O and DMSO). Strikingly, Arm signals were no longer concentrated at the lateral side of Ras^{V12} cells when Ras^{V12} midguts were treated with TG for 30 minutes (Fig. 12b and c), indicating that an increase in cytosolic Ca^{2+} is sufficient to induce disassembly of DE-cad/Arm from adherens junctions in Ras^{V12} cells. Although *Piezo* inactivation caused a loss of Arm signals from the lateral side of Ras^{V12} cells *in vivo* (Fig. 11b), transient $GdCl_3$ treatment did not yield any discernable changes in Arm signals at the lateral side of Ras^{V12} cells (Fig. 12b and c), suggesting that inhibition of Piezo doesn't delocalize DE-cad/Arm already existing at adherens junctions. Addition of $GdCl_3$ did not significantly inhibit the TG-induced delocalization of Arm from the lateral side of Ras^{V12} cells (Fig. 12b and c). Thus, Piezo does not contribute to the TG-induced disassembly of DE-cad/Arm at adherens junctions. These observations further support

that Ca^{2+} release from ER via the PLC-IP3R-CAMK pathway plays a role in disassembly of DE-cad/Arm from adherens junctions. Notably, the results gained with $GdCl_3$ treatment indicate that Ca^{2+} entry via Piezo is not required for disassembly or maintenance of DE-cad/Arm at adherens junctions, further supporting that the loss of Arm signals at the lateral side induced by Piezo knockdown (Fig. 11) is caused by an impairment of assembly of DE-cad/Arm at adherens junctions.

7.4 *Ex vivo* gadolinium treatments suggest that Piezo activity is required for assembly of DE-cad/Arm at the basal side and adherens junctions of Ras^{V12} cells

Interestingly, we observed a marginal, yet significant, decrease in the ratio of basal and junctional Arm signals in Ras^{V12} cells in TG+$GdCl_3$ treatment compared to TG treatment (Fig. 12d). Considering that the junctional/cytosol Arm ratios remained comparable between the TG and TG+$GdCl_3$ treatments (Fig. 12c), the change in the basal/junctional Arm ratio might be due to a decrease in Arm signals at the basal side. This raises an interesting possibility that Piezo might be required for localization of DE-cad/Arm at the basal side after disruption of adherens junctions. Since the presence of TG might cause a continuous disassembly of DE-cad/Arm at adherens junctions and the basal side, we designed a sequential treatment regimen whereby TG was washed out after a 30-minute treatment, and then the midguts were incubated in media either with or without $GdCl_3$ for 30 minutes, which would allow Ras^{V12} cells to recover from the effect of TG, with or without Piezo activity (Fig. 12e). Resting TG-treated Ras^{V12} midguts in media without TG induced strong Arm signals at the basal side of Ras^{V12} cells (Fig. 12f and g), suggesting that resting followed by cytosolic Ca^{2+} increase could induce an assembly of

DE-cad/Arm at the basal side. In contrast, resting the TG-treated midguts in media with $GdCl_3$ failed to assemble Arm at the basal side (Fig. 12f and g), indicating that the mechanosensitive channel activities were required for the basal DE-cad/Arm assembly. Note that the Arm signals at the basal side were not detected as discrete puncta, which might be due to a limitation in recapitulating the native circumstance in our *ex vivo* setting. For instance, considering that DE-cad was not required for formation of invasive protrusions (Fig. 9b), assembly of DE-cad/Arm at invasive protrusions might require additional factors, which were not present at day 1 of Ras^{V12} expression. Additionally, resting the TG-treated midguts in media without $GdCl_3$ increased Arm signals at the lateral side of Ras^{V12} cells, which was not observed when incubated in media with $GdCl_3$ (Fig. 12c and h). Interestingly, incubating the TG-treated midguts in media with $GdCl_3$ significantly increased apical delamination of Ras^{V12} cells (Fig. 12i and j). Previously, it was shown that E-cad was endocytosed from the cell-cell junctions during apical extrusion of Ras^{V12}-transformed mammalian cells [87]. Consistently, apical delamination of Ras^{V12} cells was predominantly observed at day 2 of Ras^{V12} expression when adherens junctions were disrupted [75]. Thus, further disruption of adherens junctions might account for the increase in apical delamination observed when the TG-treated midguts that were incubated in media with $GdCl_3$ (Fig. 12i and j). These results further support that Piezo-mediated calcium signaling is also required for assembly of DE-cad/Arm at adherens junctions. Taken together, our study suggests that the general role of Piezo might be to assemble DE-cad/Arm at the designated compartments depending on the cellular context.

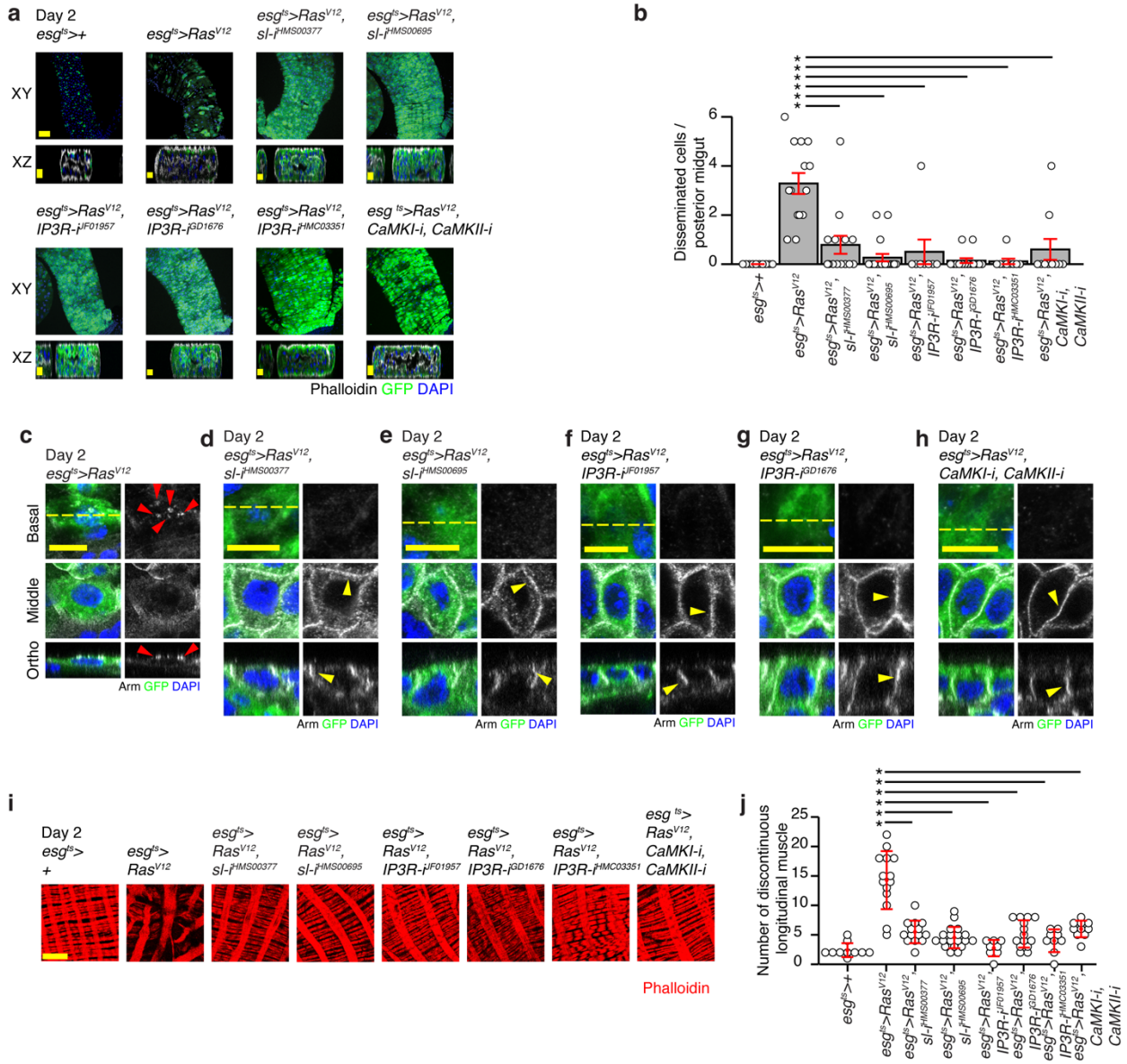
a
Day 2
esg^ts>+
esg^ts>Ras^V12
esg^ts>Ras^V12, sl-i^HMS00377
esg^ts>Ras^V12, sl-i^HMS00695
XY
XZ
esg^ts>Ras^V12, IP3R-i^JF01957
esg^ts>Ras^V12, IP3R-i^GD1676
esg^ts>Ras^V12, IP3R-i^HMC03351
esg ^ts>Ras^V12, CaMKI-i, CaMKII-i
Phalloidin GFP DAPI
b
Disseminated cells / posterior midgut
0
2
4
6
esg^ts>+
esg^ts>Ras^V12
esg^ts>Ras^V12, sl-i^HMS00377
esg^ts>Ras^V12, sl-i^HMS00695
esg^ts>Ras^V12, IP3R-i^JF01957
esg^ts>Ras^V12, IP3R-i^GD1676
esg^ts>Ras^V12, IP3R-i^HMC03351
esg^ts>Ras^V12, CaMKI-i, CaMKII-i
c
Day 2
esg^ts>Ras^V12
Basal
Middle
Ortho
Arm GFP DAPI
d
Day 2
esg^ts>Ras^V12, sl-i^HMS00377
e
Day 2
esg^ts>Ras^V12, sl-i^HMS00695
f
Day 2
esg^ts>Ras^V12, IP3R-i^JF01957
g
Day 2
esg^ts>Ras^V12, IP3R-i^GD1676
h
Day 2
esg^ts>Ras^V12, CaMKI-i, CaMKII-i
i
Day 2
esg^ts>+
esg^ts>Ras^V12
esg^ts>Ras^V12, sl-i^HMS00377
esg^ts>Ras^V12, sl-i^HMS00695
esg^ts>Ras^V12, IP3R-i^JF01957
esg^ts>Ras^V12, IP3R-i^GD1676
esg^ts>Ras^V12, IP3R-i^HMC03351
esg ^ts>Ras^V12, CaMKI-i, CaMKII-i
Phalloidin
j
Number of discontinuous longitudinal muscle
0
5
10
15
20
25
esg^ts>+
esg^ts>Ras^V12
esg^ts>Ras^V12, sl-i^HMS00377
esg^ts>Ras^V12, sl-i^HMS00695
esg^ts>Ras^V12, IP3R-i^JF01957
esg^ts>Ras^V12, IP3R-i^GD1676
esg^ts>Ras^V12, IP3R-i^HMC03351
esg^ts>Ras^V12, CaMKI-i, CaMKII-i

Figure 10. The PLC-IP3R-CAMK pathway is required for DE-cad/Arm disassembly from adherens junctions and assembly at invasive protrusions.

a, Representative images of the posterior midgut showing tumor morphologies at day 2 of transgene expression with *esg^{ts}*. *Ras^{V12}* cells are marked with GFP (green), and nuclei are stained with DAPI (blue). VM is visualized with phalloidin (gray). Bottom panels are representative orthogonal views of the midguts. Scale bars, x: 50 μm and y: 10 μm. **b,** Quantification of disseminated cells. From left to right, P=3.0567 x 10^{-10} (*Ras^{V12} - Ras^{V12}, sl-i^{HMS00377}*), P=7.3386 x 10^{-14} (*Ras^{V12} - Ras^{V12}, sl-i^{HMS00695}*), P=2.2458 x 10^{-09} (*Ras^{V12} - Ras^{V12}, IP3R-i^{JF01957}*), P=8.1712 x 10^{-14} (*Ras^{V12} - Ras^{V12}, IP3R-i^{GD1676}*), P=1.9582 x 10^{-12} (*Ras^{V12} -Ras^{V12}, IP3R-i^{HMC03351}*), P=6.6618 x 10^{-10} (*Ras^{V12} - Ras^{V12}, CaMKI-i, CaMKII-i*). **c-h,** Arm staining. All genotypes were stained with anti-Arm antibody (gray) and DAPI (blue). *Ras^{V12}* cells are marked with GFP (green). Red arrowheads indicate basal Arm signal puncta, and yellow arrowheads show Arm signals at cell-cell junctions. Scale bar, 10 μm. **i**. VM detected by phalloidin staining (red). Scale bar, 25 μm. **J,** Quantification of longitudinal muscle breaks. From left to right, P=1.1258 x 10^{-13} (*Ras^{V12} - Ras^{V12}, sl-i^{HMS00377}*), P=2.7534 x 10^{-14} (*Ras^{V12} - Ras^{V12}, sl-i^{HMS00695}*), P=5.9730 x 10^{-14} (*Ras^{V12} - Ras^{V12}, IP3R-i^{JF01957}*), P=7.8271 x 10^{-14} (*Ras^{V12} - Ras^{V12}, IP3R-i^{GD1676}*), P=7.6605 x 10^{-14} (*Ras^{V12} - Ras^{V12}, IP3R-i^{HMC03351}*), P=4.3077 x 10^{-11} (*Ras^{V12} - Ras^{V12}, CaMKI-i, CaMKII-i*). In **b** and **j**, n=10 (*esg^{ts}*), n=14 (*esg^{ts}>Ras^{V12}*), n=14 (*esg^{ts}>Ras^{V12}, sl-i^{HMS00377}*), n=19 (*esg^{ts}>Ras^{V12}, sl-i^{HMS00695}*), n=8 (*esg^{ts}>Ras^{V12}, IP3R-i^{JF01957}*), n=14 (*esg^{ts}>Ras^{V12}, IP3R-i^{GD1676}*), n=9 (*esg^{ts}>Ras^{V12}, IP3R-i^{HMC03351}*), n=10 (*esg^{ts}>Ras^{V12}, CaMKI-i, CaMKII-i*) biological replicates. Mean±SEMs are shown with individual data points. Statistical

analysis was performed using one-way ANOVA with post-hoc Tukey HSD. Asterisks indicate statistical significance (*P<0.05). In all panels, transgenes are induced with *esg*^{ts} for 2 days at 29°C.

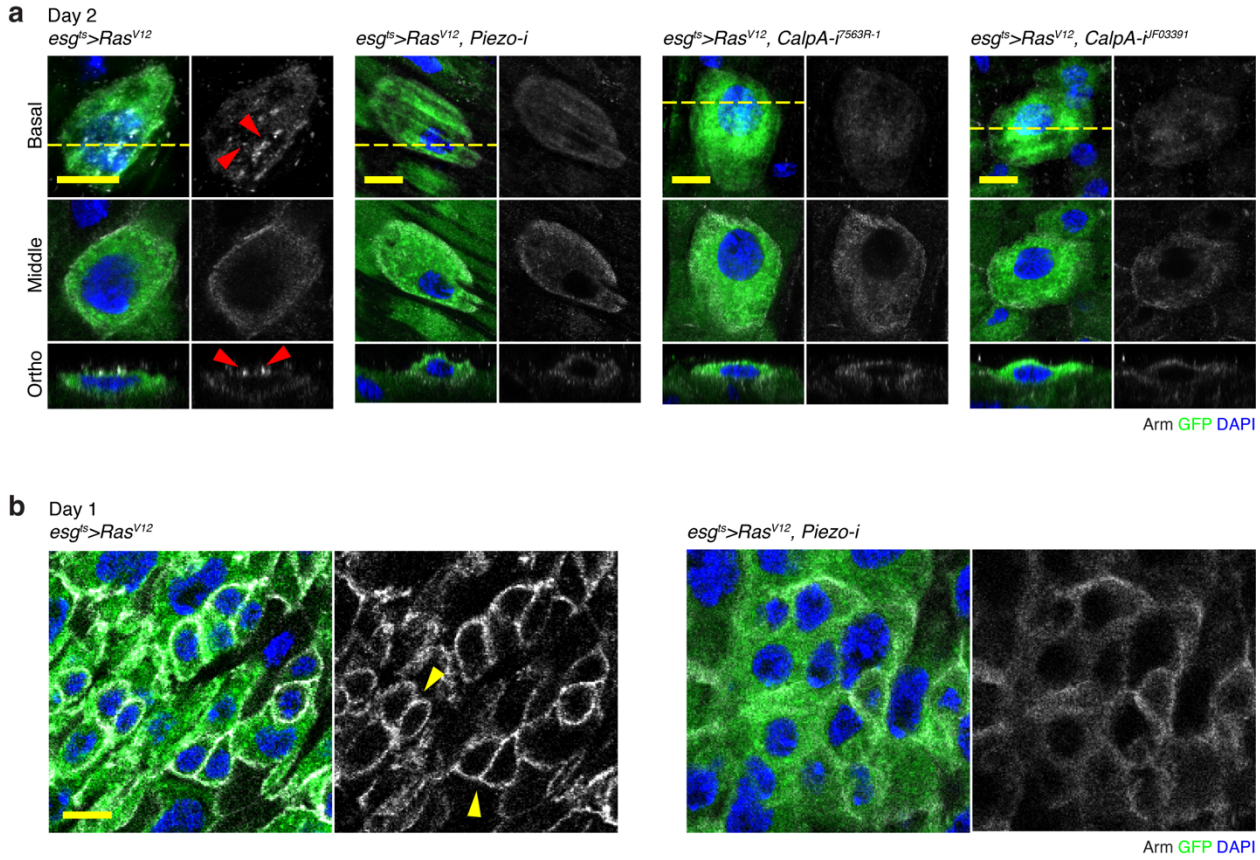
a
Day 2
esg^ts>Ras^V12
esg^ts>Ras^V12, Piezo-i
esg^ts>Ras^V12, CalpA-i^7563R-1
esg^ts>Ras^V12, CalpA-i^JF03391
Basal
Middle
Ortho
Arm GFP DAPI
b
Day 1
esg^ts>Ras^V12
esg^ts>Ras^V12, Piezo-i
Arm GFP DAPI

Figure 11. The Piezo-calpain pathway is required for assembly of DE-cad/Arm at invasive protrusions.

a, Representative images of the basal, middle, and orthogonal sections of cells stained with anti-Arm antibody (gray). Arrowheads indicate Arm signals at invasive protrusions. The *Piezo* RNAi line (8486R-3) is also used in our previous study [75], and two RNAi lines (7563R-1 and JF03391) are used to knockdown *CalpA*. Transgenes were induced for 2 days with *esg*^{ts}. Nuclei are stained with DAPI (blue). Scale bar, 10 μm. **b,** Arm staining (gray) of the midguts at day 1 of transgene expression with *esg*^{ts}. DAPI (blue) marks nuclei. Junctions are indicated by arrowhead (yellow). Scale bar, 10 μm.

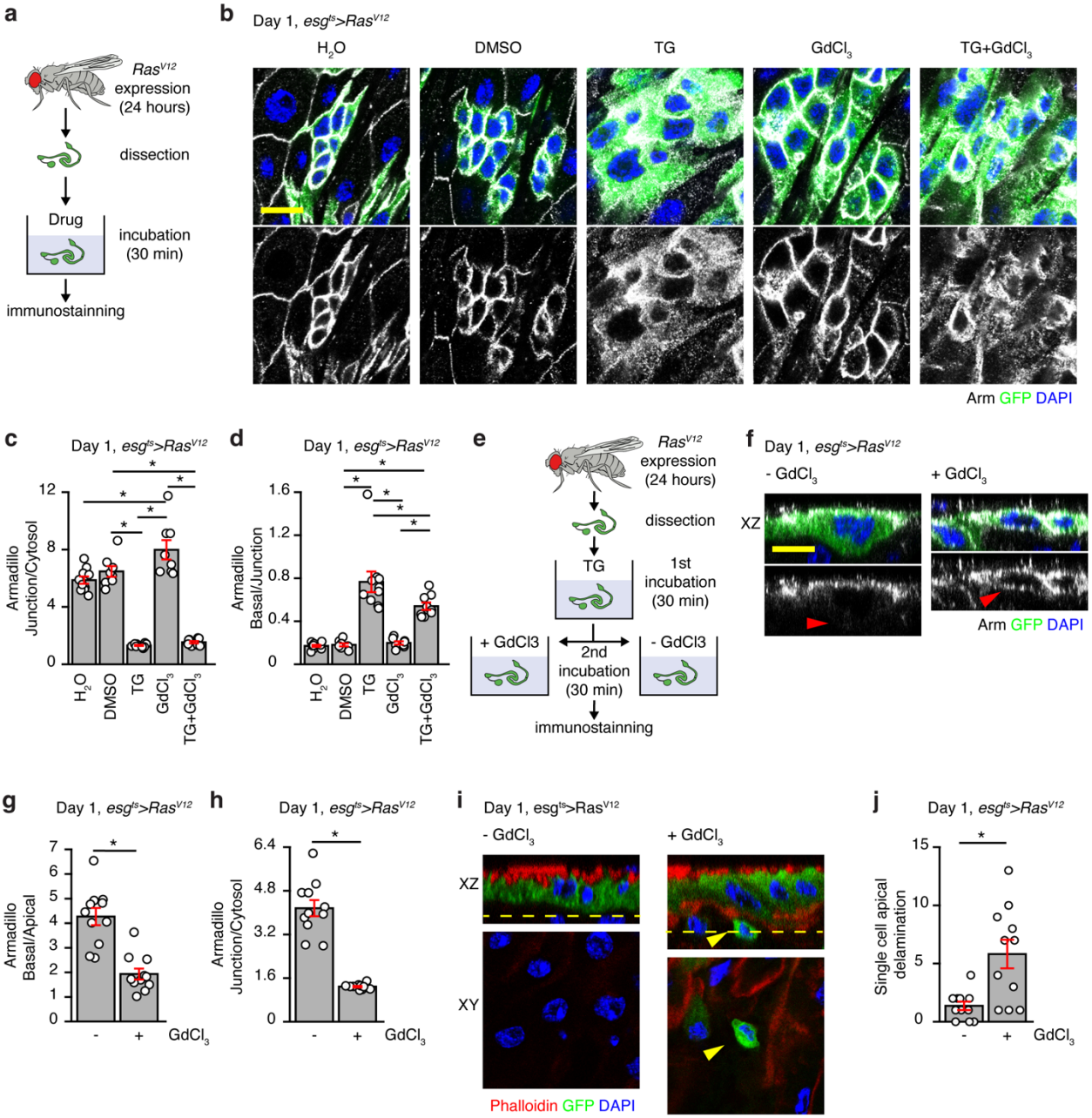
a
RasV12 expression (24 hours)
dissection
Drug
incubation (30 min)
immunostainning
b
Day 1, esgts>RasV12
H2O
DMSO
TG
GdCl3
TG+GdCl3
Arm GFP DAPI
c
Day 1, esgts>RasV12
Armadillo Junction/Cytosol
H2O
DMSO
TG
GdCl3
TG+GdCl3
d
Day 1, esgts>RasV12
Armadillo Basal/Junction
e
RasV12 expression (24 hours)
dissection
TG
1st incubation (30 min)
+ GdCl3
2nd incubation (30 min)
- GdCl3
immunostainning
f
Day 1, esgts>RasV12
- GdCl3
+ GdCl3
XZ
Arm GFP DAPI
g
Day 1, esgts>RasV12
Armadillo Basal/Apical
GdCl3
h
Day 1, esgts>RasV12
Armadillo Junction/Cytosol
GdCl3
i
Day 1, esgts>RasV12
- GdCl3
+ GdCl3
XZ
XY
Phalloidin GFP DAPI
j
Day 1, esgts>RasV12
Single cell apical delamination
GdCl3

Figure 12. Endoplasmic reticulum calcium release and extracellular calcium entry generate distinct signals regulating the localization of E-cadherin/β-catenin.

a, Schematic outlining the *ex vivo* midgut manipulation procedure. $esg^{ts}>Ras^{V12}$ midguts are dissected out at day 1 of Ras^{V12} expression for *ex vivo* treatments for 30 minutes and then stained with anti-Arm antibody. **b,** Midgut epithelia showing Arm signals (gray). Ras^{V12} cells are marked by GFP (green), and nuclei are stained with DAPI (blue). Scale bar, 10 μm. **c,** Ratios of junctional and cytosolic Arm signal intensities. The average fluorescent intensity of Arm at cell-cell junctions are normalized to that in the cytosol. P=1.7979x10^{-12} (DMSO - TG), P=0.0006 (H_2O - $GdCl_3$), P=1.0472x10^{-11} (DMSO - TG+$GdCl_3$),*P=4.6474x10^{-13} (TG - $GdCl_3$), P=4.6918x10^{-13} ($GdCl_3$ - TG+$GdCl_3$). **d,** Ratios of basal and junctional Arm signal intensities. Average Arm fluorescent intensity in basal membrane was normalized to that in the cell-cell junction. Measurements were acquired from orthogonal views. P=7.2906x10^{-09} (DMSO - TG), P=2.0376x10^{-04} (DMSO - TG+$GdCl_3$), P=1.5348x10^{-08} (TG - $GdCl_3$), P=0.0215 (TG - TG+$GdCl_3$), P=4.1858x10^{-04} ($GdCl_3$ - TG+$GdCl_3$). For **c** and **d**, each data point represents the mean value of the fluorescent intensities measured from 10 cells in a midgut – a biological replicate. From left to right, n=10 (H_2O), n=8 (DMSO), n=10 (TG), n=8 ($GdCl_3$), n=9 (TG+$GdCl_3$) biological replicates. Mean±SEMs are shown. Statistical analysis was performed using one-way ANOVA with post-hoc Tukey HSD. **e,** Schematic of the sequential drug treatment experiments. $esg^{ts}>Ras^{V12}$ midguts are dissected out at day 1 of Ras^{V12} expression for treating TG for 30 minutes. The TG-treated midguts are incubated with or without $GdCl_3$ for 30 minutes. **f,** Orthogonal views of representative Ras^{V12} cells treated with TG and

then incubated with (right panels) or without $GdCl_3$ (left panels). The basal side of cells is positioned upward, and arrowheads indicate the apical cell surface. Scale bar, 10 μm. **g,** Ratios of basal and apical Arm signal intensities. P=3.0136x10^{-05}. **h,** Ratios of junctional and cytosolic Arm signal intensities. P=1.9916x10^{-06}. For **g** and **h**, each data point represents the mean value of the fluorescent intensities measured from 10 cells in a midgut – a biological replicate. n=11(DMSO), n=11 ($GdCl_3$) biological replicates. Mean±SEMs are shown, and *P<0.05 (two-tailed unpaired Student's t-test).**i,** Orthogonal and cross sections of *esg^{ts}>Ras^{V12}* midguts. Phalloidin (red) stains Actin in the VM, and DAPI (blue) show nuclei. *Ras^{V12}* cells are marked with GFP (green). Top panels show orthogonal views (xz), and bottom panels show cross sections (xy) above the apical end of the epithelia. Arrowheads indicate a representative apically delaminating *Ras^{V12}* cell. Scale bar, 10 μm. **j,** Quantification of apical cell delamination. P=0.0049. n=11(DMSO), n=11 ($GdCl_3$) biological replicates. Mean±SEMs are shown. *P<0.05 (two-tailed unpaired Student's t-test).

Chapter 8. Discussion on the role of DE-cadherin in cell invasion and its regulation by the IP3R and Piezo

In this study, we describe the unexpected role of DE-cad in the invasiveness of Ras^{V12} cells during cell dissemination. Without DE-cad, Ras^{V12} cells could not invade or disseminate *in vivo*. DE-cad/Arm subcellular distribution remodels during dissemination of Ras^{V12} cells: DE-cad/Arm disassembles at adherens junctions and assembles at invasive protrusions, which are not the conventional locations to detect DE-cad/Arm. Mechanistically, DE-cad controls the function of invasive protrusions, not the formation. Thus, loss of DE-cad results in inability of Ras^{V12} cells to breach the ECM and the VM. Our findings coincide with the previous clinical reports describing metastasis of $E\text{-}cad^{+}$ cancers [71-74]. Padmanaban et al. (2019) have demonstrated that E-cad promotes metastasis in multiple models of breast cancer by functioning as a survival factor [63]. Our study provides new insight into the molecular mechanism by which E-cad can promote the initial step of metastasis.

Our study elucidates the essential roles of the two intracellular calcium signaling pathways in the invasiveness of Ras^{V12} cells (Fig. 13). The PLC-IP3R-CAMK pathway induces disassembly of DE-cad/Arm at adherens junctions, which recapitulates the functional consequence caused by E-cad loss during epithelial-mesenchymal transition (EMT) [51, 88, 89]. Importantly, the Piezo-calpain pathway controls assembly of DE-cad/Arm at invasive protrusions, which is critical for breaching the ECM and the VM. Interestingly, Piezo is required for assembly of DE-cad/Arm at not only invasive protrusions but also

the basal side and adherens junctions, suggesting that the general role of calcium entry via Piezo is to control localized assembly of DE-cad/Arm by sensing the mechanical cues in the microenvironment. We have previously reported that Piezo orchestrates dissemination of *Ras*^{V12} cells by controlling multiple cellular processes, including invasive protrusion's function, matrix metalloprotease 1 (MMP1) expression, and bleb-driven movement [75]. Additionally, Piezo channels have been shown to be important for matrix degradation in cultured cancer cells [43, 90]. A recent preprint suggests that E-cadherin plays a role in invadopodia formation in human cancer cells [91]. Thus, the regulation of E-cad assembly by Piezo channels might be a conserved mechanism by which tumor cells coordinate their invasive behavior upon sensing mechanical cues in the microenvironment. Recently, it has been shown that activation of E-cad by injecting an E-cad activating antibody inhibits metastasis in mice presumably by strengthening adherens junctions [64]. Our study provides a repertoire of potential targets for strengthening adherens junctions or inhibiting assembly of E-cad at invadopodia to halt the spreading of transformed cells.

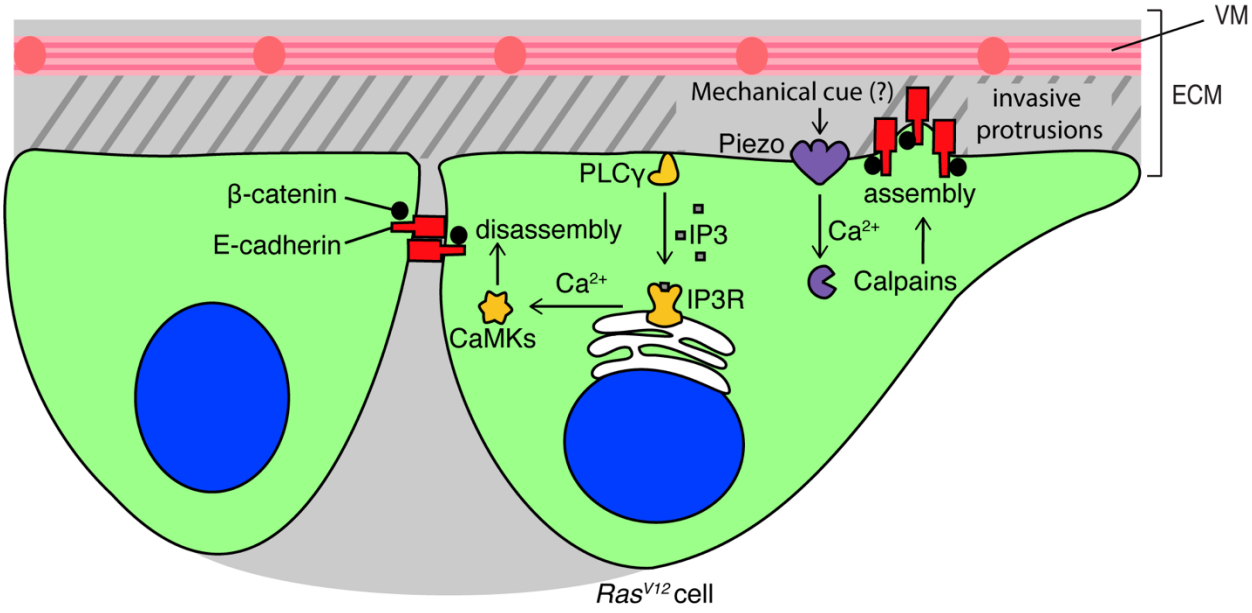
VM
ECM
Mechanical cue (?)
Piezo
invasive
protrusions
assembly
PLCγ
IP3
β-catenin
E-cadherin
disassembly
Ca2+
IP3R
CaMKs
Ca2+
Calpains
RasV12 cell

Figure 13. E-cadherin/β-catenin regulation by intracellular calcium signaling in *Ras^{V12}* cells

E-cadherin/β-catenin localizes to adherens junctions in control epithelial cells. During dissemination of *Ras^{V12}* cells, E-cadherin/β-catenin disassembles at adherens junctions and assembles at invasive protrusions. The disassembly of E-cadherin/β-catenin at adherens junctions is induced by intracellular calcium signaling caused by ER Ca^{2+} release via the PLC-IP3R pathway. The assembly of E-cadherin/β-catenin at invasive protrusions is induced by Ca^{2+} entry via Piezo. Given the role of Piezo in mechanosensation, Piezo-mediated assembly of E-cadherin/β-catenin may allow *Ras^{V12}* cells to adjust their invasive behavior by sensing mechanical cues in their microenvironment.

Chapter 9. Methods

9.1 *Drosophila* stocks and genetics

The stocks obtained from the Bloomington *Drosophila* Stock Center (BDSC), the Vienna *Drosophila* Resource Center (VDRC), and the National Institute of Genetics, Japan (NIG) are the following: *UAS-Piezo-GFP/TM6B* (#58773), *UAS-Ras^{V12}* (III) (BDSC, 4847), *UAS-Raf^{gof}* (#2033), *UAS-p35* (#5073), *UAS-Cortactin-HA* (#9368), *ey-GAL4* (#5534), and *UAS-EGFP* (#5430), *UAS-DE-cad-i^{JF02769}* (BDSC, 27689), *UAS-DE-cad-i^{HMS0693}* (BDSC, 32904), *UAS-DE-cad* (BDSC, 655589), *UAS-DE-cad-GFP* (BDSC, 58445), *shg^{mTomato}* (referred as *DE-cad^{mTomato}*; BDSC, 58789), *UAS-sl-i^{HMS00377}* (BDSC, 32385), *UAS-sl-i^{HMS00695}* (BDSC, 32906), *UAS-IP3R-i^{JF01957}* (BDSC, 25937), *UAS-IP3R-i^{GD1676}* (VDRC, 6484), *UAS-IP3R-i^{HMC03351}* (BDSC, 51795), *UAS-CaMKII-i* (BDSC, 29401), *UAS-CaMKI-i* (BDSC, 26726), *UAS-Piezo-i$^{8486R-3}$* (NIG, 8486R-3), *UAS-Piezo-iv2796* (VDRC, 2796), *UAS-CalpA-i$^{7563R-3}$* (NIG, 7563R-3), *UAS-CalpA-i^{JF03391}* (BDRC, 29455), *UAS-Calpain-B* RNAi (BDSC, 25963), *UAS-Cortactin* RNAi (BDSC, 32871), *UAS-Actin-mRFP* (BDSC, 24778), and *UAS-Lifeact-mRFP* (BDSC, 58362). We also used *UAS-Ras^{V12}* (II) (laboratory stock) and *UAS-mCherry-Moe.ABD* (FlyBase, FBtp0108918; gift from Dr. Susan Parkhurst). For the experiments to check subcellular distribution of Piezo-GFP and Cortactin-HA, we omitted *UAS-GFP* from *esg^{ts}*.

Knockdown efficiency of the *Piezo* RNAi lines was assessed by expressing each line with a *Piezo* promoter trap line, *Piezo-GAL4* (BDSC #78335) [40]. We extracted RNA samples from 5 adult female flies to measure *Piezo* mRNA levels by qPCR using the

primer sequences: 5'-TTGCTCGTTCAGTGAGCGTC-3' and 5'-AGGCACTAGCCATTCGATGAT-3'. *Piezo* transcript levels were reduced to ~43% by *UAS-Piezo-i*^{8486} and ~61% by *UAS-Piezo-i*^{v2796} compared to the levels in *Piezo-GAL4* only.

9.2 Fly husbandry

To manipulate intestinal stem cells (ISCs) and enteroblasts (EBs), we used *esg-GAL4, tub-GAL80*^{ts}, *UAS-GFP* (referred as *esg*^{ts}) (laboratory stock). The experimental procedures are described previously [92]. Fly crosses were raised in vials containing standard cornmeal-agar medium and incubated at 18°C throughout development and adulthood. 3- to 10-day old non-virgin female flies were used for all experiments. Flies were shifted to 29°C for 1- to 6-days prior to dissection. During incubation at 29°C, flies were transferred onto fresh food every 2 days.

9.3 Antibodies and immunostaining

We used the following primary antibodies: rabbit anti-GFP antibody, Alexa Fluor® 488 (1:1000; Thermo Fisher Scientific, A-21311), mouse anti-Dl antibody (1:1000; Developmental Studies Hybridoma Bank, C594.9B), rabbit anti-phospho-histone H3 antibody (1:1000; Millipore, 06-570), mouse anti-phospho-histone H3 antibody (1:1000; Abcam, ab14955, mouse anti-HA antibody (1:2000; Santa Cruz, SC7392), mouse anti-Armadillo (1:100; DSHB, N27A1), rat anti-DE-cadherin antibody concentrate (1:50; DSHB, DCAD2), rabbit anti-Laminin B1 (1:100; Abcam, ab47650), mouse anti-Mmp1 (1:1000; DSHB, 3B8D12). Alexa Fluor secondary antibodies raised in goat (A11012,

A11005, A21244, A21235) were obtained from Thermo Fisher Scientific and used at a dilution of 1:1000. We stained F-actin with phalloidin conjugated to Alexa 594 or 647 (1:1000, Thermo Fisher Scientific, A12381 and A22287). DAPI was used at a 1:2000 dilution (Sigma-Aldrich, D9542).

We fed flies 4% sucrose for approximately 4 hours prior to dissection to remove food from the midgut. Midguts from the adult female flies were then dissected in phosphate buffered saline, pH7.4 (PBS) and fixed for 20 minutes at room temperature in 4% paraformaldehyde (PFA) (Electron Microscopy Sciences, RT15710) diluted in PBS. Midguts were washed three times in PBST (PBS supplemented with 0.2% Triton X-100) and then blocked overnight in PBST supplemented with 5% normal goat serum at 4°C. The tissue samples were then incubated with primary antibody in PBST supplemented with 5% normal goat serum for 2-3 hours at room temperature and rinsed three times in PBST. Secondary antibodies and DAPI were diluted together in PBST supplemented with 5% normal goat serum and incubated with samples at room temperature for 1-2 hours. After secondary incubation, the samples were rinsed three times in PBST and mounted in Vectashield (Vector Laboratories, H1000).

9.4 Immunofluorescence imaging

Fluorescence micrographs were acquired with a Leica SP8 laser scanning confocal microscope with 20x/0.7 dry, 40x/1.25 oil, or 63X/1.4 objective lenses. Higher resolution images were acquired using Leica LIGHTNING—a detection package for image information extraction of confocal images. 3D reconstructions were created from

z-stack images using a LAS X 3D viewer. NIH ImageJ software was used for further adjustment and assembly of the acquired images.

9.5 Quantification of disseminated cells

We defined disseminated cells as GFP- and DAPI- positive cells residing more basally than the visceral muscle layer, which was labeled with Phalloidin. To determine the position of a cell, we captured a series of z-stacks using confocal microscopy. Orthogonal view reconstituted from z-stacks was used for further confirmation. The number of disseminated cells was counted from the R5 region of the posterior midgut captured in 388 μm x 388 μm confocal microscope fields. Confocal stacks 0.8 μm step size. Graphical representations of all data points were generated as bar charts with data point overlap in R.

9.6 Quantification of longitudinal muscle breakage

To quantify longitudinal muscle breakage, we visualized the visceral muscles by staining with phalloidin. Longitudinal muscle breaks were quantified from one leaflet of the confocal stacks (0.8 µm step size). Fluorescent images (388 μm x 388 μm) were acquired from the posterior midgut with 40X/1.25 oil objective. Graphical representations of all data points were generated as ggplot2 dot plots in R.

9.7 Quantification of Mmp1 intensity

Laser settings were kept identical for capturing midgut images. Confocal planes covering one leaflet of the midgut along the apical-basal axis were projected to generate

the 388 μm x 388 μm microscope field projection. We collected mean intensity values from three random 100 μm x 100 μm fields per midgut using Fiji and subtracted background values from the area outside surrounding the intestine. Graphical representations of all data points were generated as bar charts with data point overlap in R.

9.8 Quantification of Laminin B1 intensity

To measure fluorescent intensity of Laminin B1, we generated z-projection (388 μm x 388 μm) of confocal stacks covering one leaflet of the posterior midgut. Mean gray values from three random 100 μm x 100 μm regions per midgut were collected. The background was then subtracted using values from the area outside the intestine. Graphical representations of all data points were generated as bar charts with data point overlap in R.

9.9 Quantification of phosphor-histone H3 (pHH3)-positive cells

To determine the number of dividing cells, midguts were dissected and stained with DAPI and anti-pHH3 antibody. pHH3-positive nuclei were counted from the entire midgut.

9.10 Intestinal tumor quantification

We defined tumors as epithelial layers having over 80% of the layer comprising of GFP-positive cells. Images were acquired from the R5 region of the posterior midgut with

the 40x/1.25 oil objective covering 388 μm x 388 μm in area. Graphical representations of all data points were generated in the percentage stacked bar chart in R.

9.11 Actin time-lapse imaging

To monitor filamentous Actin during *ex vivo* live imaging, we expressed Lifeact-mRFP with *esg*^{ts}. 5–7 days old adult flies were incubated at 29°C for 2 days before imaging. Time-lapse imaging of the posterior midgut was captured with a Leica SP8 laser scanning confocal microscope using a 40x/1.25 oil objective. Z-stacks of the dual-color images were recorded every 1 minute for 2 hours. A maximum intensity z-projection was obtained using Leica LAS X imaging software.

9.12 *Ex vivo* live imaging

The experimental procedures described in [93] were adapted for *ex vivo* live imaging of midguts. Our *ex vivo* live-imaging medium comprises Schneider's *Drosophila* medium (Thermo Fisher Scientific, 21720024), 2% FBS (Life Technologies, 16140071), and 0.5% penicillin-streptomycin (Thermo Fisher Scientific, 15140122).

Drosophila were dissected in the imaging media and the entire midgut and hindgut sections were recovered. Then, the dissected samples were mounted on a 35mm glass bottom dish (MatTek, P35G-1.0-14-C). To prevent squeezing, vacuum grease was applied as two lines on the glass bottom dish, approximately 2mm apart. ~100 μl of imaging media was added to the center of the dish, and the dissected guts were placed perpendicular to the vacuum grease lines. Anterior end of the midgut and hindgut

segment were embedded in each vacuum grease line to prevent drifting. A cover glass was gently placed on top of the vacuum grease lines to prevent excessive movement of the midgut. Approximately 1ml of imaging medium was added to the dish to prevent dehydration and facilitate gas exchange. To prevent media evaporation the samples were covered with the dish lid and were imaged from the bottom side.

9.13 Quantification of vesicles released from gut

Ex vivo live imaging of midguts was processed into z-projection videos with the Leica LAS X software. The number and diameter of the GFP-positive vesicles detected outside the midguts at the indicated time points were quantified using NIH ImageJ software.

9.14 Collection of circulating ELEVs and disseminated cells

Hemolymph was collected through punctures on the head as described [94]. Hemolymph prepared from 3 flies was mixed with 3µl of Vectashield with DAPI (1:2000) for immediate imaging. 7 random views of 500 μm x 500 μm confocal microscope fields were obtained with a Leica SP8 laser scanning confocal microscope with 40x/1.25 oil objective. ELEVs larger than 1 μm were counted using the NIH ImageJ analysis particle function. The number of circulating cells was counted manually by finding foci that were positive for both GFP and DAPI.

9.15 Gd^{3+} feeding

3–7 days old adult flies were transferred onto standard media supplemented with either solvent (distilled water) or 100 μM $GdCl_3$ (EMD Millipore, G7532-5G), then allowed to feed while the transgenes were induced at 29°C.

9.16 Cell outline tracing

We picked cells with distinguishable boundary and followed them for one hour in *ex vivo* live imaging z-projection videos. Still shots were captured every 10 minutes. At each timepoint, cell outline was traced using freehand area selection tool and subjected to create mask in NIH ImageJ software. To visualize the changes in cell boundary overtime, the traced cell outlines were overlaid. To quantify the changes in cell boundary, we measured non-overlapping area of two cell silhouettes acquired at consecutive time points (n' and n+10', n = 0', 10', 20', 30', 40', 50'), apostrophe indicates minutes.

9.17 *Ex vivo* drug treatment and quantification

For the *ex vivo* experiments, we essentially used *Drosophila* Adult Hemolymph-like saline (AHLS) comprising 2 mM $CaCl_2$, 5 mM KCl, 5 mM HEPES, 8.2 mM $MgCl_2$,108 mM NaCl, 4 mM $NaHCO_3$, 1 mM NaH_2PO_4, 10 mM Sucrose, and 5 mM Trehalose [95]. The solution was adjusted to pH 7.5 and stored at 4C. We dissolved Thapsigargin (TG) (Sigma-Aldrich, T9033) in DMSO and $GdCl_3$ (EMD Millipore, G75325G) in water to make stock solutions.

Ras^{V12} was expressed with *esg*^{ts} for 24 hours and dissected in AHLS to prepare the whole midguts. The dissected midguts were then incubated in AHLS supplemented with 4% Fetal Bovine Serum (Life Technologies, 16140071) for drug treatment for 30 minutes at room temperature in unsealed glass dissection wells. Intestines were then washed in PBS, fixed in 4% PFA, and immunostained. Fluorescent images (388 μm x 388 μm) were captured from the posterior midguts. Laser settings were kept identical for all conditions. For sequential treatment experiments, dissected midguts were incubated with 1 µM TG for 30 minutes and then washed three times in AHLS with 4% FBS. The TG-treated midguts were then incubated in AHLS with 4% FBS containing either 100 µM $GdCl_3$ or solvent for 30 minutes. Midguts were washed in PBS and followed by immunostaining. All steps occurred in unsealed wells at room temperature.

To assess junction integrity, we measured Armadillo (Arm) signal intensity from 10 cells per midgut. Arm signal intensity was measured from a representative cross-section for a given cell using the plot profile feature in FIJI. We measured Arm signal intently along a line drawn from the cell boundary to the nuclear boundary. We took the measured value at the midpoint of the line as the cytosolic Arm signal intensity and compared to the value obtained at the cell boundary/junction. For statistical analysis, one-way ANOVA with post-hoc Tukey HSD (Honestly Significant Difference) was performed using R.

To assess the enrichment of Arm at the basal surface relative to junction, we used a representative orthogonal view of a given cell. We measured Arm signal intensity at the basal boundary and compared to Arm signal intensity measured at the lateral boundary of the cell. The ratios of Basal and Junctional signal intensities were presented, and one-

way ANOVA with post-hoc Tukey HSD (Honestly Significant Difference) was performed using R.

To assess the Arm signal ratio between basal and apical surfaces, Arm signals were quantified from ten cells per midgut. We measured signal intensity values from a representative orthogonal view of given cell by tracing cell's basal and apical boundaries. The ratios of basal and apical Arm signals were calculated, and two-tailed unpaired t-test was performed for statistical analysis.

To quantify apically delaminating cells, we used the orthogonal view in FIJI to determine the midgut epithelial boundary-outlined with phalloidin staining. GFP^+, $DAPI^+$ cells detected outside the midgut epithelial boundary were counted. For statistical analyses, two-tailed unpaired t-tests were performed.

9.18 Statistics and reproducibility

All the images presented and used for quantification are from the posterior R5 region of adult female fly midguts, except for the pHH3, which is counted from the entire midgut. Statistical differences between groups of data were analyzed using a series of two-tailed unpaired Student t-test with unequal variances or one-way ANOVA with post-hoc Tukey HSD (Honestly Significant Difference). All statistical analyses and data graphics were done using Microsoft Excel, GraphPad Prism 8, and 'R' software (version 1.3.1093). All quantified experiments represent at least three biologically independent samples. Level of significance are depicted by asterisks in the figures: $*P<0.05$. *P* values

are indicated in the figure legends or graph. Sample sizes were chosen empirically based on the observed effects and listed in the figure legends.

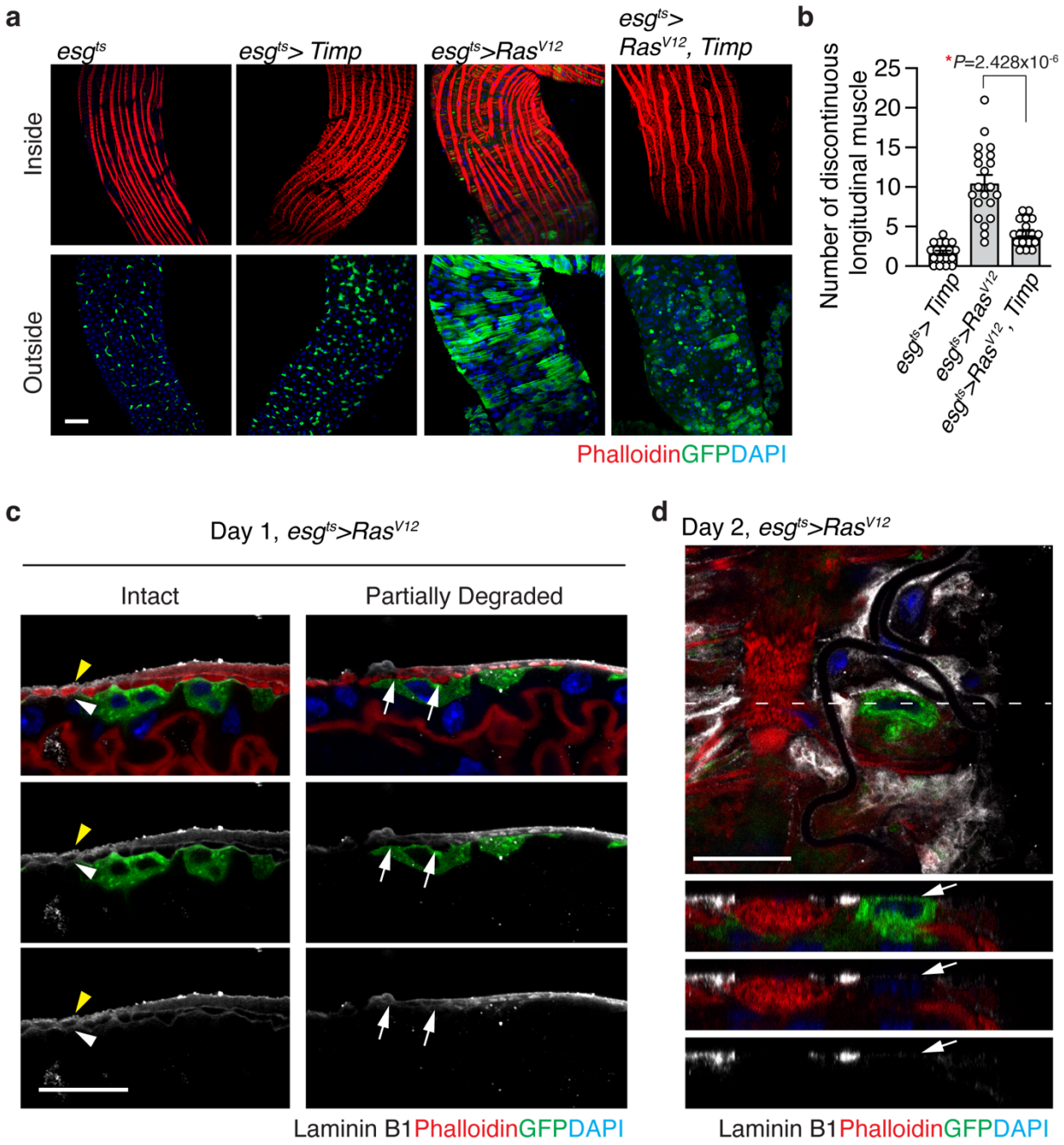
a
esg^ts
esg^ts> Timp
esg^ts>Ras^V12
esg^ts> Ras^V12, Timp
Inside
Outside
PhalloidinGFPDAPI
b
Number of discontinuous longitudinal muscle
*P=2.428x10^-6
25
20
15
10
5
0
esg^ts> Timp
esg^ts>Ras^V12
esg^ts>Ras^V12, Timp
c
Day 1, esg^ts>Ras^V12
Intact
Partially Degraded
Laminin B1PhalloidinGFPDAPI
d
Day 2, esg^ts>Ras^V12
Laminin B1PhalloidinGFPDAPI

Supplementary Figure 1. Inhibition of Mmp suppresses dissemination of *Ras^{V12}* cells.

a, Representative images of the posterior midgut at day 2 of transgene expression. Scale bar, 50 μm. **b,** Quantification of longitudinal muscle break. N=18 (*esg^{ts}>Timp*), N=21(*esg^{ts}>Ras^{V12}*), N=18 (*esg^{ts}>Ras^{V12}*, *Timp*) biological replicates. *Ras^{V12}* quantification is adopted from Fig. 3g. **c**, Laminin B1 staining from side view on day 1 *esg^{ts}>Ras^{V12}* midguts. White arrowhead points to the inner ECM layer adjacent to the epithelium, and yellow arrowhead points to the layer outside of the VM. Degradation of the inner ECM layer is pointed with white arrows. Scale bar, 20 μm. **d**, Laminin B1 staining from top view on day 2 *esg^{ts}>Ras^{V12}* midguts. Arrow points to the basal side of a *Ras^{V12}* cell, indicating that the cell was not imbounded by a Laminin layer. Scale bar, 20 μm. In the side views, the basal side of epithelium is positioned upward. In **b**, mean±SEMs are shown with individual data points. Data were analyzed by two-tailed unpaired Student's *t*-test. Asterisk indicates statistical significance (*P<0.01), and P-value is indicated in graph.

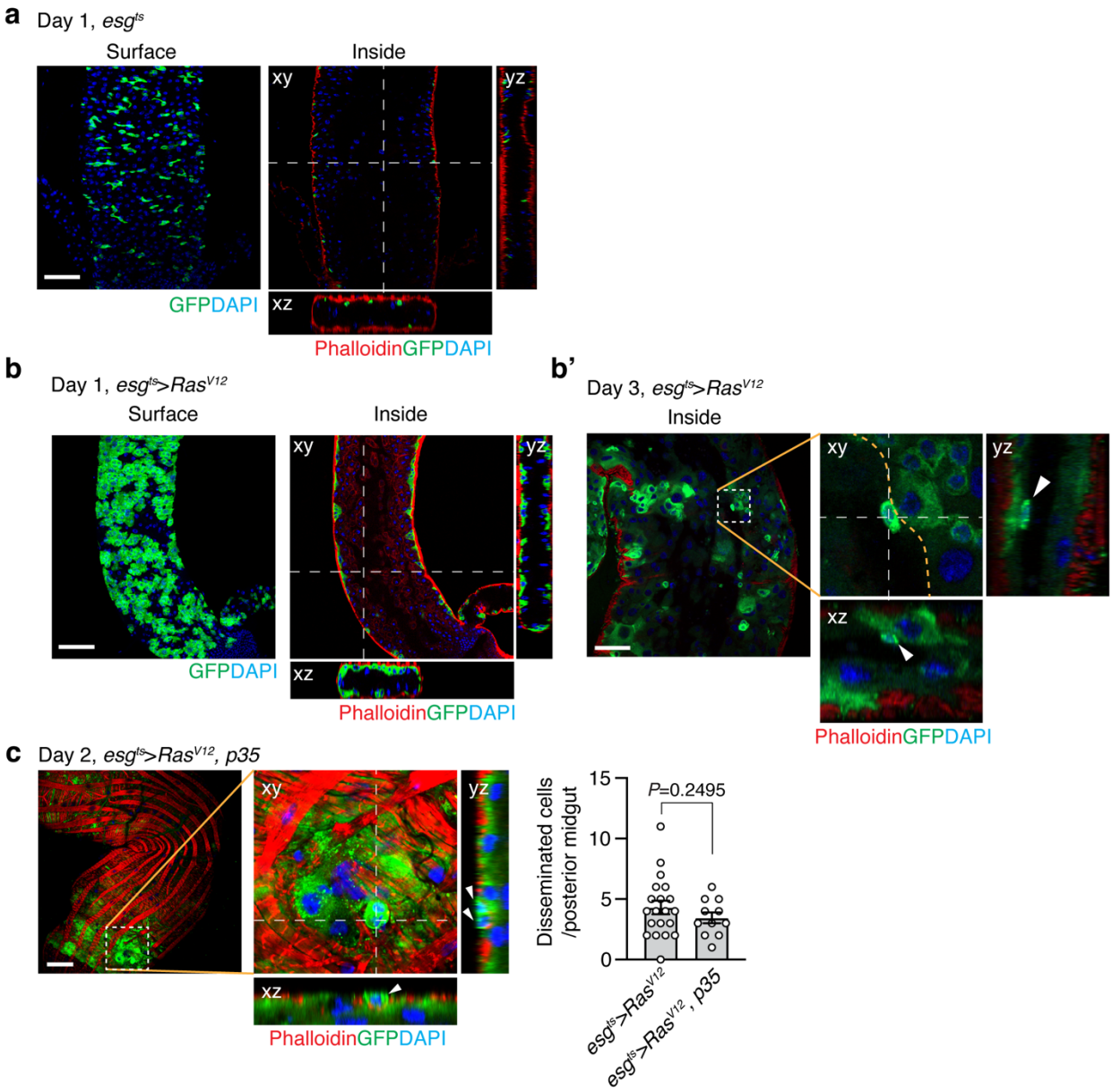
a
Day 1, esg^ts
Surface
Inside
xy
yz
xz
GFPDAPI
PhalloidinGFPDAPI
b
Day 1, esg^ts>Ras^V12
Surface
Inside
xy
yz
xz
GFPDAPI
PhalloidinGFPDAPI
b'
Day 3, esg^ts>Ras^V12
Inside
xy
yz
xz
PhalloidinGFPDAPI
c
Day 2, esg^ts>Ras^V12, p35
xy
yz
xz
PhalloidinGFPDAPI
Disseminated cells /posterior midgut
15
10
5
0
P=0.2495
esg^ts>Ras^V12
esg^ts>Ras^V12, p35

Supplementary Figure 2. Expression of *Ras^{V12}* also induces delamination into lumen.

a–b, Representative images of the posterior midguts at day 1 of transgene expression. At day 1, *Ras^{V12}* cells detached from the VM layer were rarely detected. **b'**, Representative image of the posterior *esg^{ts}>Ras^{V12}* midgut at day 3 of *Ras^{V12}* expression. *Ras^{V12}* cells delaminating into lumen were frequently detected at day 2 and 3 of *Ras^{V12}* expression. Inset shows *Ras^{V12}* cells detached from the VM layer and a *Ras^{V12}* cell (arrowhead) that appears to be shedding into lumen. Yellow dotted line indicates the apical boundary of the midgut epithelium. VM is visualized with Phalloidin (red), and nuclei are stained with DAPI (blue). Scale bars, 50 μm. **c**, Representative image of the posterior *esg^{ts}>Ras^{V12}*, *p35* midgut. Baculovirus p35 protein functions to prevent apoptotic death of infected cells. We have expressed p35 in *Ras^{V12}* cells with *esg^{ts}* for 2 days. Inset and the magnified views show basally disseminated cells (indicated with arrowheads). Scale bar, 50 μm. Graph on right shows quantification of disseminated cells detected on the surface of the posterior midgut. N=20 (*esg^{ts}>Ras^{V12}*), N=11(*esg^{ts}>Ras^{V12}*, *p35*) biological replicates. Mean±SEMs are shown with individual data points. Data were analyzed by two-tailed unpaired Student's *t*-test. *P*-value is indicated in graph.

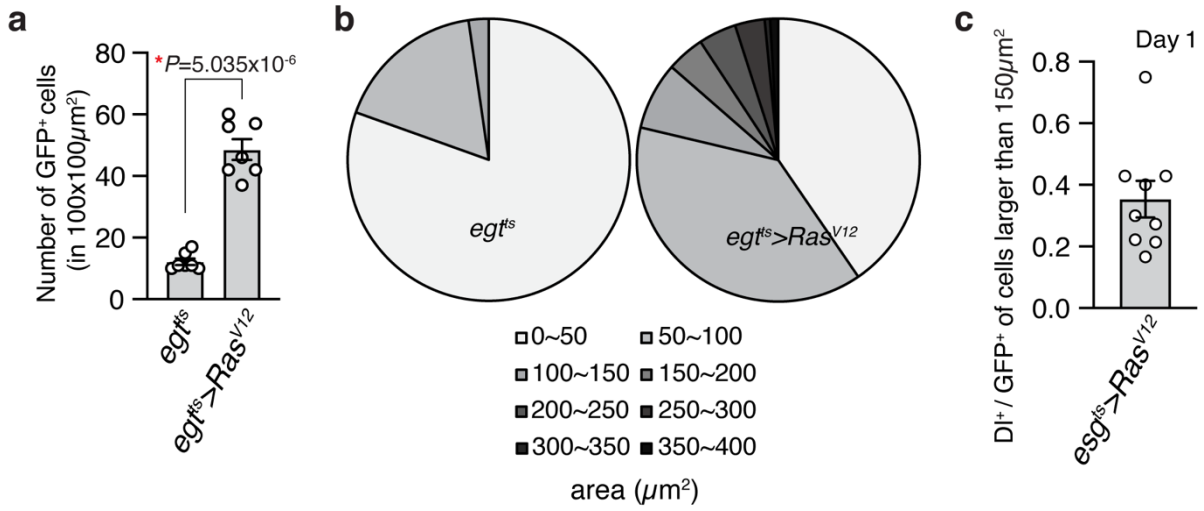
a
Number of GFP+ cells (in 100x100μm2)
80
60
40
20
0
*P=5.035x10-6
egtts
egtts>RasV12
b
egtts
egtts>RasV12
0~50
50~100
100~150
150~200
200~250
250~300
300~350
350~400
area (μm2)
c
Day 1
DI+ / GFP+ of cells larger than 150μm2
0.8
0.6
0.4
0.2
0.0
esgts>RasV12

Supplementary Figure 3. *Ras^{V12}* cells undergo proliferation and enlargement.

a, Quantification of ISC and EB cells in the *esg^{ts}>Ras^{V12}* midgut at day 1 of transgene expression. Number of GFP$^+$ cells were counted in 100x100 μm^2 of the posterior midgut. N=11 biological replicates for each genotype. **b**, Quantification of the size of GFP$^+$ cells at day 1. N=11 biological replicates for each genotype. **c,** Quantification of the proportion of Dl$^+$ cells in *esg^{ts}>Ras^{V12}* midgut that are larger than normal *esg^{ts}* cells. *Ras^{V12}*-expressing cells that are both Dl$^+$ positive and larger than 150 μm^2 were counted and divided by the number of total GFP$^+$ positive cells. N=9 biological replicates. In **a**, mean±SEMs are shown with individual data points. Data were analyzed by two-tailed unpaired Student's *t*-test. Asterisk indicates statistical significance (*P<0.01), and P-value is indicated in graph.

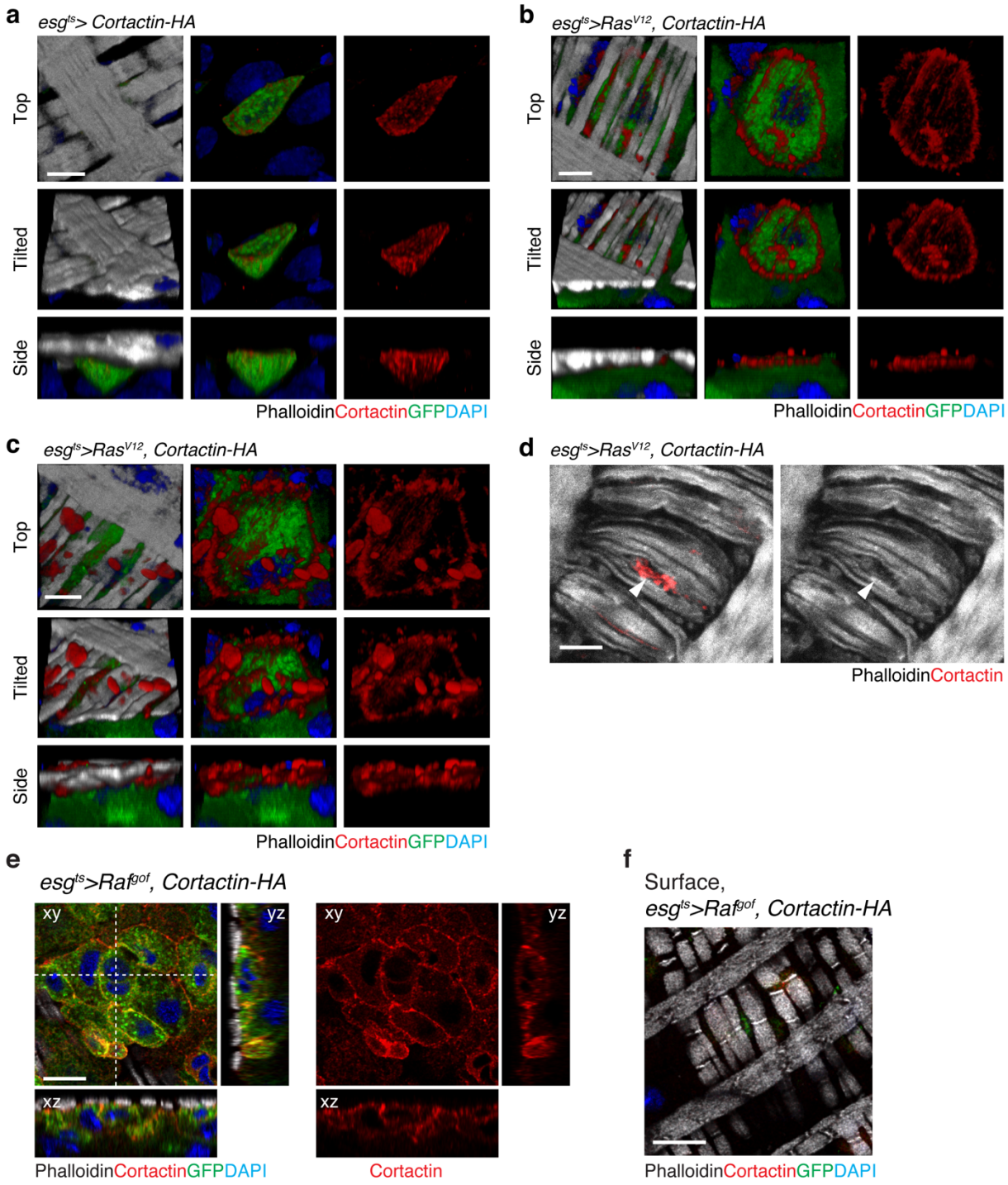
a
esg^ts> Cortactin-HA
Top
Tilted
Side
PhalloidinCortactinGFPDAPI
b
esg^ts>Ras^V12, Cortactin-HA
Top
Tilted
Side
PhalloidinCortactinGFPDAPI
c
esg^ts>Ras^V12, Cortactin-HA
Top
Tilted
Side
PhalloidinCortactinGFPDAPI
d
esg^ts>Ras^V12, Cortactin-HA
PhalloidinCortactin
e
esg^ts>Raf^gof, Cortactin-HA
xy
yz
xz
PhalloidinCortactinGFPDAPI
xy
yz
xz
Cortactin
f
Surface,
esg^ts>Raf^gof, Cortactin-HA
PhalloidinCortactinGFPDAPI

Supplementary Figure 4. Basal Cortactin-rich protrusions disrupt visceral muscle integrity.

a-c, 3D reconstructions of confocal images angled at 0, 45, and 90 degrees. Representative images of *esg^{ts}* cells (**a**) and *esg^{ts}>Ras^{V12}* cells (**b, c**) are shown. Dissected guts were stained with anti-HA antibody for Cortactin (red), Phalloidin (gray) for Actin, and DAPI (blue) for nuclei. Scale bars, 5 μm. N=8 (*esg^{ts} >Cortactin-HA*) for **a** and N=20 (*esg^{ts}>Ras^{V12}*, *Cortactin-HA*) biological replicates for **b, c** and **d**. **d,** Surface view of a rupture in the VM layer associated with a cluster (arrowhead) of Cortactin-rich protrusions (red). Scale bar, 5 μm. **e-f**, Top and orthogonal views (**e**) and surface view (**f**) of *esg^{ts}>Raf^{gof}, Cortactin-HA* cells at day 4 of transgene expression. Note that the basal Cortactin-rich protrusions were not formed by overexpression of Cortactin-HA in *esg^{ts}>Raf^{gof}* cells. Scale bars, 10 μm. In the side views, the basal side of epithelium is positioned upward.

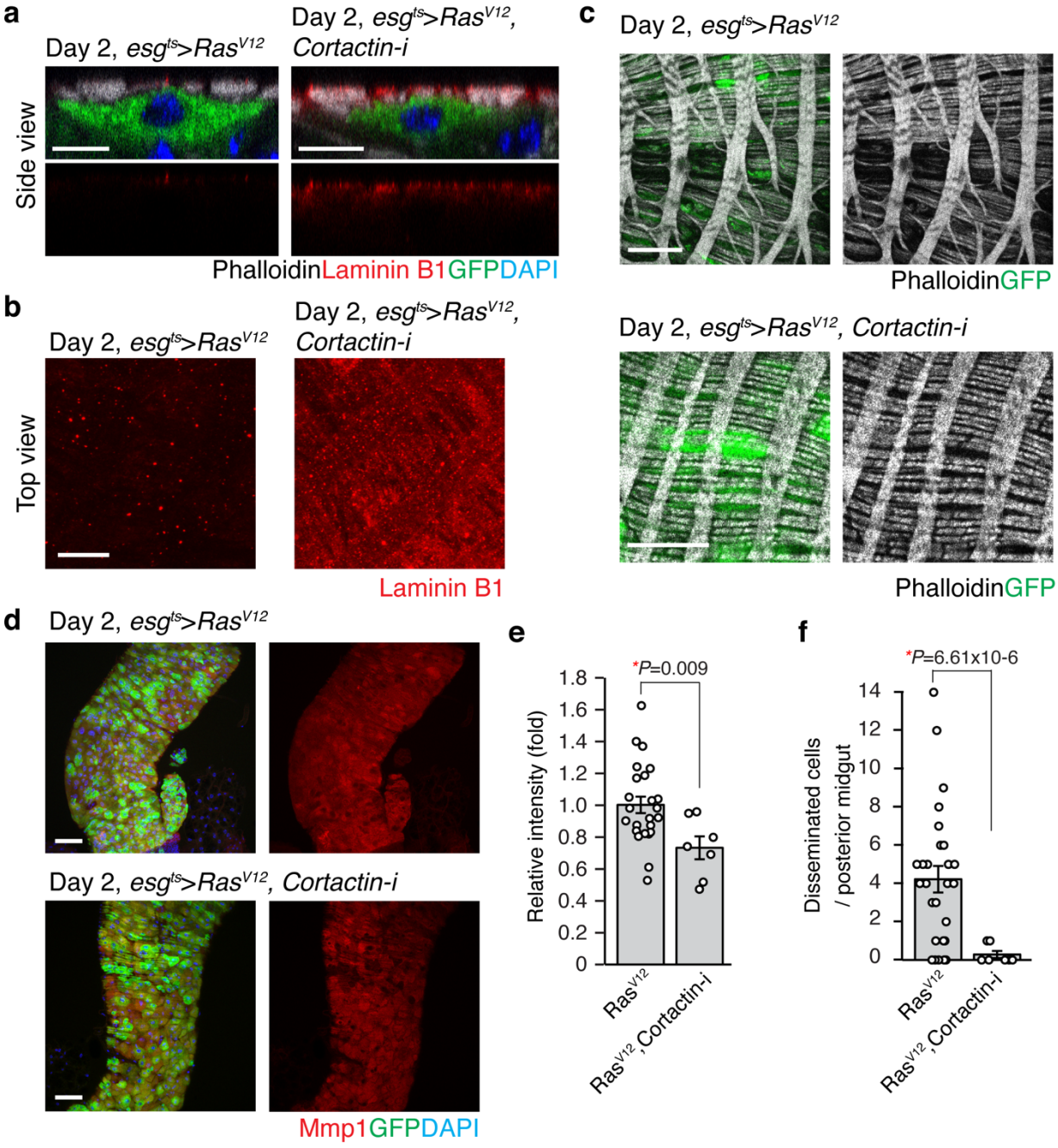
a
Day 2, esg^ts>Ras^V12
Day 2, esg^ts>Ras^V12, Cortactin-i
Side view
PhalloidinLaminin B1GFPDAPI
b
Day 2, esg^ts>Ras^V12
Day 2, esg^ts>Ras^V12, Cortactin-i
Top view
Laminin B1
c
Day 2, esg^ts>Ras^V12
PhalloidinGFP
Day 2, esg^ts>Ras^V12, Cortactin-i
PhalloidinGFP
d
Day 2, esg^ts>Ras^V12
Day 2, esg^ts>Ras^V12, Cortactin-i
Mmp1GFPDAPI
e
*P=0.009
Relative intensity (fold)
1.8
1.6
1.4
1.2
1.0
0.8
0.6
0.4
0.2
0
Ras^V12
Ras^V12,Cortactin-i
f
*P=6.61x10-6
Disseminated cells / posterior midgut
14
12
10
8
6
4
2
0
Ras^V12
Ras^V12,Cortactin-i

Supplementary Figure 5. *Cortactin* knockdown in *Ras^{V12}* cells suppresses Laminin degradation, Mmp1 expression, and cell dissemination.

a, Side view showing Laminin B1 expression. *esg^{ts}>Ras^{V12}* and *esg^{ts}>Ras^{V12}*, *Cortactin-i* midguts were stained with anti-Laminin B1 antibody (red), Phalloidin (gray), and DAPI (blue). Scale bars, 10 μm. **b,** Top view showing Laminin B1(red) expression. Scale bar, 10 μm. **c,** Visceral muscle (gray) integrity on day 2 of transgene expression. Scale bars, 30 μm. **d,** Mmp1 immunostaining (red) of posterior midguts. Scale bars, 50 μm. **e,** Quantification of Mmp1 levels per midgut: N=24 (*esg^{ts}>Ras^{V12}*), N=7 (*esg^{ts}>Ras^{V12}, Cortactin-i*) biological replicates. 3 regions were measured from each sample. **f,** Quantification of disseminated cells at day 2 of transgene expression: N=27 (*esg^{ts}>Ras^{V12}*), N=7 (*esg^{ts}>Ras^{V12}*, *Cortactin-i*) biological replicates. In **e** and **f**, mean±SEMs are shown with individual data points. Data were analyzed by two-tailed unpaired Student's *t*-test. Asterisks indicate statistical significance (*P<0.01), and P-values are indicated in graph.

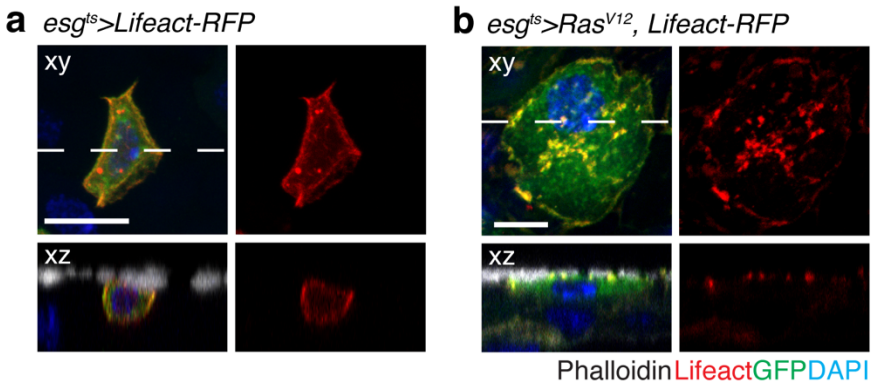
a esg^ts>Lifeact-RFP
xy
xz
b esg^ts>Ras^V12, Lifeact-RFP
xy
xz
PhalloidinLifeactGFPDAPI

Supplementary Figure 6. F-actin-rich puncta are formed at the basal side of *Ras^{V12}* cells.

a, Lifeact (red) distribution in an *esg^{ts}* control cell. Scale bar, 10 μm. **b**, Lifeact-rich puncta are formed at the basal side of an *esg^{ts}>Ras^{V12}* cell adjacent to the VM layer (Phalloidin, gray). Cells at day 2 of transgene expression are shown. Representative images are shown from N=11 (**a**) and N=16 (**b**) biological replicates. Scale bar, 10 μm.

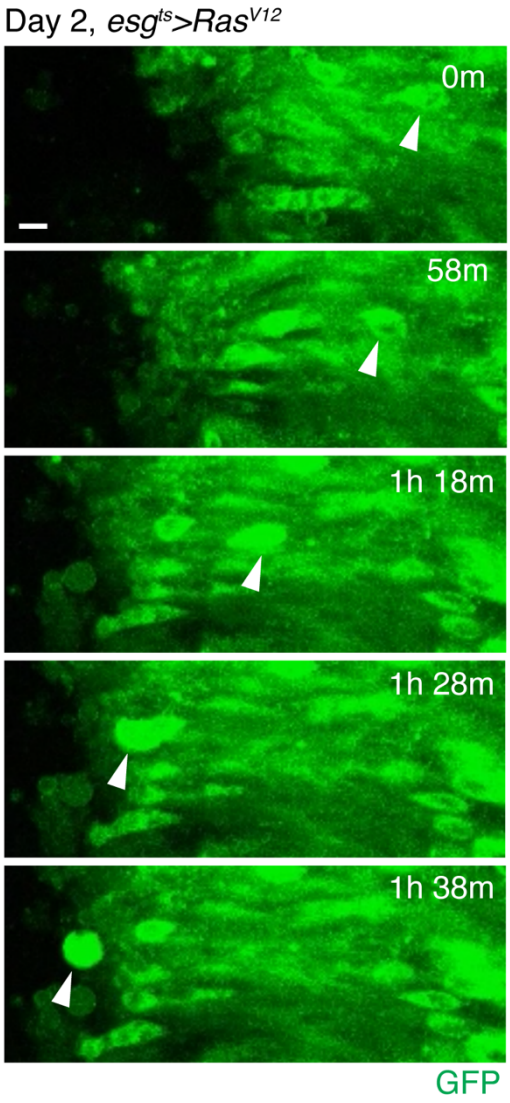
Day 2, esg^ts>Ras^V12
0m
58m
1h 18m
1h 28m
1h 38m
GFP

Supplementary Figure 7. Disseminating *Ras^{V12}* cell in a slipping motion.

Still shots from *ex vivo* live imaging of day 2 *esg^{ts}>Ras^{V12}* midgut (Supplementary Video 8). Arrowheads point to the disseminating cell at indicated time points. Scale bar, 10 μm.

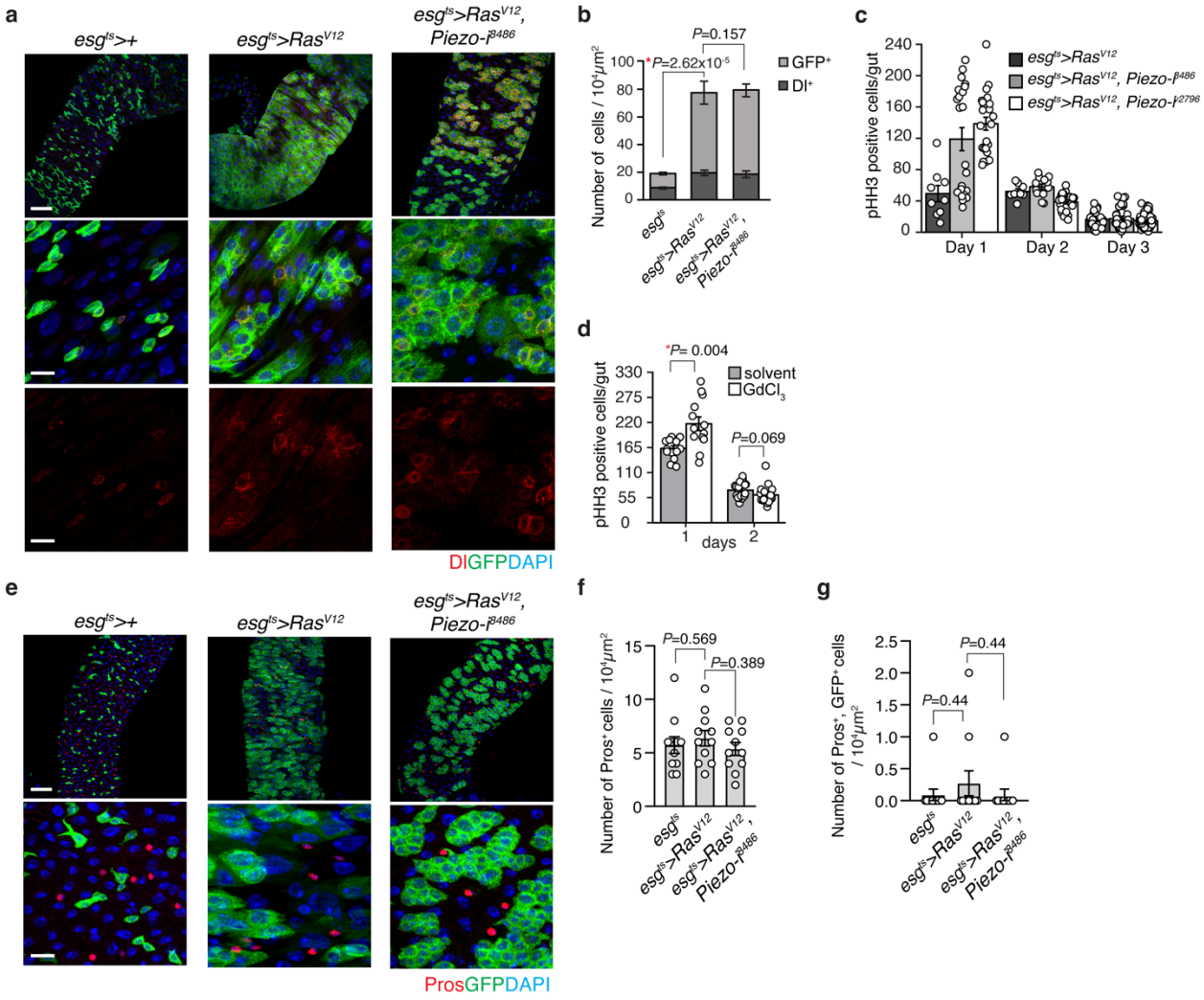
a
esg^ts>+
esg^ts>Ras^V12
esg^ts>Ras^V12, Piezo-i^B486
DlGFPDAPI
b
P=0.157
*P=2.62x10^-5
GFP+
Dl+
Number of cells / 10^4μm^2
esg^ts
esg^ts>Ras^V12
esg^ts>Ras^V12, Piezo-i^B486
c
esg^ts>Ras^V12
esg^ts>Ras^V12, Piezo-i^B486
esg^ts>Ras^V12, Piezo-i^2796
pHH3 positive cells/gut
Day 1
Day 2
Day 3
d
*P= 0.004
P=0.069
solvent
GdCl3
pHH3 positive cells/gut
1
days
2
e
esg^ts>+
esg^ts>Ras^V12
esg^ts>Ras^V12, Piezo-i^B486
ProsGFPDAPI
f
P=0.569
P=0.389
Number of Pros+ cells / 10^4μm^2
esg^ts
esg^ts>Ras^V12
esg^ts>Ras^V12, Piezo-i^B486
g
P=0.44
P=0.44
Number of Pros+, GFP+ cells / 10^4μm^2
esg^ts
esg^ts>Ras^V12
esg^ts>Ras^V12, Piezo-i^B486

Supplementary Figure 8. Differentiation of EE cells are not affected by *Piezo* knockdown in *Ras^{V12}* cells.

a, Representative image of the posterior midguts at day 1 of transgene expression. *esg^{ts}, esg^{ts}>Ras^{V12}*, and *esg^{ts}>Ras^{V12}, Piezo-i^{8486}* midguts were stained with anti-Dl antibody (red) and DAPI (blue) Scale bars, 50 μm (top), 10 μm (middle and bottom). **b**, Quantification of Dl^{+} and GFP^{+} cells at day 1 of transgene expression. N=11 biological replicates. **c,** Quantification of pHH3 cells per gut after 3 days of expressing two RNAi lines (VDRC#v2796 and NIG#8486R-3) to knockdown *Piezo*. Day 1: N=9 (*esg^{ts}>Ras^{V12}*), N=22 (*esg^{ts}>Ras^{V12}, Piezo-i^{8486}*), N=23 (*esg^{ts}>Ras^{V12}, Piezo-i^{v2796}*); Day 2: N=8 (*esg^{ts}>Ras^{V12}*), N=13 (*esg^{ts}>Ras^{V12}, Piezo-i^{8486}*), N=23 (*esg^{ts}>Ras^{V12}, Piezo-i^{v2796}*); Day 3: N=21 (*esg^{ts}>Ras^{V12}*), N=35 (*esg^{ts}>Ras^{V12}, Piezo-i^{8486}*), N=41 (*esg^{ts}>Ras^{V12}, Piezo-i^{v2796}*) biological replicates. **d**, Quantification of pHH3 positive cells. Gd^{3+} treatment does not decrease cell proliferation. Day 1: N=14 (solvent), N=13 ($GdCl_3$); Day 2: N=19 (solvent), N=20 ($GdCl_3$) biological replicates. **e,** Representative image of the posterior midguts. EE cells were visualized by staining with anti-Prospero antibody (red). Scale bars, 50 μm (top), 10 μm (bottom). **f,** Quantification of Pros^{+} cells at day 1 of transgene expression. N=11 biological replicates. **g,** Quantification of Pros^{+} and GFP^{+} cells at day 1 of transgene expression. N=11 biological replicates. In **b**, **c**, **d, f**, and **g**, mean±SEMs are shown with individual data points. Data were analyzed by two-tailed unpaired Student's *t*-test. Asterisks indicate statistical significance (*P<0.01), and P-values are indicated in graph.

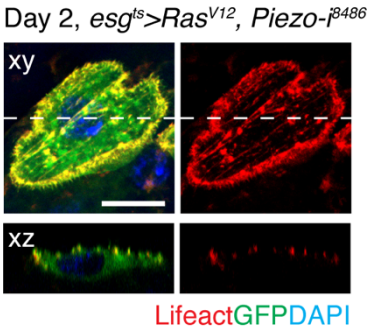
Day 2, esg^ts>Ras^V12, Piezo-i^8486
xy
xz
LifeactGFPDAPI

Supplementary Figure 9. *Piezo* is dispensable for Actin-rich puncta formation.

Lifeact puncta (red) were detected at the basal side of the Ras^{V12}, *Piezo* RNAi cells at day 2 of transgene expression. Representative images are shown from N=13 biological replicates. Scale bar, 10 μm.

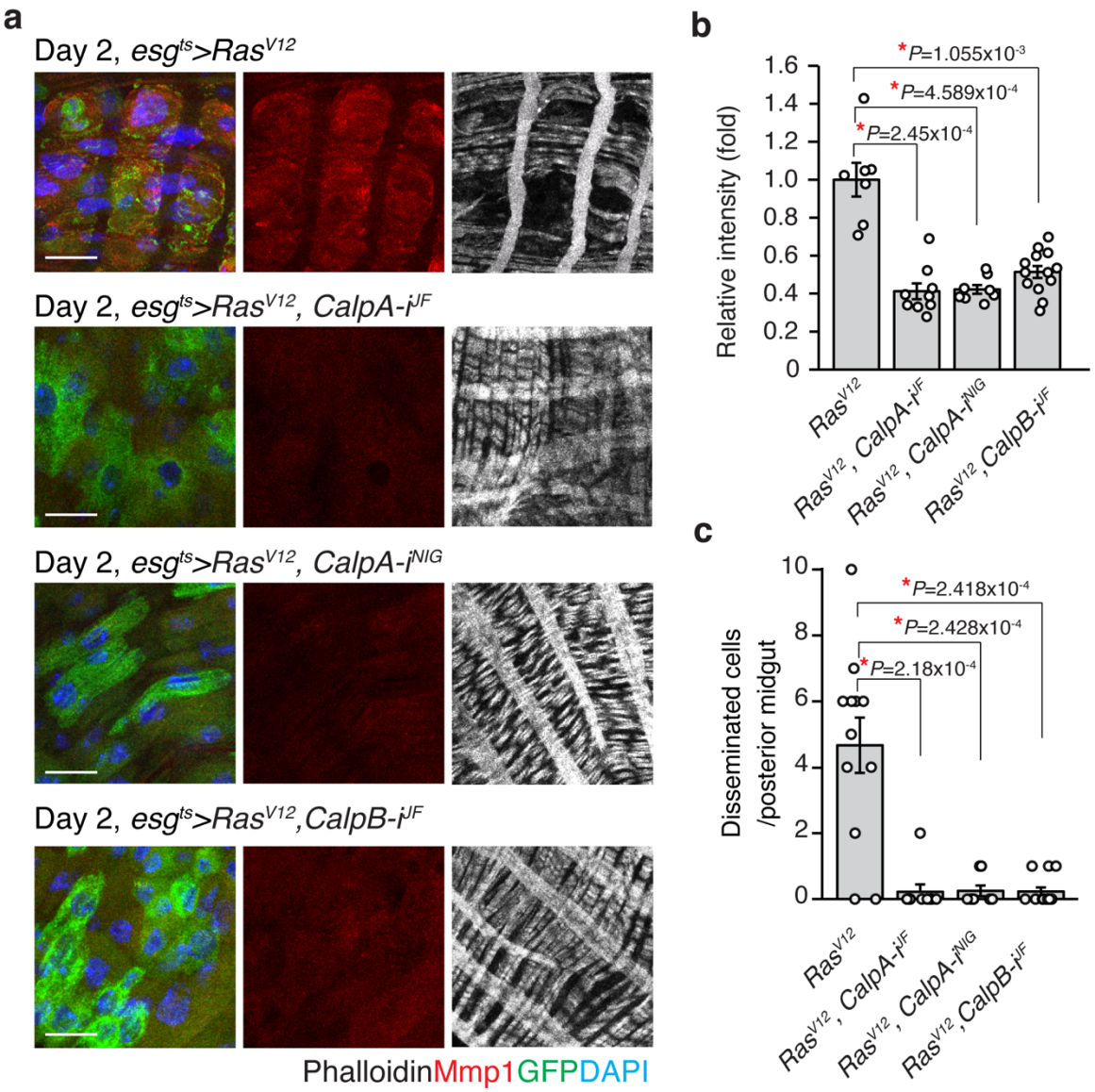
a
Day 2, esg^ts>Ras^V12
Day 2, esg^ts>Ras^V12, CalpA-i^JF
Day 2, esg^ts>Ras^V12, CalpA-i^NIG
Day 2, esg^ts>Ras^V12,CalpB-i^JF
PhalloidinMmp1GFPDAPI
b
Relative intensity (fold)
*P=1.055x10-3
*P=4.589x10-4
*P=2.45x10-4
Ras^V12
Ras^V12, CalpA-i^JF
Ras^V12, CalpA-i^NIG
Ras^V12,CalpB-i^JF
c
Disseminated cells /posterior midgut
*P=2.418x10-4
*P=2.428x10-4
*P=2.18x10-4
Ras^V12
Ras^V12, CalpA-i^JF
Ras^V12, CalpA-i^NIG
Ras^V12,CalpB-i^JF

Supplementary Figure 10. *Calpain* knockdown in *Ras^{V12}* cells suppress Mmp1 expression and inhibits cell dissemination.

a, Representative images of Mmp1(red) expression levels and visceral muscle integrity after 2 days of transgene induction. Visceral muscle is stained with Phalloidin (gray). ISC/EB are marked with GFP (green), and nuclei are stained with DAPI (blue). Scale bar, 20 μm. N=7 (*esg^{ts}>Ras^{V12}*), N=9 (*esg^{ts}>Ras^{V12}, CalpA-i^{JF}*), N=8(*esg^{ts}>Ras^{V12}, CalpA-i^{NIG}*), N=13 (*esg^{ts}>Ras^{V12}, CalpB-i^{JF}*) biological replicates. **b,** Quantification of Mmp1 levels per midgut. 3 regions were measured for each biological independent sample. **c,** Quantification of disseminated cells per midgut after 2 days of expression: N=12 (*esg^{ts}>Ras^{V12}*), N=9 (*esg^{ts}>Ras^{V12}, CalpA-i^{JF}*), N=8 (*esg^{ts}>Ras^{V12}, CalpA-i^{NIG}*), N=13 (*esg^{ts}>Ras^{V12}, CalpB-i^{JF}*) biological replicates. In **b** and **c**, mean±SEMs are shown with individual data points. Data were analyzed by two-tailed unpaired Student's *t*-test. Asterisks indicate statistical significance (*P<0.01), and P-values are indicated in graph.

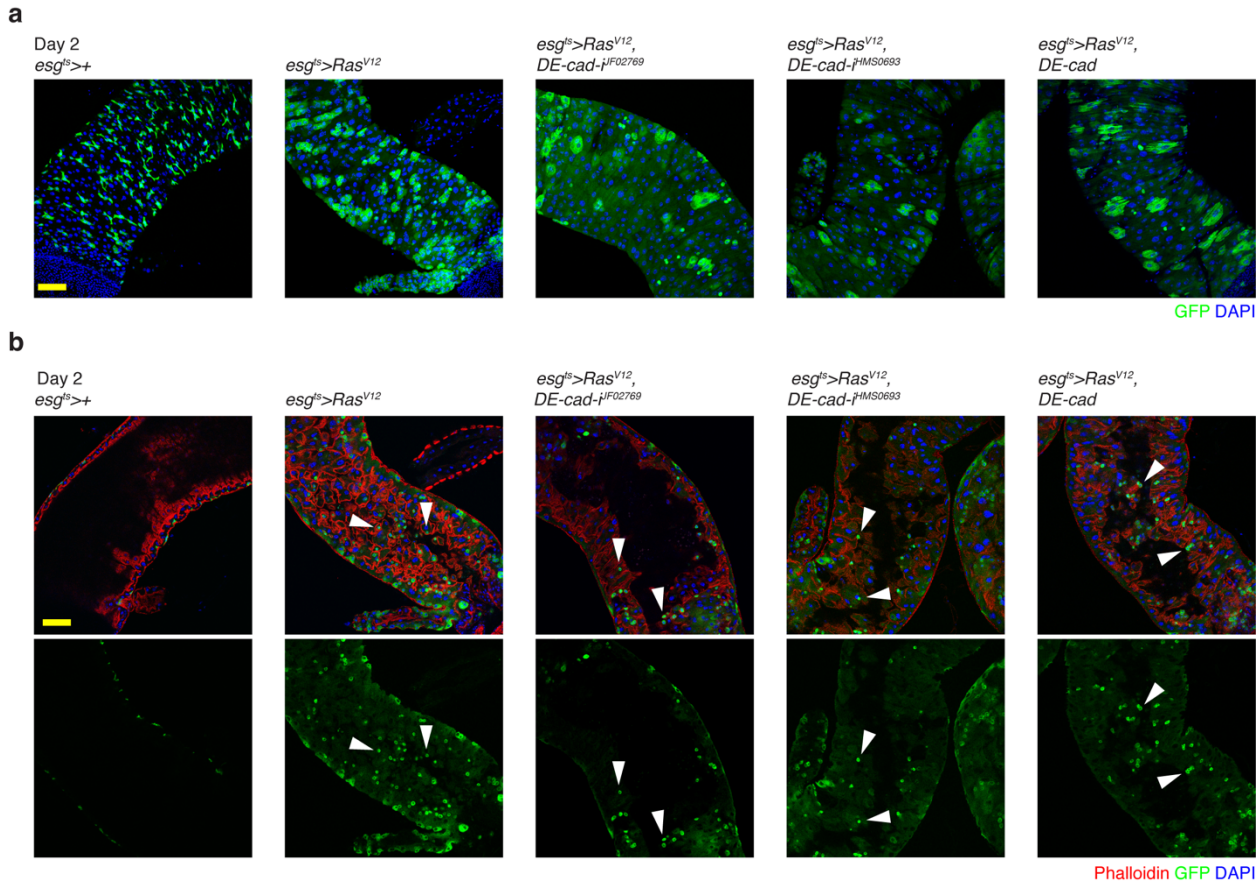
a
Day 2
esg^ts>+
esg^ts>Ras^V12
esg^ts>Ras^V12, DE-cad-i^JF02769
esg^ts>Ras^V12, DE-cad-i^HMS0693
esg^ts>Ras^V12, DE-cad
GFP DAPI
b
Day 2
esg^ts>+
esg^ts>Ras^V12
esg^ts>Ras^V12, DE-cad-i^JF02769
esg^ts>Ras^V12, DE-cad-i^HMS0693
esg^ts>Ras^V12, DE-cad
Phalloidin GFP DAPI

Supplementary Figure 11. DE-cadherin is dispensable for delamination of *Ras^{V12}* cells.

a, Posterior midguts at day 2 of transgene expression by *esg^{ts}*. Two DE-cad RNAi lines used to knockdown DE-cad are indicated as *DE-cad-i^{JF02769}* or *DE-cad-i^{HMS0693}*. Cells manipulated by *esg^{ts}* are labeled with GFP (green), and nuclei are stained with DAPI (blue). Scale bar, 50 μm. **b,** Representative images of the posterior midgut at day 2 of transgene expression. Cells manipulated with *esg^{ts}* express GFP (green). VM is stained with phalloidin (red) and nuclei with DAPI (blue). Images are single confocal stacks showing the longitudinal section of the midgut. Representative delaminating GFP^{+} cells are indicated with arrowheads. Scale bar, 50 μm.

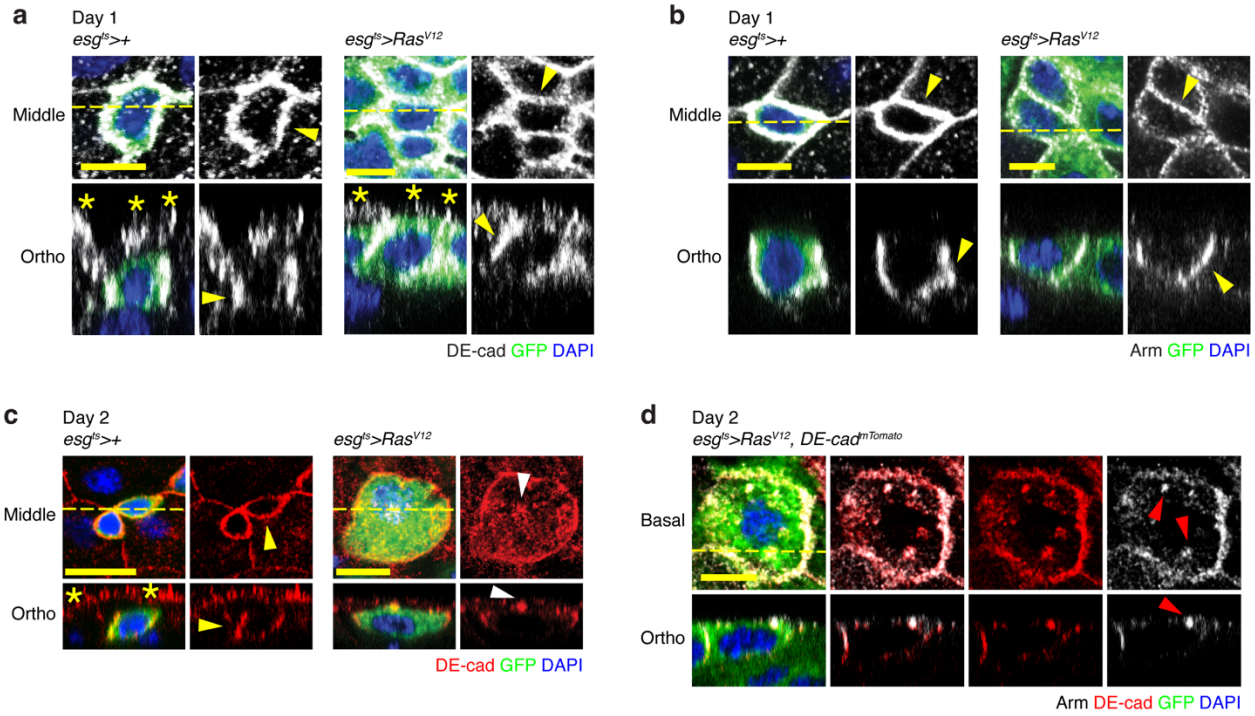
a
Day 1
esg^ts>+
esg^ts>Ras^V12
Middle
Ortho
DE-cad GFP DAPI
b
Day 1
esg^ts>+
esg^ts>Ras^V12
Middle
Ortho
Arm GFP DAPI
c
Day 2
esg^ts>+
esg^ts>Ras^V12
Middle
Ortho
DE-cad GFP DAPI
d
Day 2
esg^ts>Ras^V12, DE-cad^mTomato
Basal
Ortho
Arm DE-cad GFP DAPI

Supplementary Figure 12. DE-cadherin/Armadillo localizes at invasive protrusions.

a, Basal and orthogonal views showing DE-cad signals (gray). Day 1 *esg^{ts}>+* (control) and *esg^{ts}>Ras^{V12}* midguts were stained with anti-DE-cad antibody. Arrowheads indicate DE-cad signals at cell-cell junctions. Asterisks indicate nonspecific signals in the visceral muscle layer. Scale bar, 5 μm. **b,** Basal and orthogonal views showing Arm signals (gray). Day 1 *esg^{ts}>+* (control) and *esg^{ts}>Ras^{V12}* midguts were stained with anti-Arm antibody. Arrowheads indicate Arm signals at cell-cell junctions. Scale bar, 5 μm. **c**, Basal and orthogonal views showing DE-cad signals (red) at day 2 of transgene expression. yellow arrowheads indicate Arm signals at cell-cell junctions. White arrowheads show DE-cad signal puncta at the basal side of *Ras^{V12}* cell. Scale bar, 10 μm. **d**, DE-cad (red) and Arm (gray) co-localization at invasive protrusions. DE-cad signals (red) was detected by using a DE-cad protein-trap line (*DE-cad^{mTomato}*), which produces DE-cad-mTomato under control of the native *DE-cad* regulatory sequence. Arm signals (gray) were detected by staining with anti-Arm antibody. Arrowheads indicate basal puncta showing both DE-cad-mTomato and Arm signals. Scale bar, 10 μm. In all the orthogonal sections, the basal side of the epithelia is position upward.

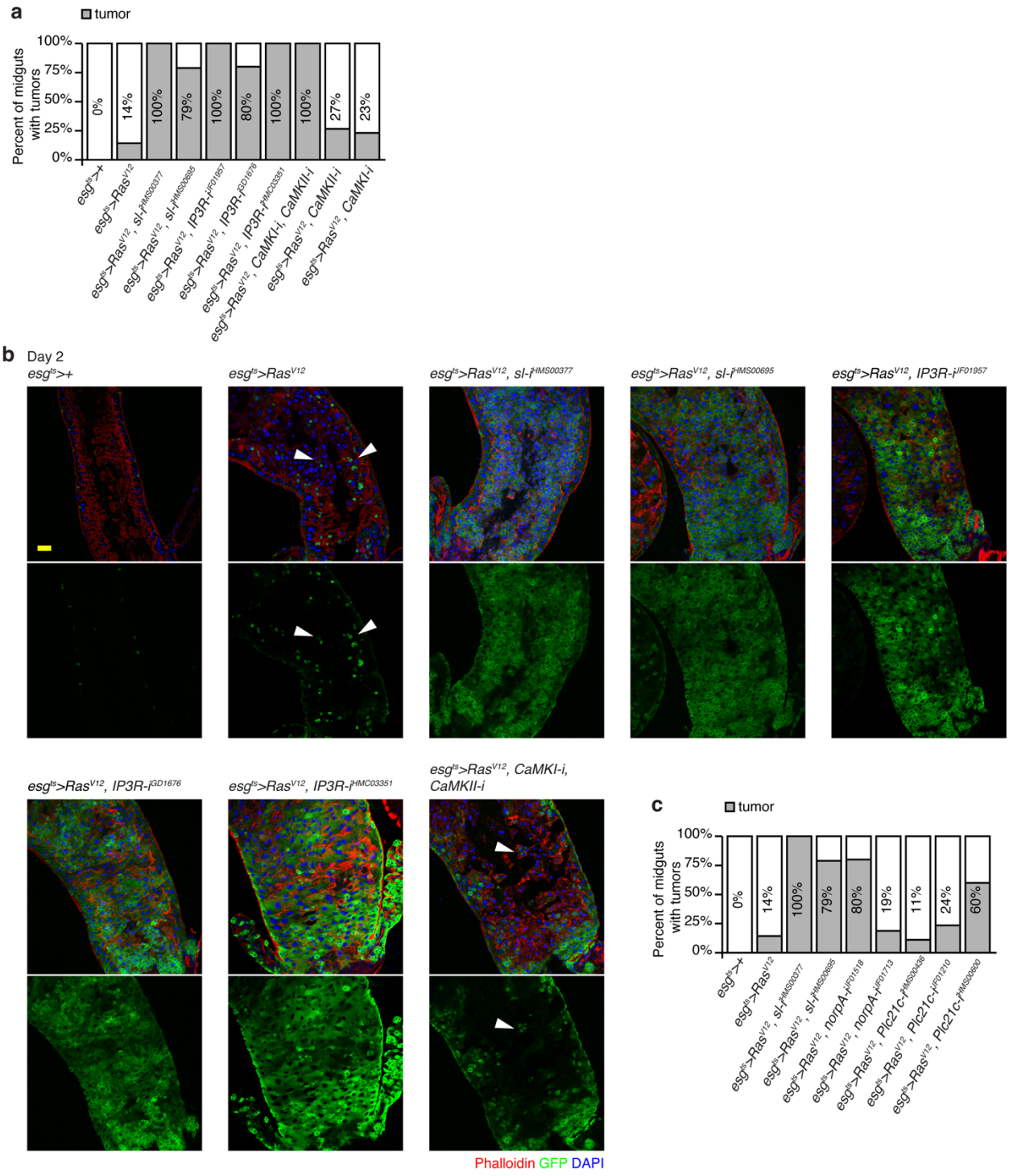
a
tumor
Percent of midguts with tumors
100%
75%
50%
25%
0%
0%
14%
100%
79%
100%
80%
100%
100%
27%
23%
esg^ts>+
esg^ts>Ras^V12
esg^ts>Ras^V12, sl-i^HMS00377
esg^ts>Ras^V12, sl-i^HMS00695
esg^ts>Ras^V12, IP3R-i^JF01957
esg^ts>Ras^V12, IP3R-i^GD1676
esg^ts>Ras^V12, IP3R-i^HMC03351
esg^ts>Ras^V12, CaMKI-i, CaMKII-i
esg^ts>Ras^V12, CaMKII-i
esg^ts>Ras^V12, CaMKI-i
b
Day 2
esg^ts>+
esg^ts>Ras^V12
esg^ts>Ras^V12, sl-i^HMS00377
esg^ts>Ras^V12, sl-i^HMS00695
esg^ts>Ras^V12, IP3R-i^JF01957
esg^ts>Ras^V12, IP3R-i^GD1676
esg^ts>Ras^V12, IP3R-i^HMC03351
esg^ts>Ras^V12, CaMKI-i, CaMKII-i
Phalloidin GFP DAPI
c
tumor
Percent of midguts with tumors
100%
75%
50%
25%
0%
0%
14%
100%
79%
80%
19%
11%
24%
60%
esg^ts>+
esg^ts>Ras^V12
esg^ts>Ras^V12, sl-i^HMS00377
esg^ts>Ras^V12, sl-i^HMS00695
esg^ts>Ras^V12, norpA-i^JF01516
esg^ts>Ras^V12, norpA-i^JF01713
esg^ts>Ras^V12, Plc21c-i^HMS00436
esg^ts>Ras^V12, Plc21c-i^JF01210
esg^ts>Ras^V12, Plc21c-i^HMS00600

Supplementary Figure 13. Depletion of the PLC-IP3R-CAMK pathway components induces midgut tumors.

a, Percentage stacked bar chart of midguts with epithelial tumors. *n*=10 (*esg^{ts}*), *n*=14 (*esg^{ts}>Ras^{V12}*), *n*=14 (*esg^{ts}>Ras^{V12}, sl-i^{HMS00377}*), *n*=19 (*esg^{ts}>Ras^{V12}, sl-i^{HMS00695}*), *n*=8 (*esg^{ts}>Ras^{V12}, IP3R-i^{JF01957}*), *n*=15 (*esg^{ts}>Ras^{V12}, IP3R-i^{GD1676}*), *n*=9 (*esg^{ts}>Ras^{V12}, IP3R-i^{HMC03351}*), *n*=10 (*esg^{ts}>Ras^{V12}, CaMKI-i, CaMKII-i*) biological replicates. **b**, Representative midgut longitudinal sections. Transgenes were induced for 2 days with *esg^{ts}*. Cells manipulated with *esg^{ts}* express GFP (green). Visceral muscles are visualized with Phalloidin (red), and nuclei are stained with DAPI (blue). Arrowheads indicate representative delaminating *GFP^{+}* cells. Scale bar, 50 μm. **c**, Percentage stacked bar chart of midguts with epithelial tumors. *n*=10 (*esg^{ts}*), *n*=14 (*esg^{ts}>Ras^{V12}*), *n*=14 (*esg^{ts}>Ras^{V12}, sl-i^{HMS00377}*), *n*=19 (*esg^{ts}>Ras^{V12}, sl-i^{HMS00695}*), *n*=15 (*esg^{ts}>Ras^{V12}, norpA-i^{JF01518}*), *n*=16 (*esg^{ts}>Ras^{V12}, norpA-i^{JF01713}*), *n*=9 (*esg^{ts}>Ras^{V12}, Plc21c-i^{HMS00436}*), *n*=17 (*esg^{ts}>Ras^{V12}, Plc21c-i^{JF01210}*), *n*=10 (*esg^{ts}>Ras^{V12}, Plc21c-i^{HMS00600}*) biological replicates. *small wing [sl]*, *no receptor potential A [norpA]*, and *Phospholipase C at 21C [Plc21c].*

References

1. Gomez-Cuadrado, L., Tracey, N., Ma, R., Qian, B. & Brunton, V.G. Mouse models of metastasis: progress and prospects. *Dis Model Mech* **10**, 1061-1074 (2017).
2. Saxena, M. & Christofori, G. Rebuilding cancer metastasis in the mouse. *Mol Oncol* **7**, 283-296 (2013).
3. Kang, Y. & Pantel, K. Tumor cell dissemination: emerging biological insights from animal models and cancer patients. *Cancer Cell* **23**, 573-581 (2013).
4. Cai, D. & Montell, D.J. Diverse and dynamic sources and sinks in gradient formation and directed migration. *Curr Opin Cell Biol* **30**, 91-98 (2014).
5. Bai, J., Uehara, Y. & Montell, D.J. Regulation of invasive cell behavior by taiman, a Drosophila protein related to AIB1, a steroid receptor coactivator amplified in breast cancer. *Cell* **103**, 1047-1058 (2000).
6. Sherwood, D.R. & Plastino, J. Invading, Leading and Navigating Cells in Caenorhabditis elegans: Insights into Cell Movement in Vivo. *Genetics* **208**, 53-78 (2018).
7. Sherwood, D.R. & Sternberg, P.W. Anchor cell invasion into the vulval epithelium in C. elegans. *Dev Cell* **5**, 21-31 (2003).
8. Sonoshita, M. & Cagan, R.L. Modeling Human Cancers in Drosophila. *Curr Top Dev Biol* **121**, 287-309 (2017).
9. Yu, F.X., Zhao, B. & Guan, K.L. Hippo Pathway in Organ Size Control, Tissue Homeostasis, and Cancer. *Cell* **163**, 811-828 (2015).

10. Hariharan, I.K. Organ Size Control: Lessons from Drosophila. *Dev Cell* **34**, 255-265 (2015).

11. Johnson, R. & Halder, G. The two faces of Hippo: targeting the Hippo pathway for regenerative medicine and cancer treatment. *Nat Rev Drug Discov* **13**, 63-79 (2014).

12. Pagliarini, R.A. & Xu, T. A genetic screen in Drosophila for metastatic behavior. *Science* **302**, 1227-1231 (2003).

13. Campbell, K. *et al.* Collective cell migration and metastases induced by an epithelial-to-mesenchymal transition in Drosophila intestinal tumors. *Nat Commun* **10**, 2311 (2019).

14. Bangi, E., Pitsouli, C., Rahme, L.G., Cagan, R. & Apidianakis, Y. Immune response to bacteria induces dissemination of Ras-activated Drosophila hindgut cells. *EMBO Rep* **13**, 569-576 (2012).

15. Bangi, E., Murgia, C., Teague, A.G., Sansom, O.J. & Cagan, R.L. Functional exploration of colorectal cancer genomes using Drosophila. *Nat Commun* **7**, 13615 (2016).

16. Hirabayashi, S., Baranski, T.J. & Cagan, R.L. Transformed Drosophila cells evade diet-mediated insulin resistance through wingless signaling. *Cell* **154**, 664-675 (2013).

17. Miles, W.O., Dyson, N.J. & Walker, J.A. Modeling tumor invasion and metastasis in Drosophila. *Dis Model Mech* **4**, 753-761 (2011).

18. Simanshu, D.K., Nissley, D.V. & McCormick, F. RAS Proteins and Their Regulators in Human Disease. *Cell* **170**, 17-33 (2017).

19. Wright, K.L. *et al.* Ras Signaling Is a Key Determinant for Metastatic Dissemination and Poor Survival of Luminal Breast Cancer Patients. *Cancer Res* **75**, 4960-4972 (2015).

20. Egan, S.E. *et al.* Expression of H-ras correlates with metastatic potential: evidence for direct regulation of the metastatic phenotype in 10T1/2 and NIH 3T3 cells. *Mol Cell Biol* **7**, 830-837 (1987).

21. McCaffrey, L.M., Montalbano, J., Mihai, C. & Macara, I.G. Loss of the Par3 polarity protein promotes breast tumorigenesis and metastasis. *Cancer Cell* **22**, 601-614 (2012).

22. Martorell, O. *et al.* Conserved mechanisms of tumorigenesis in the Drosophila adult midgut. *PLoS One* **9**, e88413 (2014).

23. Wang, C. *et al.* APC loss-induced intestinal tumorigenesis in Drosophila: Roles of Ras in Wnt signaling activation and tumor progression. *Dev Biol* **378**, 122-140 (2013).

24. Uhlirova, M. & Bohmann, D. JNK- and Fos-regulated Mmp1 expression cooperates with Ras to induce invasive tumors in Drosophila. *Embo J* **25**, 5294-5304 (2006).

25. Kelley, L.C. *et al.* Adaptive F-Actin Polymerization and Localized ATP Production Drive Basement Membrane Invasion in the Absence of MMPs. *Dev Cell* **48**, 313-328 e318 (2019).

26. Biteau, B., Hochmuth, C.E. & Jasper, H. JNK activity in somatic stem cells causes loss of tissue homeostasis in the aging Drosophila gut. *Cell Stem Cell* **3**, 442-455 (2008).

27. Lohmer, L.L., Kelley, L.C., Hagedorn, E.J. & Sherwood, D.R. Invadopodia and basement membrane invasion in vivo. *Cell Adh Migr* **8**, 246-255 (2014).

28. Eddy, R.J., Weidmann, M.D., Sharma, V.P. & Condeelis, J.S. Tumor Cell Invadopodia: Invasive Protrusions that Orchestrate Metastasis. *Trends Cell Biol* **27**, 595-607 (2017).

29. Parekh, A. & Weaver, A.M. Regulation of invadopodia by mechanical signaling. *Exp Cell Res* **343**, 89-95 (2016).

30. Clark, E.S. & Weaver, A.M. A new role for cortactin in invadopodia: regulation of protease secretion. *Eur J Cell Biol* **87**, 581-590 (2008).

31. Clark, E.S., Whigham, A.S., Yarbrough, W.G. & Weaver, A.M. Cortactin is an essential regulator of matrix metalloproteinase secretion and extracellular matrix degradation in invadopodia. *Cancer Res* **67**, 4227-4235 (2007).

32. Spracklen, A.J., Fagan, T.N., Lovander, K.E. & Tootle, T.L. The pros and cons of common actin labeling tools for visualizing actin dynamics during Drosophila oogenesis. *Dev Biol* **393**, 209-226 (2014).

33. Meehan, B., Rak, J. & Di Vizio, D. Oncosomes - large and small: what are they, where they came from? *J Extracell Vesicles* **5**, 33109 (2016).

34. Headley, M.B. *et al.* Visualization of immediate immune responses to pioneer metastatic cells in the lung. *Nature* **531**, 513-517 (2016).

35. Becker, A. *et al.* Extracellular Vesicles in Cancer: Cell-to-Cell Mediators of Metastasis. *Cancer Cell* **30**, 836-848 (2016).

36. Wolf, K. *et al.* Compensation mechanism in tumor cell migration: mesenchymal-amoeboid transition after blocking of pericellular proteolysis. *J Cell Biol* **160**, 267-277 (2003).

37. Pandya, P., Orgaz, J.L. & Sanz-Moreno, V. Modes of invasion during tumour dissemination. *Mol Oncol* **11**, 5-27 (2017).

38. Paluch, E.K., Aspalter, I.M. & Sixt, M. Focal Adhesion-Independent Cell Migration. *Annu Rev Cell Dev Biol* **32**, 469-490 (2016).

39. Kim, S.E., Coste, B., Chadha, A., Cook, B. & Patapoutian, A. The role of Drosophila Piezo in mechanical nociception. *Nature* **483**, 209-212 (2012).

40. He, L., Si, G., Huang, J., Samuel, A.D.T. & Perrimon, N. Mechanical regulation of stem-cell differentiation by the stretch-activated Piezo channel. *Nature* (2018).

41. Coste, B. *et al.* Piezo1 and Piezo2 are essential components of distinct mechanically activated cation channels. *Science* **330**, 55-60 (2010).

42. He, L., Si, G., Huang, J., Samuel, A.D.T. & Perrimon, N. Mechanical regulation of stem-cell differentiation by the stretch-activated Piezo channel. *Nature* **555**, 103-106 (2018).

43. Pardo-Pastor, C. *et al.* Piezo2 channel regulates RhoA and actin cytoskeleton to promote cell mechanobiological responses. *Proc Natl Acad Sci U S A* **115**, 1925-1930 (2018).

44. McHugh, B.J. *et al.* Integrin activation by Fam38A uses a novel mechanism of R-Ras targeting to the endoplasmic reticulum. *J Cell Sci* **123**, 51-61 (2010).

45. MacGrath, S.M. & Koleske, A.J. Cortactin in cell migration and cancer at a glance. *J Cell Sci* **125**, 1621-1626 (2012).

46. Te Boekhorst, V., Preziosi, L. & Friedl, P. Plasticity of Cell Migration In Vivo and In Silico. *Annu Rev Cell Dev Biol* **32**, 491-526 (2016).

47. Liu, Y.J. *et al.* Confinement and low adhesion induce fast amoeboid migration of slow mesenchymal cells. *Cell* **160**, 659-672 (2015).

48. Srivastava, N., Traynor, D., Piel, M., Kabla, A.J. & Kay, R.R. Pressure sensing through Piezo channels controls whether cells migrate with blebs or pseudopods. *Proc Natl Acad Sci U S A* **117**, 2506-2512 (2020).

49. Harris, T.J. & Tepass, U. Adherens junctions: from molecules to morphogenesis. *Nat Rev Mol Cell Biol* **11**, 502-514 (2010).

50. Gumbiner, B.M. Regulation of cadherin-mediated adhesion in morphogenesis. *Nat Rev Mol Cell Biol* **6**, 622-634 (2005).

51. Mendonsa, A.M., Na, T.Y. & Gumbiner, B.M. E-cadherin in contact inhibition and cancer. *Oncogene* **37**, 4769-4780 (2018).

52. Larue, L., Ohsugi, M., Hirchenhain, J. & Kemler, R. E-cadherin null mutant embryos fail to form a trophectoderm epithelium. *Proc Natl Acad Sci U S A* **91**, 8263-8267 (1994).

53. Burdsal, C.A., Damsky, C.H. & Pedersen, R.A. The role of E-cadherin and integrins in mesoderm differentiation and migration at the mammalian primitive streak. *Development* **118**, 829-844 (1993).

54. Onder, T.T. *et al.* Loss of E-cadherin promotes metastasis via multiple downstream transcriptional pathways. *Cancer Res* **68**, 3645-3654 (2008).

55. Vleminckx, K., Vakaet, L., Jr., Mareel, M., Fiers, W. & van Roy, F. Genetic manipulation of E-cadherin expression by epithelial tumor cells reveals an invasion suppressor role. *Cell* **66**, 107-119 (1991).

56. Strobl-Mazzulla, P.H. & Bronner, M.E. Epithelial to mesenchymal transition: new and old insights from the classical neural crest model. *Semin Cancer Biol* **22**, 411-416 (2012).

57. Cano, A. *et al.* The transcription factor snail controls epithelial-mesenchymal transitions by repressing E-cadherin expression. *Nat Cell Biol* **2**, 76-83 (2000).

58. Thiery, J.P., Acloque, H., Huang, R.Y. & Nieto, M.A. Epithelial-mesenchymal transitions in development and disease. *Cell* **139**, 871-890 (2009).

59. Hajra, K.M., Chen, D.Y. & Fearon, E.R. The SLUG zinc-finger protein represses E-cadherin in breast cancer. *Cancer Res* **62**, 1613-1618 (2002).

60. Frixen, U.H. *et al.* E-cadherin-mediated cell-cell adhesion prevents invasiveness of human carcinoma cells. *J Cell Biol* **113**, 173-185 (1991).

61. Bogenrieder, T. & Herlyn, M. Axis of evil: molecular mechanisms of cancer metastasis. *Oncogene* **22**, 6524-6536 (2003).

62. Berx, G. *et al.* E-cadherin is a tumour/invasion suppressor gene mutated in human lobular breast cancers. *Embo J* **14**, 6107-6115 (1995).

63. Padmanaban, V. *et al.* E-cadherin is required for metastasis in multiple models of breast cancer. *Nature* **573**, 439-444 (2019).

64. Na, T.Y., Schecterson, L., Mendonsa, A.M. & Gumbiner, B.M. The functional activity of E-cadherin controls tumor cell metastasis at multiple steps. *Proc Natl Acad Sci U S A* **117**, 5931-5937 (2020).

65. Perl, A.K., Wilgenbus, P., Dahl, U., Semb, H. & Christofori, G. A causal role for E-cadherin in the transition from adenoma to carcinoma. *Nature* **392**, 190-193 (1998).

66. Berx, G. & Van Roy, F. The E-cadherin/catenin complex: an important gatekeeper in breast cancer tumorigenesis and malignant progression. *Breast Cancer Res* **3**, 289-293 (2001).

67. Semb, H. & Christofori, G. The tumor-suppressor function of E-cadherin. *Am J Hum Genet* **63**, 1588-1593 (1998).

68. Herzig, M., Savarese, F., Novatchkova, M., Semb, H. & Christofori, G. Tumor progression induced by the loss of E-cadherin independent of beta-catenin/Tcf-mediated Wnt signaling. *Oncogene* **26**, 2290-2298 (2007).

69. Petrova, Y.I., Schecterson, L. & Gumbiner, B.M. Roles for E-cadherin cell surface regulation in cancer. *Mol Biol Cell* **27**, 3233-3244 (2016).

70. Christofori, G. & Semb, H. The role of the cell-adhesion molecule E-cadherin as a tumour-suppressor gene. *Trends Biochem Sci* **24**, 73-76 (1999).

71. Kleer, C.G., van Golen, K.L., Braun, T. & Merajver, S.D. Persistent E-cadherin expression in inflammatory breast cancer. *Mod Pathol* **14**, 458-464 (2001).

72. Di Venosa, G. *et al.* Changes in actin and E-cadherin expression induced by 5-aminolevulinic acid photodynamic therapy in normal and Ras-transfected human mammary cell lines. *J Photochem Photobiol B* **106**, 47-52 (2012).

73. Sundfeldt, K. *et al.* E-cadherin expression in human epithelial ovarian cancer and normal ovary. *Int J Cancer* **74**, 275-280 (1997).

74. Kim, S.A. *et al.* Loss of CDH1 (E-cadherin) expression is associated with infiltrative tumour growth and lymph node metastasis. *Br J Cancer* **114**, 199-206 (2016).

75. Lee, J., Cabrera, A.J.H., Nguyen, C.M.T. & Kwon, Y.V. Dissemination of Ras(V12)-transformed cells requires the mechanosensitive channel Piezo. *Nat Commun* **11**, 3568 (2020).

76. Kwon, Y. *et al.* Systemic organ wasting induced by localized expression of the secreted insulin/IGF antagonist ImpL2. *Dev Cell* **33**, 36-46 (2015).

77. Belin, B.J., Goins, L.M. & Mullins, R.D. Comparative analysis of tools for live cell imaging of actin network architecture. *Bioarchitecture* **4**, 189-202 (2014).

78. Riedl, J. *et al.* Lifeact: a versatile marker to visualize F-actin. *Nat Methods* **5**, 605-607 (2008).

79. Millard, T.H. & Martin, P. Dynamic analysis of filopodial interactions during the zippering phase of Drosophila dorsal closure. *Development* **135**, 621-626 (2008).

80. Liu, R. *et al.* Sisyphus, the Drosophila myosin XV homolog, traffics within filopodia transporting key sensory and adhesion cargos. *Development* **135**, 53-63 (2008).

81. Berridge, M.J. The Inositol Trisphosphate/Calcium Signaling Pathway in Health and Disease. *Physiol Rev* **96**, 1261-1296 (2016).

82. Kadamur, G. & Ross, E.M. Mammalian phospholipase C. *Annu Rev Physiol* **75**, 127-154 (2013).

83. Murthy, S.E., Dubin, A.E. & Patapoutian, A. Piezos thrive under pressure: mechanically activated ion channels in health and disease. *Nat Rev Mol Cell Biol* **18**, 771-783 (2017).

84. Bagriantsev, S.N., Gracheva, E.O. & Gallagher, P.G. Piezo proteins: regulators of mechanosensation and other cellular processes. *J Biol Chem* **289**, 31673-31681 (2014).

85. Chemaly, E.R., Troncone, L. & Lebeche, D. SERCA control of cell death and survival. *Cell Calcium* **69**, 46-61 (2018).

86. Michelangeli, F. & East, J.M. A diversity of SERCA Ca2+ pump inhibitors. *Biochem Soc Trans* **39**, 789-797 (2011).

87. Saitoh, S. *et al.* Rab5-regulated endocytosis plays a crucial role in apical extrusion of transformed cells. *Proc Natl Acad Sci U S A* **114**, E2327-E2336 (2017).

88. Lamouille, S., Xu, J. & Derynck, R. Molecular mechanisms of epithelial-mesenchymal transition. *Nat Rev Mol Cell Biol* **15**, 178-196 (2014).

89. Yu, W., Yang, L., Li, T. & Zhang, Y. Cadherin Signaling in Cancer: Its Functions and Role as a Therapeutic Target. *Front Oncol* **9**, 989 (2019).

90. Yu, Y. *et al.* Piezo1 regulates migration and invasion of breast cancer cells via modulating cell mechanobiological properties. *Acta Biochim Biophys Sin (Shanghai)* **53**, 10-18 (2021).

91. Dobric, A. *et al.* E-cadherin: Unexpected actor of invadopodia formation in pancreatic cancer. *bioRxiv*, 2020.2010.2009.332783 (2020).

92. Apidianakis, Y., Pitsouli, C., Perrimon, N. & Rahme, L. Synergy between bacterial infection and genetic predisposition in intestinal dysplasia. *Proc Natl Acad Sci U S A* **106**, 20883-20888 (2009).

93. Aldaz, S., Escudero, L.M. & Freeman, M. Live imaging of Drosophila imaginal disc development. *Proc Natl Acad Sci U S A* **107**, 14217-14222 (2010).

94. Haselton, A.T. & Fridell, Y.W. Insulin injection and hemolymph extraction to measure insulin sensitivity in adult Drosophila melanogaster. *J Vis Exp* (2011).

95. Singleton, K. & Woodruff, R.I. The osmolarity of adult Drosophila hemolymph and its effect on oocyte-nurse cell electrical polarity. *Dev Biol* **161**, 154-167 (1994).